NEGATIVE ION RESONANCES IN MAGNESIUM AND CADMIUM

A thesis submitted for the degree of
Doctor of Philosophy
of the Australian National University

by
James Patrick Sullivan

11th May 1999

This thesis contains no material which has been accepted for the award of any other degree or diploma in any university. To the best of the author's knowledge and belief, it contains no material previously published or written by another person, except where due reference is made in the text.

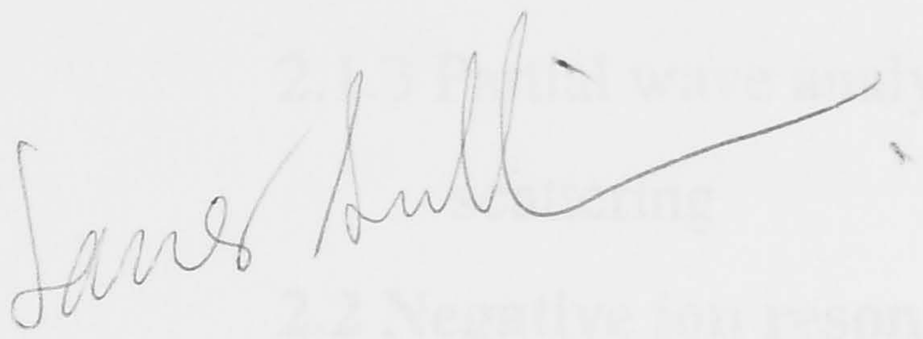

James Patrick Sullivan

11th May 1999

TABLE OF CONTENTS

Summary

This thesis reports high resolution electron scattering experiments on magnesium and cadmium. Elastic electron scattering measurements as a function of angle and energy, and electron impact excitation measurements as a function of energy have been performed on magnesium and cadmium, and negative ion resonances have been identified and classified for both elements. An attempt has also been made to measure a metastable atom excitation function for cadmium. The thesis consists of seven chapters, and the first presents a brief overview of the field of negative ion resonances.

Chapter 2 provides an introduction to the theoretical approaches to the electron-atom scattering problem in general, and to the formation and description of negative ion resonances in particular.

In chapter 3, a description of the apparatus is given, and the development of a new metal vapour oven for the apparatus, a photon detection system and a detector for metastable cadmium atoms is outlined.

Techniques used for the presentation and analysis of the data are outlined in chapter 4, and the results of the electron scattering experiments are presented in chapter 5. Electron scattering and photon excitation measurements have been performed from an incident energy of 2 eV to an energy of 7.7 eV in magnesium. This represents an energy region from just below the first excited state ($3p\ ^3P_0$ at 2.71 eV) to just above the ionisation threshold (7.644 eV). Elastic electron scattering measurements have been performed at scattering angles of 24°, 54°, 90° and 120° over this energy range, and the excitation of the $3p\ ^1P_1$ state has been measured. For cadmium, the energy range of the incident electrons extended from 3 eV to 13.5 eV, which is from just below the first excited state ($5p\ ^3P_0$ at 3.737 eV) to several electron volts above the ionisation potential (8.99 eV). Elastic electron scattering measurements have been made at scattering angles

of 24°, 54°, 90° and 120°. The excitation of the 5p $^1P_1$ and 5p $^3P_1$ states were also examined as a function of incident electron energy.

Chapter 6 presents the analysis of the results, and proposes classifications for the negative ion resonances observed, based on the measurements presented in this thesis as well as comparisons with previous experiments on mercury. The results are compared to available previous experimental and theoretical work on negative ion resonances in these systems. Chapter 7 gives some brief concluding remarks.

Acknowledgements

The first person that must be thanked for guiding me through the last three years or so is my supervisor, Dr. Steve Buckman. He has been a source of knowledge, inspiration and much needed motivation and I'd like to think that he's taught me a lot of physics along the way. Nothing presented here would have been possible without his support and advice.

Professor Paul Burrow and Dr. Stan Newman deserve special mention for introducing me to the weird and wonderful world of resonance analysis. They have also taught me much about this field, and often provided much needed help and encouragement. I would also like to thank Professor Bob McEachran and Dr. Jim Mitroy for having the patience to explain the more confusing aspects of the theory to me.

Technical support for my project has been without peer, and I would like to extend my thanks to Kevin Roberts and Graeme Cornish for their work and constant availability to help with the smallest of problems. Steve Battisson deserves special mention as he has helped with the majority of the design work and maintainence on the experiment over the last three years, and has also provided invaluable assistance with preparing the graphics for this thesis.

Thanks also goes to the rest of the AMPL gang, past and present, who have provided a friendly and stimulating working environment, and were always ready with suggestions or ideas when I've been stuck. The social gatherings outside have also been most enjoyable.

My parents, brothers and sisters have been a source of great support when I've needed them, and have encouraged my studies in physics. They have managed to give me a great start in life.

Finally, and most importantly, I would like to thank my wife Gillian, without whom all of this would have been impossible, and my daughter Chloe, without whom it would have been pointless.

Chapter 1

Introduction

The study of atoms and their interactions has a long history, and finds application in nearly all areas of modern day scientific endeavour, such as chemistry, pharmacology, biology, genetics, atmospheric science, electronics and most branches of physics, to name but a few. Many different techniques have been devised with which to probe the structure and properties of atomic systems, with electron scattering being only one of many. As technology improves and new ideas are developed, more innovative approaches are being taken in the development of electron scattering experiments, which are increasing the versatility and usefulness of the electron scattering approach. High resolution electron beams allow the measurement of scattering cross sections to a high degree of accuracy, and these, in turn, are of particular use in applied areas such as discharge plasma physics among others. Electron beams can also be used to investigate specific excited states of atomic systems. Indeed one of the inherent values of electron scattering experiments lies in the fact that dipole forbidden transitions of atomic systems can be investigated, unlike techniques which, for instance, rely on single photons as an atomic probe. High precision measurements of specific atomic states are now able to be made to the point where a "complete" description of these states is possible from a single experiment. New parallel detection techniques for electrons, developed to take advantage of multichannel detectors such as channel plates and resistive anodes, now mean that large amounts of data are able to be taken in a very short time, opening up new areas of atomic investigation.

Short lived negative ion states, or resonances, often occur in electron scattering processes when the projectile electron attaches to the target atom or molecule for a short

period of time. Whilst several alternate techniques have been developed to study these states, such as negative-ion photodetachment and ion-atom collisions, the overwhelming body of work has come from electron scattering. Resonances can appear as prominent structures in many of the cross sections which are measured in electron scattering. These include differential and total cross sections, metastable atom excitation cross sections and photon decay spectra. The first identification of a negative ion resonance was made by Schulz in 1963 performing electron scattering experiments on helium, although evidence of resonances appeared much earlier than this, with the earliest reported observation in the research of Walter Brattain (1929). In this work, however, there was no understanding of what caused the observed effect. Further experimental confirmation of Schulz's observation quickly followed, with experiments by Simpson and Fano (1963), and Fleming and Higginson (1963). The first theoretical calculation of this He^- state was by LeBahn and Callaway (1964), and since this time, helium has provided a popular atom for studies of negative ion resonances, both experimentally and theoretically. Schulz (1973) provides a good history of the development of the field, along with a summary of the investigations of negative ion resonances up to that time. For a more recent, comprehensive review, Buckman and Clark (1994) summarise the work undertaken on negative ion resonances in atomic systems since Schulz's review.

The description and prediction of negative ion resonances provides a demanding challenge for theorists, as the negative ion states typically result from a highly correlated electron motion and the orbitals are very diffuse, leading to complications in the application of standard theoretical approaches. Negative ion resonances are also systems where the independent particle model does not always provide a good description. In this model, the electrons are presumed to interact only weakly with each other, or not at all, and this leads to difficulties in systems where correlated electron motion is important. As a result of these problems, new theories have been developed which describe the negative ion complex, including correlation effects. In some cases these approaches have resulted in the development of new quantum numbers for the description of the motion of two or more correlated electrons. These developments

have been crucial in furthering our understanding of negative ion and atomic systems and their interactions. For experimentalists, the challenge is as great as for theorists, with new experimental techniques required to investigate these features as the need for higher energy resolution and greater signal to background ratios in the experiments become apparent.

Studies of negative ion resonances in many atomic systems have been undertaken, particularly in the heavier noble gases and the one-electron atoms. However, the properties of negative ion resonances for many groups of elements in the periodic table have yet to be examined. Of particular interest are the Group IIA and IIB elements, where the lack of information on negative ion resonance formation in these groups has provided the principle motivation for the commencement of the experimental program outlined in this thesis. The experiments also provide the chance to investigate the influence of the atomic structure on the observed spectra of negative ions. Magnesium, for instance, has an outer electron configuration of $2p^63s^2$ and zinc, cadmium and mercury have a $(n-1)d^{10}ns^2$ outer electron configuration (n=4, 5 and 6 respectively). It may be interesting to see what influence the full d-shell in the latter three, along with the increase in principle quantum number, has on the negative ion resonance formation in the different elements.

Little previous experimental data exists for negative ion resonances in magnesium, with only the electron transmission experiments of Burrow et al. (1976) and Burrow (1998), and the optical excitation experiments of Shpenik et al. (1979) available. Possible resonance structures have also been observed in optical excitation spectra measured by Shafran'osh et al. (1994), Leep and Gallagher (1976), Aleksakhin et al. (1973) and Karstensen and Köster (1971), although no comprehensive analysis of these results has been undertaken in terms of negative ion resonances. There are numerous theoretical calculations for resonances in magnesium, although they have mainly concentrated only on the lowest-lying negative ion state. Examples of this are the work by Yuan and Zhang (1989), Kurtz and Jordan (1981), Fabrikant (1974) and Van Blerkom (1970). Theoretical calculations of optical excitation and electron

scattering from magnesium have recently been made by Gedeon et al. (1999) who have identified several higher lying resonances within the energy range of the experiments presented here.

There has also, to date, been little experimental work on negative ion resonances in cadmium. Again, Burrow et al. (1976) and Burrow (1998) have observed several resonances in their electron transmission experiments, and resonances have been observed in the optical excitation functions of Shpenik et al. (1973), in the spin asymmetry measurements of Bartsch et al. (1992) and in elastic scattering by Panajatovic et al. (1994). Theoretical effort has again concentrated only on the lowest lying resonance, with calculations by Sin Fai Lam (1981) and Zollweg (1969). Only Bartschat (1998) has calculated cross sections for elastic scattering and optical excitation in cadmium for an energy range that is accesible for the present experiments.

In the present investigation, experiments have been performed to examine the negative ion resonance spectrum of magnesium and cadmium. The energy dependence of elastic electron scattering and several optical excitation cross sections have been measured, and resonances have been observed in these spectra. An attempt has also been made to measure excitation functions for metastable cadmium atoms. Resonances were observed in magnesium from just below the excitation of the 3p ^{3}P states at 2.711 eV up to the ionisation limit of 7.644 eV. In the case of cadmium, resonances have been observed from just below the excitation energy of the 5p ^{3}P states at 3.737 eV to above the ionisation limit of cadmium (8.99 eV) at an energy of 13.5 eV. Classifications for the observed resonances have been proposed, based on comparisons with previous experimental data and the angular behaviour of the resonances in the elastic scattering cross section.

Chapter 2

Theory

2.1 Electron - atom scattering

2.1.1 Introduction

A theoretical description of electron scattering from atomic systems can be found in a variety of texts. In particular, Mott and Massey (1965), Bransden and Joachain (1983) and McDaniel (1989) provide a detailed guide to the theory of electron-atom collisions, and have been used, in part, for the preparation of this section. This is intended to be a brief overview of electron-atom scattering theory in order to introduce some of the fundamental concepts required for the analysis of the results of the experiments presented in this thesis.

Electrons can scatter from atoms in a variety of different ways, with a number of different reactions and reaction products possible. Examples of some of the reactions which are relevant to the experiments presented in this thesis are:

Direct scattering:

$$\begin{aligned} e^- + A &\rightarrow e^- + A && (elastic) \\ &\rightarrow e^- + A^* \rightarrow e^- + A + h\upsilon && (inelastic) \end{aligned}$$

Scattering via a negative ion resonance:

$$\begin{aligned} e^- + A &\rightarrow A^{-*} \rightarrow e^- + A && (elastic) \\ &\rightarrow e^- + A^* \rightarrow e^- + A + h\upsilon && (inelastic) \end{aligned}$$

In these cases the asterisk indicates that the species is in an excited state, and it can be seen that there is more than one possible pathway to the same end products.

Negative ion resonances (A^{-*}) typically occur at well defined energies, corresponding to the energy levels of excited states of the negative ion. Scattering via a negative ion resonance has an influence on the cross section being measured, typically giving rise to sharp features when the yield of a given scattering process is examined as a function of energy. It is these effects which form the basis of the experiments presented in this thesis. Before examining in detail the theoretical treatment of these negative ion resonances, it is appropriate to consider some of the basic concepts of general scattering theory.

2.1.2 Scattering cross sections

The result of a collision of an electron with an atom can be expressed in terms of the scattering cross section for that specific collision. This is defined as the ratio of the number of collisions of a specific type per unit time, per unit scatterer, to the flux of incident electrons. It is essentially a measure of the probability of a certain type of collision occurring under a given set of conditions.

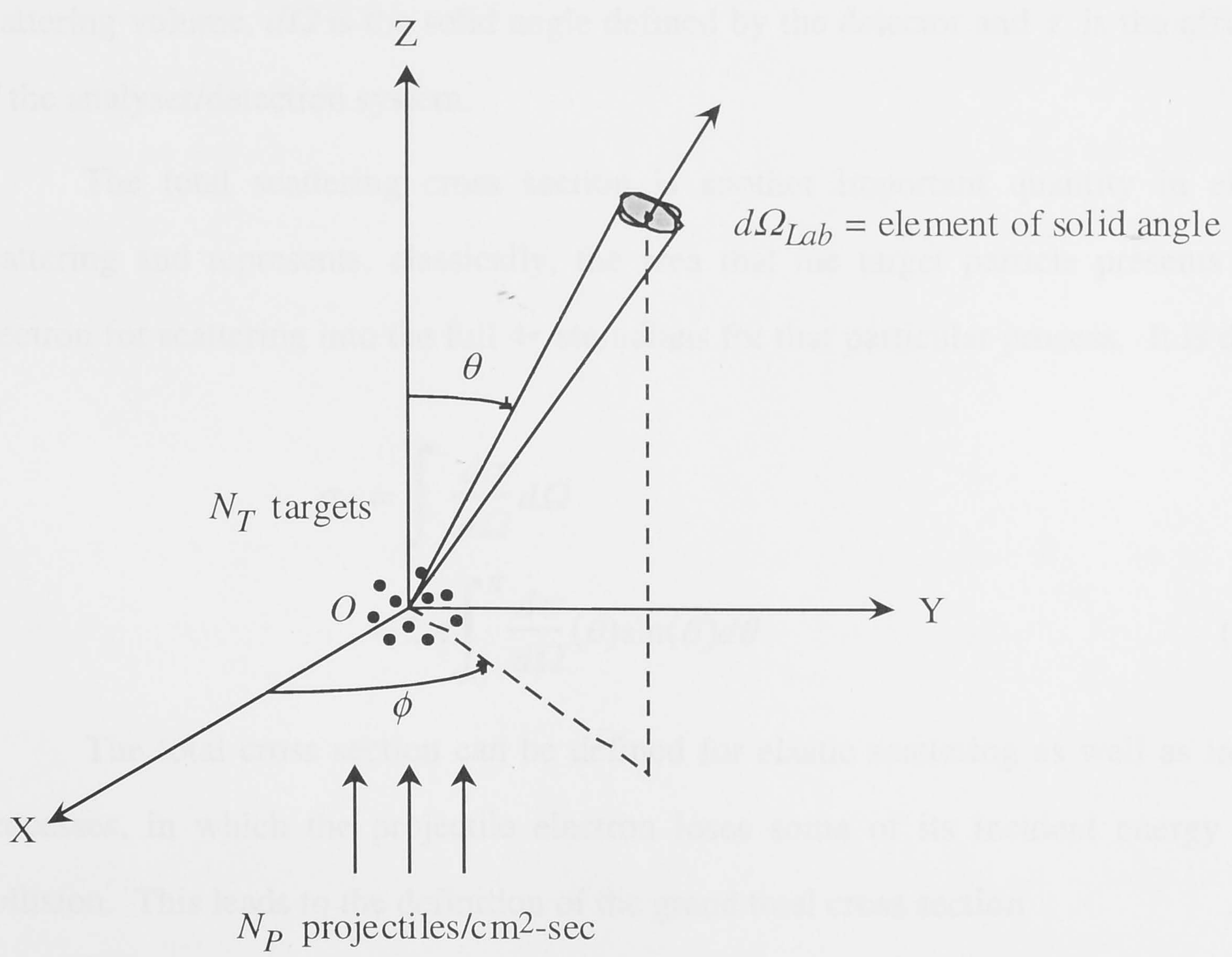

Figure 2.1: Beam of projectiles scattered from a target

To demonstrate this, we can consider a parallel beam of electrons incident on a number of target particles, as shown in figure 2.1 above (from McDaniel, 1989).

Of relevance to many of the measurements in this thesis is the differential cross section per unit solid angle, $\frac{d\sigma}{d\Omega}(\theta,\phi)$, which can be thought of in a classical sense as the area presented to the electrons by the target atom or molecule for scattering into the element $d\Omega$ of solid angle. In terms of figure 2.1, this quantity can be expressed as

$$\frac{d\sigma}{d\Omega}(\theta,\phi)=\frac{N_S(\theta,\phi)}{N_P N_T} \tag{2.1}$$

where N_s is the number of scattered electrons. This can be rewritten in terms of typical experimental parameters as

$$\frac{d\sigma}{d\Omega}(E,\theta)=\frac{I_s(E,\theta)}{I_o(E,\theta)}\frac{1}{Nld\Omega\tau} \tag{2.2}$$

where I_s and I_o are the scattered and incident electron currents respectively, N is the number density of the target particles in the scattering region, l is the length of the scattering volume, $d\Omega$ is the solid angle defined by the detector and τ is the efficiency of the analyser/detection system.

The total scattering cross section is another important quantity in electron scattering and represents, classically, the area that the target particle presents to the electron for scattering into the full 4• steradians for that particular process. It is defined as

$$\begin{aligned}\sigma_T &= \int \frac{d\sigma}{d\Omega}d\Omega \\ &= 2\pi\int_0^{\pi}\frac{d\sigma}{d\Omega}(\theta)\sin(\theta)d\theta\end{aligned} \tag{2.3}$$

The total cross section can be defined for elastic scattering as well as inelastic processes, in which the projectile electron loses some of its incident energy in the collision. This leads to the definition of the grand total cross section

$$Q_T = \sigma_{Tel} + \sigma_{T1} + \sigma_{T2} + \ldots\ldots\ldots \tag{2.4}$$

where σ_{Tel} is the total elastic cross section and σ_{T1}, σ_{T2} etc. are the total cross sections for the various inelastic processes that are energetically possible. The grand total cross

section is usually measured in attenuation experiments (see, for instance, Golden and Bandel, 1965), where the transmitted, rather than the scattered, electrons are detected.

In the current electron scattering experiments, measurements are made of the number of electrons elastically scattered from a neutral target atom, at a specific scattering angle, as a function of energy. This quantity is proportional to the elastic differential cross section, which can be seen by the relationship given in equation 2.2.

2.1.3 Partial wave analysis of electron-atom scattering

In principle, electron scattering from a single atom can be described by the Schrödinger equation

$$H\Psi = E\Psi \tag{2.5}$$

In the case of non-relativistic, elastic scattering, with the centre of mass of the system stationary relative to the laboratory frame, the solution to the Schrödinger equation can be written as

$$\Psi(\boldsymbol{r},t) = \psi(\boldsymbol{r})e^{-iEt/\hbar} \tag{2.6}$$

where $\boldsymbol{r}$ is the position of the incoming electron.

The incident wave function can be closely approximated to be a plane wave, so that it can be expressed as $\psi_{inc}(\boldsymbol{r}) = Ae^{ikz}$, with the z direction being the direction of propagation of the incident electron. The scattered wave function can be expressed as a spherical outgoing wave, which, for large r, is given by

$$\psi_{sc}(\boldsymbol{r}) \sim \frac{A}{r} f(\theta)e^{ikr} \tag{2.7}$$

where A is a constant and $f(\theta)$ is called the scattering amplitude. The scattering amplitude is related to the differential cross section by the expression

$$\frac{d\sigma}{d\Omega} = |f(\theta)|^2 . \tag{2.8}$$

Therefore, to determine the elastic differential cross section for any given scattering system, all that is needed is the scattering amplitude.

In order to find an expression for $f(\theta)$ in the case of electron scattering from an atom, it can be shown that (McDaniel, 1989)

$$\psi(r,\theta)=\sum_{l=0}^{\infty}(2l+1)i^l e^{i\eta_l}P_l(\cos\theta)\frac{1}{kr}\sin\left(kr-\frac{l\pi}{2}+\eta_l\right) \qquad (2.9)$$

where $P_l(cos\theta)$ are the Legendre polynomials of order l, where, in this case, l is the orbital angular momentum.

As $\psi_{sc} \sim f(\theta)\frac{e^{ikr}}{r}$ it can then be shown that

$$f(\theta)=\frac{1}{2ik}\sum_{l=0}^{\infty}(2l+1)\left(e^{2i\eta_l}-1\right)P_l(\cos\theta) \qquad (2.10)$$

$$=A+iB \qquad (2.11)$$

where,

$$A=\frac{1}{2k}\sum_{l=0}^{\infty}(2l+1)\sin(2\eta_l)P_l(\cos\theta) \qquad (2.12)$$

$$B=\frac{1}{2k}\sum_{l=0}^{\infty}(2l+1)\left(1-\cos(2\eta_l)\right)P_l(\cos\theta). \qquad (2.13)$$

and

$$\frac{d\sigma}{d\Omega}=A^2+B^2 \qquad (2.14)$$

The terms η_l in these expressions are called the phase shifts, and they are functions of the incident energy. The number of phase shifts that make significant contributions to the differential cross section varies depending upon the energy of the incident electrons and the electronic structure of the target atom. The variation of the differential cross section with scattering angle can then be understood by taking into account the contributions from different phase shifts to the scattering amplitude. For $l=0$, η_l is called the s-wave phase shift, $l=1$ gives the p-wave phase shift, and so on for higher angular momentum.

The Hamiltonian for the scattering system can be thought to consist of many different interaction potentials. A common expression for the Hamiltonian is

$$H=T+V_{st}+V_{ex}+V_{pol}+.... \qquad (2.15)$$

Here, T is the kinetic energy operator for the system, V_{st} is the static Coulomb potential, which takes into account the electrostatic interaction between the incident electron and the nucleus and target electrons, V_{ex} is the exchange potential which takes into account the indistinguishability of the electrons and models the interaction where the incident

electron exchanges with one of the target electrons, and V_{pol} is the polarisation potential which takes into account the distortion of the target charge cloud by the incident electron. Approximation methods attempt to model the various potentials that contribute to the Hamiltonian of the system. For different target atoms, and different scattering energies and angles, the scattering process will be sensitive to different parts of the interaction potential, and this must be taken into account when attempting to solve the scattering problem. Various approximations are used in theoretical approaches to the scattering problem to calculate both $f(\theta)$ and η_l, as the precise description of all but the simplest atomic system is impossible. At low energies the partial wave analysis method is particularly useful, as the number of partial waves that need to be included is relatively low, and by choosing an appropriate (low) number of phase shifts, the calculation of the cross sections can be made significantly easier.

2.2 Negative ion resonances

2.2.1 Introduction

Negative ion resonances occur in electron scattering when an incident electron is temporarily trapped by the target atom or molecule, forming a negative ion state with a lifetime of 10^{-12} to 10^{-14} s, which is significantly longer than the typical direct scattering time (10^{-15} to 10^{-16} s). These resonances generally occur at well defined energies and appear typically as sharp structures in scattering or excitation cross sections, with the width of the resonance being inversely proportional to the lifetime of the negative ion state. The shape of the resonance structure in the energy dependence of the measured cross section is essentially due to interference between the electron ejected in the decay of the negative ion state and the directly scattered electrons. Theoretical models of negative ion resonances present difficulties as the extra electron in the problem is usually weakly bound to the target particle, and is often in a doubly excited state in which electron correlation effects can have a large influence. This means the system cannot be easily described by the independent particle approach that is generally used for the formulation of scattering from a neutral target. In addition to conventional electron scattering approaches, new methods have been introduced which place a high

importance on effects which are significant in negative ions but less so in neutral systems, such as electron-electron correlation. The development of theory in this area has, as a consequence, also led to a greater understanding of correlated systems, introducing concepts such as quantum numbers for pairs of electrons to aid in the description of these systems.

An overview of the different theoretical approaches used in calculating negative ion resonances is given in this section. For a more comprehensive review, Buckman and Clark (1994) provides an excellent reference, and this has been used as a guide, in part, for the preparation of this section.

2.2.2 Classification schemes

In this section, two general schemes that describe negative ion resonances will be discussed. The first of these is the parent-grandparent scheme and the second labels temporary negative ions as either shape or Feshbach resonances.

The parent-grandparent model was first proposed by Schulz in his review "Resonances in Electron Impact on Atoms" in 1973. A parent-type resonance is one which can be viewed as an electron bound to a neutral target in either its ground or an excited state, the parent state. For instance, this description is appropriate for the $5s^25p\ ^2P$ resonance seen by Burrow et al. (1976) at 0.33 eV in cadmium. In the grandparent model, the incident electron is correlated with one of the target electrons in the formation of the resonance and this doubly-excited complex is then weakly bound to the grandparent state, which in this case is the a singly charged positive ion core. The grandparent scheme has been demonstrated to be highly appropriate for the description of the $(n\text{-}1)p^5nln'l'$ resonances seen in electron-rare gas scattering by Brunt et al. (1976) and Buckman et al. (1983b), for instance.

Categorising resonances as “shape” or “Feshbach” is perhaps a more common terminology. A shape resonance is formed when the incident electron is trapped by a potential barrier which is a property of the target atom. The potential barrier is formed from a combination of the atomic mean field which is an attractive potential, and the centrifugal potential, which is repulsive. Shape resonances typically lie energetically

above their parent state and decay preferentially into this state, resulting in short lifetimes and correspondingly large energy widths. In the case of Feshbach resonances, the extra electron gives energy to internal degrees of freedom of the target and is then ejected when the energy is transferred back to the electron. A Feshbach resonance is essentially an excited state of the negative ion with the electron trapped in a potential associated with an excited neutral state. Feshbach resonances lie near to, but below, the parent state in energy and are thus unable to decay into this state. As a result, they are usually long lived, and have a correspondingly narrow natural width.

2.2.3 Resonances in electron scattering

In conventional electron scattering theory, an approximate solution to the non-relativistic, many-body Schrödinger equation is found to determine the various scattering parameters. The usual approach is to assume that there is only a weak interaction between the electrons in the system, which does not have to be explicitly taken into account. This is known as the independent particle approximation. In calculating parameters for negative ion resonances in electron scattering using these methods, the theoretical approach is not substantially different. However, as mentioned previously, this conventional approach is made more difficult by the correlated states which lead to typically diffuse orbitals. This means that larger regions of configuration space have to be accounted for in the calculations, adding to their complexity.

In the idealised situation of a resonance appearing in a single partial wave, the phase shift, δ_r, due to that resonance can be expressed as a function of the incident electron energy, E, as

$$\delta_r = \tan^{-1}\left[\frac{\Gamma}{2(E_r - E)}\right], \tag{2.16}$$

where E_r is the resonance energy and Γ is the width (FWHM in energy) of the resonance. In this case the phase shift will increase by π radians as the incident electron energy increases through E_r (see, for instance, Joachain 1975). The scattering amplitude for this partial wave is then given by

$$f_l(\theta) \approx \frac{(2l+1)}{k} \exp i\delta_r \sin \delta_r P_l(\cos\theta), \tag{2.17}$$

and the total elastic cross section, σ_l^{el}, by

$$\sigma_l^{el}(k^2) \approx \frac{4\pi(2l+1)}{k^2} \sin^2 \delta_r . \tag{2.18}$$

This formula is known as the one-level, Breit-Wigner resonance formula, and it gives a Lorentzian profile in σ_l^{el}.

In practice, a smoothly varying background phase shift is added to the resonant phase shift to obtain the total phase shift in the region of the resonance, in that way accounting for the non-resonant contributions to the cross section.

Of course, a major drawback to this approach is that it fails to take into account the possible presence of the resonance in other partial waves, meaning that this method is only of limited practical application. The above equation (2.16) has been generalised by Hazi (1979) to include multichannel scattering, to give an expression for the eigenphase sum:

$$\Delta = \sum_n \delta_n = \Delta^0 + \tan^{-1}\left(\frac{\Gamma}{2(E_0 - E)}\right) \tag{2.19}$$

where Δ^0 is the sum of the background eigenphases:

$$\Delta^0 = \sum_n \delta_n^0 . \tag{2.20}$$

Whilst a useful tool, this approach tends only to be used in a qualitative manner (see, for instance, Scott et al., 1984) due to other complicating factors. One of these factors is that the behaviour of resonances can be affected by their proximity to excitation thresholds, a situation applying to many experimentally observed resonances. The possibility of overlap with other resonances also needs to be taken into account. These factors then impose other constraints upon the description of resonances in terms of their phase shifts, which will not be covered here. Resonances can occur in many kinds of scattering calculations, and some examples of these will be briefly outlined.

The first example is single channel scattering calculations. In a single channel calculation of resonance parameters, a single fixed atomic state target is used, meaning that it is not possible to account for inelastic processes. This allows only a single-

electron effective potential, with the result that it is only possible to calculate the properties of shape resonances associated with the ground state in this approximation. In this case, exchange is typically taken into account using a Hartree-Fock or a Dirac-Fock approximation with an ad hoc calculation of the target polarisation potential (Buckman and Clark, 1994). This approach has been used, for instance, by Sin Fai Lam (1981) to calculate low energy shape resonances in beryllium, zinc, cadmium and mercury. In this case, Dirac-Fock wavefunctions were used to describe the target atom, with a second order Dirac potential to account for relativistic effects.

Another approach is the use of close-coupling calculations. In the close-coupling approximation, the wave function of the N+1 electron system is expanded such that:

$$\Psi(\boldsymbol{r}_1,\boldsymbol{r}_2,\ldots\boldsymbol{r}_{N+1})=\mathcal{A}\sum_k \Phi_k(\boldsymbol{r}_1,\boldsymbol{r}_2,\ldots\boldsymbol{r}_N)f_k(\boldsymbol{r}_{N+1}) \qquad (2.20)$$

where Φ_k are fixed eigenstates of the target atom, $\mathcal{A}$ is an antisymmetrisation operator on the N+1 electron wave function and f_k are the scattering orbitals that are to be found. Φ_k are usually described using Hartree-Fock or configuration-interaction wave functions (Buckman and Clark, 1994). This approach can account for electron-target interactions and inelastic processes, unlike the single channel approximations described previously. Examples of close-coupling calculations can be found in the work of Moores and Norcross (1972, 1974) on electron scattering from sodium and photodetachment of Li^-, Na^- and K^-, and also in work by Taylor and Norcross (1986) on photodetachment of K^-.

The final example of an approximation for scattering calculations is the R-matrix technique. The R-matrix method of calculating scattering parameters has been developed at Queen's University, Belfast (for example see Burke et al. (1969) and Berrington et al. (1975)), and has been used in calculations on many atoms. It treats the problem in two parts, the first being the whole N+1 electron system enclosed in a sphere of radius r_0 with fixed boundary conditions for the electron wave functions at $r=r_0$. Only one electron, then, is allowed in the region outside this sphere. The electrons within the sphere are treated using standard configuration-interaction techniques

(Buckman and Clark, 1994), whereas the region outside the sphere is described using the close coupling description of equation 2.20 and the boundary conditions at $r=r_0$, reducing the problem in this region to an electron scattering from a radial potential. In general, r_0 has to be large for calculations on negative ions to account for the diffuse nature of the excited states of the target, meaning that the calculations are correspondingly more difficult. For instance, Pathak et al. (1988) used r_0=83 a.u. to calculate resonance states of H^-, whereas typical calculations for atomic systems using the R-matrix method have $r_0 \leq 10$ a.u. A prime advantage of the R-matrix approach is that computational effort is concentrated within the sphere of $r<r_0$, where electron correlation effects dominate, with the region outside the sphere being treated in a more simplified manner (Kim and Greene, 1989). The R-matrix approach has also been quite successful in the application to He^- resonances (see Burke et al. (1969), Fon et al. (1978) and Fon et al. (1989) for example).

2.2.4 Calculations of resonance states

Another approach to the determination of the properties of negative ion resonances is to attempt to calculate the energy of the states in the same way that it is possible to calculate the energy levels of a neutral atom. Of course, this approach is substantially complicated by the fact that negative ion resonances, by their very nature, are not bound states, but rather transient states of the negative ion.

Several different approaches have been developed to treat the problem in this way. The first of these is the use of Feshbach projection operators, which "turn off" any interaction between the resonant state and any continuum channels. This then allows the energy of the resonant state to be calculated, appearing as an eigenvalue of the transformed problem. After this is completed, the width of the resonance and any shift due to interaction with the continuum have to be calculated, generally by use of perturbation theory (Buckman and Clark, 1994). This projection operator method has been used for calculations of low energy resonances in simple sytems, such as the $2s^2\ ^1S$ resonance in atomic hydrogen (Bhatia and Temkin, 1981), but has yet to be used for

targets with more than two electrons, or where many continua are present (Buckman and Clark, 1994).

Another approach has been to frame the state calculation in complex variables, a technique first introduced in nuclear physics by Siegert (1939). In the case of s-wave scattering from a spherically symmetric potential, *V(r)*, a resonance occurs when:

$$\frac{\partial \phi}{\partial r} = ik\phi \quad at\ r = r_0 \tag{2.21}$$

(Buckman and Clark, 1994) with ϕ the reduced radial wave function, $k = \sqrt{2\varepsilon}$ and r_0 the radius beyond which *V(r)=0*. ε is the complex energy, $E_0 - i\Gamma/2$, and this gives the Briet-Wigner form of the cross section in the region of the resonance, as given in equation 2.17. If long range forces are present however, such as a target polarisation potential, this approach will only be applicable for $r_0 \to \infty$. This was addressed by Nuttall (1972) by making *r* a complex number as well, which overcame the problem and allowed the calculation to be performed in the same manner as is used for the calculation of bound state wavefunctions. A different approach to the complex coordinate scaling, which is more commonly used, involves scaling the coordinates of all the particles in the system by $e^{-i\theta}$, which gives rise to solutions of the new Hamiltonian which have the form $\varepsilon e^{-i\phi}$, giving the complex energies corresponding to negative ion resonances. This approach was first used by Doolan et. al. (1974) to calculate the $2s^2\ ^1S$ resonance in H^-. Since then, many calculations have been performed for H^- resonances, as reported by Ho (1992), some calculations on He^-, for instance by Junker (1982a,b) and Ne^- by Bentley (1991). Calculations have also been made of the so called "b resonances" (Buckman and Clark, 1994) for the alkaline earth elements, the first of which was a calculation for Be^- by Rescigno et al. (1978) followed by various other calculations, mainly by the same authors.

The final approach taken towards the calculation of negative ion resonance states is to use so called "stabilization" techniques in conjunction with conventional bound state calculations, to eliminate interactions with the continuum (Buckman and Clark, 1994). In this case, a transient localisation of the wave function in configuration space gives rise to a resonance and, if successive, larger sets of basis functions are taken to

solve the appropriate Hamiltonian, one eigenfunction will converge to the resonant solution. This method has been used by Weiss and Krause (1970) to calculate resonances in Ar^- and Ne^- and also by Lipsky et al. (1977) to calculate resonances in H^- below the H(n=3) threshold.

2.2.5 Approaches incorporating electron correlations

The approximations in the previous sections either ignore the effect of electron-electron interactions, or deal with them only superficially. However, the nature of negative ion resonances suggests that correlated electron motion can play a large part in the formation of the negative ion state. Several approaches have been developed which attempt to directly include these electron correlations into the calculation of resonance parameters.

For a two electron system, with a large positive core, it seems that a natural way of framing the problem is to use hyperspherical coordinates (R, α, θ_{12}), defined as:

$$R = \sqrt{r_1^2 + r_2^2},$$
$$\alpha = \arctan(r_2/r_1)$$
$$\theta_{12} = \arccos\left(\frac{\mathbf{r_1} \cdot \mathbf{r_2}}{r_1 r_2}\right). \qquad (2.22)$$

Here $\mathbf{r_1}$ and $\mathbf{r_2}$ are the electron-nucleus separations, and it is assumed that the nuclear mass is infinite. R is called the hyperradius and provides a measure of the separation of the two electron system from the nucleus, α gives a measure of the relative sizes of the distance of each electron from the nucleus, and θ_{12} is a measure of the angle between the two electrons. This approach was first introduced into atomic physics by Fock (1958), and was first used in the analysis of resonance phenomena by Macek (1968). By using hyperspherical coordinates to frame the problem, new quantum numbers arise that are unique to the picture of the atom with some sort of correlated electron motion, which is quite different to the independent particle model. One of the advantages of this approach is that it gives a good qualitative understanding of the physical processes involved with resonance phenomena. Calculations using this approach have been done by Fukuda et al. (1987), Koyama et al. (1989) and Sadeghpour (1991) on the H^-

resonances, and the approach has been extended to systems with more than two electrons by, for instance, Lin (1983) on Li^-, Christiensen-Dalsgaard (1988) on the alkalis and LeDourneuf and Watanabe (1990) on He^-.

Another approach that explicitly deals with electron correlations is the so-called Wannier theory. This was first developed by Wannier (1953) to explain electron impact ionisation. Wannier theory predicts that at near-threshold energies, double escape (single ionisation) is only possible under very specific conditions, when θ_{12}•• and α••/4, that is when the electrons are equidistant from the ion core and on opposite sides of it (referring to the definition of these coordinates above). This region appears as a ridge in the potential surface for two electrons external to a single postive charge, as shown in figure 2.2 (after Lin 1974). By applying this scheme to the resonance problem, it can be shown (for example, see Buckman and Clark, 1994) that it gives rise to a Rydberg series of resonances converging on the threshold for electron escape. Fano (1980) first proposed the existence of resonance states in helium based on this model, and Buckman et al. (1983a) and Buckman and Newman (1987) used this idea to analyse the resonances series that they observed in electron-helium scattering. Since then, many other systems have been found to have resonances that can be described by this scheme (see Buckman and Clark, 1994).

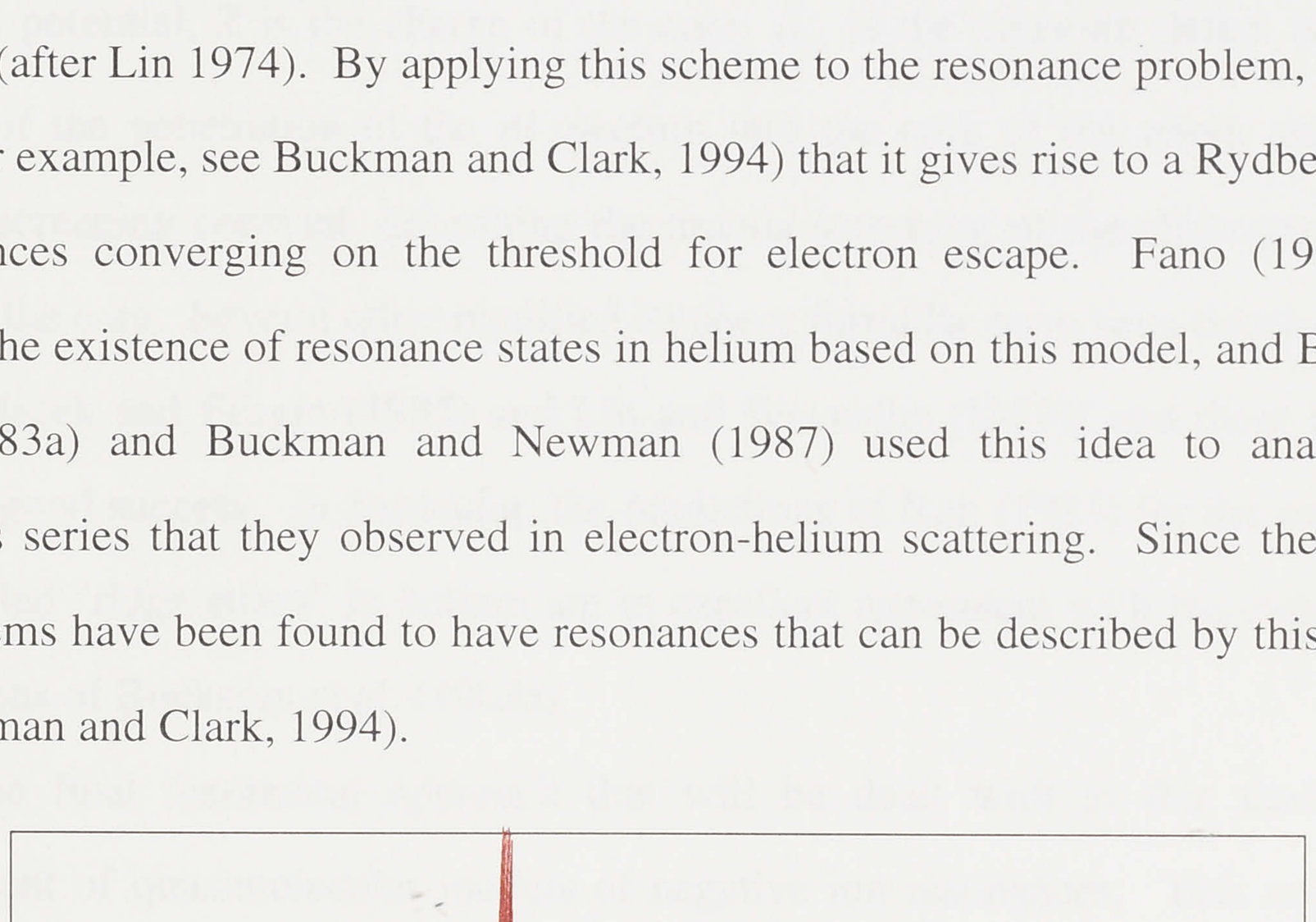

Figure 2.2: Wannier potential ridge for two electrons in the presence of a positive core

Other, semi-empirical approaches have been used as aids in the description of doubly-excited states of both neutral and negative ion systems. Heddle (1977) and Read (1977, 1982) developed a modified Rydberg formula, which fits the resonance series in He^- quite well, and also predicts the lowest lying negative ion resonances of the other noble gases, as well as being quite successful in predicting the electron affinities of the alkali atoms. This formula is given as

$$E_{nlnl'} = I - \frac{R(Z-\sigma)^2}{(n-\delta_{nl})^2} - \frac{R(Z-\sigma)^2}{(n-\delta_{nl'})^2} \qquad (2.22)$$

(Read 1977) where $E_{nlnl'}$ is the energy of configurations of the type [core]$nlnl'$, I is the ionisation potential, Z is the charge of the core, δ_{nl} is the quantum defect which is a measure of the penetration of the nl electron into the core of the atom, and σ is an effective screening constant, describing the mutual screening of the electrons from the charge of the core. Several other modified Rydberg formulae have been developed (Rau (1983), Macek and Feagin (1985) and Lin and Watanabe (1987)) and these have also met with good success. In particular, the predictions of Rau (1983) for the energies of the so-called "ridge states" in helium are in excellent agreement with the experimental observations of Buckman et al. (1983a).

The final theoretical approach that will be dealt with in this thesis is the development of quasimolecular models of negative ion resonances. This came about after the observation of series of resonances, indicating that it might be possible to indentify excitation channels for a two electron system in the same way that it is possible to indentify vibrational excitation channels in molecules. Rost and Briggs (1988), Feagin and Briggs (1986, 1988) and Rost et al. (1991) identified an alternative set of coordinates to describe the collective motion of two electrons, and identified excitation channels corresponding to an asymmetric stretch mode, symmetric stretch mode and a bending mode in triatomic molecular excitation, assuming in this case that the nucleus remains stationary. This approach was used quite successfully to calculate energies for doubly excited states. Richter and Wingen (1990) found that the Wannier configuration described above was unstable, and instead identified a two electron orbit with $\alpha = \bullet/4$ and oscillation about $\theta_{12} = \bullet$, again resembling the bending mode of a

triatomic molecule. In the final example of this approach, Klar (1986) proposed a rigid rotor type motion for two electron systems with Z=1, with $\alpha=\pi/4$ and $\theta_{12} \sim 78^{o}$.

Chapter 3

Experimental apparatus

3.1 General description

The electron scattering experiments described in this thesis were carried out on a Crossed Beam Apparatus (CBA), which consists of a monoenergetic beam of electrons crossed at right angles to a neutral atomic beam. Elastically scattered electrons were detected in the plane of the incident electron beam, normal to the atomic beam, by two rotatable electron detectors which can access an angular range from 24° to 122°. Photon decay spectra were obtained by detecting photons from collisionally excited atoms with a photomultiplier tube, placed orthogonal to both the electron and atomic beams. A metastable atom detector was able to be placed in the path of the incident target beam, allowing metastable excitation experiments to be performed on argon.

The experimental apparatus can be divided into two main sections, situated in separate, differentially pumped chambers. The first (lower) chamber contains the target source providing either a metal vapour beam, or a gaseous nitrogen or argon beam. Production of a metal vapour beam is achieved by a high temperature oven, heated using coaxial resistive heaters. The oven's exit aperture is a needle which protrudes into the top chamber to a point just below the electron beam, giving the greatest possible beam density in the interaction volume. The other beam source used is a gas line which admits either argon or nitrogen gas into the lower chamber and this forms a diffuse gas beam which flows into the top chamber, allowing electron scattering experiments to be performed on these systems for the purpose of characterisation of the electron monochromator. The second (upper) chamber contains the electron spectrometer, electron detectors, a photomultiplier for decay photon detection and a cold trap to

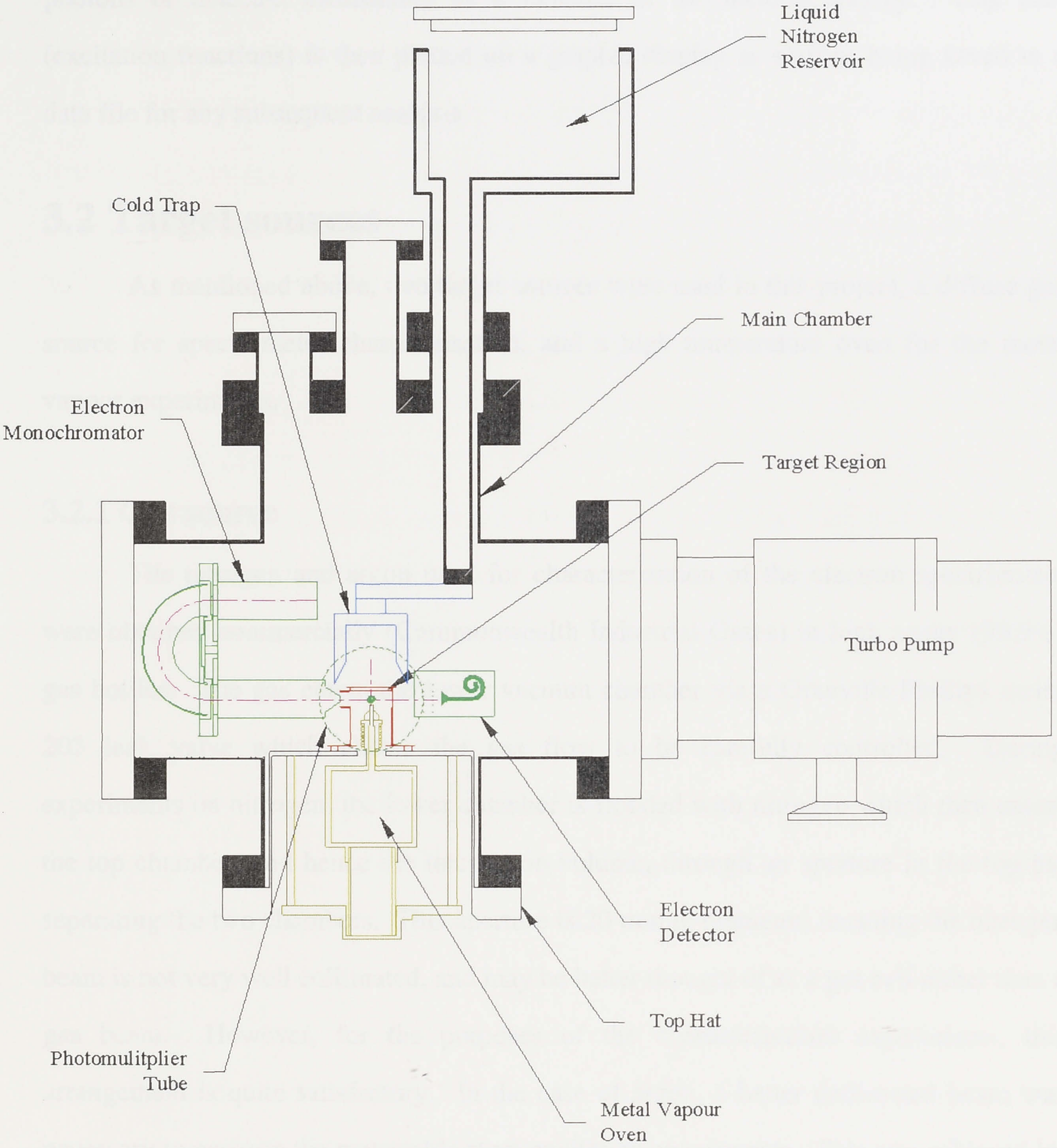

Figure 3.1: Schematic diagram of crossed beam apparatus

collect the metal vapour beam. For metastable excitation experiments on argon, a metastable detector replaced the cold trap. The chambers are separated by a stainless steel top hat with a large (20 mm) aperture through which the heated needle of the oven protrudes. A schematic diagram of the apparatus is shown in figure 3.1.

Data collection is computer controlled. The measurements involve scanning the energy of the incident electron beam, along with the appropriate elements of the electron spectrometer, whilst collecting the number of scattered electrons, emitted

photons or detected metastables as a function of the incident energy. This data (excitation functions) is then plotted on a graphic display as well as being saved to a data file for any subsequent analysis.

3.2 Target sources

As mentioned above, two target sources were used in this project, a diffuse gas source for spectrometer characterisation, and a high temperature oven for the metal vapour experiments.

3.2.1 Gas source

The nitrogen and argon used for characterisation of the electron spectrometer were obtained commercially (Commonwealth Industrial Gases) in high purity (99.9%) gas bottles. The gas enters the lower vacuum chamber via a Granville-Phillips series 203 leak valve which allows the gas flow to be carefully controlled. During experiments on nitrogen, the lower chamber is flooded with nitrogen which then enters the top chamber, and hence the interaction volume, through an aperture in the top hat separating the two chambers. This aperture is 20 mm in diameter, meaning the nitrogen beam is not very well collimated, and may be better thought of as a gas cell rather than a gas beam. However, for the purposes of the characterisation experiments, this arrangement is quite satisfactory. In the case of argon, a better collimated beam was necessary to perform the metastable atom excitation experiments. This was achieved by using a teflon line connected to the gas input which terminated in a stainless steel needle (0.7 mm internal diameter) protruding into the upper chamber. This provided a reasonably well collimated beam of argon atoms, most of which could be directed into the metastable detector above the intersection of the atom and electron beams.

3.2.2 Metal vapour oven

At the commencement of this project, the metal vapour oven in use on the CBA consisted of a molybdenum crucible containing the desired metal, heated both radiatively and by electron bombardment from three tungsten filaments. This form of

heating was used as the oven was intended for the study of a number of atomic systems which require a high temperature (>1000°C) oven, such as lead and copper. The metal vapour beam resulting from this was collimated by a series of apertures before passing into the top chamber for electron scattering experiments. This arrangement, however, proved unsatisfactory as the collimating apertures would block after approximately 12 hours of operation, meaning that the oven had to be taken out of the vacuum chamber and cleaned regularly. This did not allow sufficient time to carry out the required experiments and required regular intervention to ensure proper operation, so it was decided to design and construct a new oven which would require less maintenance and thus provide longer periods of operation without intervention. The temperatures that are required for atomic beam experiments on cadmium and magnesium are relatively low (<500°C), and can be readily achieved by standard resistive heating. The advantage of this approach is that the design and construction of an oven using this method of heating is much simpler than for a filament-heated oven, and it also allowed the exit aperture of the oven to be a heated needle which extends to just 2 mm below the interaction volume, formed by the intersection of the electron and atomic beams. Stray magnetic fields from the heating wires are minimised as coaxial heaters (Thermocoax) are used and the connecting wires return along almost the same path as they enter, effectively cancelling out the magnetic field produced. This design also avoids other problems associated with filament heated ovens, such as stray electron emission, as well as avoiding the need for collimating apertures which have a tendency to block.

The oven consists of two parts, a crucible containing the desired metal and a heated needle exit. The crucible is a stainless steel cylinder of internal diameter 56 mm and height 49 mm, giving a volume of approximately 120 cc. Approximately ten turns of Thermocoax heating wire is wrapped around the exterior of the crucible, enabling it to be heated to the desired temperature. The exit to this crucible is connected by a short piece of stainless steel tubing to a heated needle, which extends to 2 mm below the axis of the electron beam in the upper chamber. The needle is embedded in a copper block which is also wrapped in the Thermocoax heating wire. Chromel-alumel (type K) thermocouples are located at the base of the crucible and the top of the needle, allowing

the temperature of the needle to be controlled and monitored separately to the crucible. During the operation of the oven the needle is kept at a higher temperature than the crucible to prevent clogging. For production of a cadmium beam the needle was heated to approximately 270°C, with the crucible held at approximately 225°C, corresponding to a vapour pressure of approximately 1 mTorr. This required a current of approximately 0.75 amps through the heating wires for the needle, and 1.1 amps through those for the crucible in this configuration. To obtain the same vapour pressure for magnesium, operating temperatures of 390°C and 375°C were required for the needle and crucible respectively.

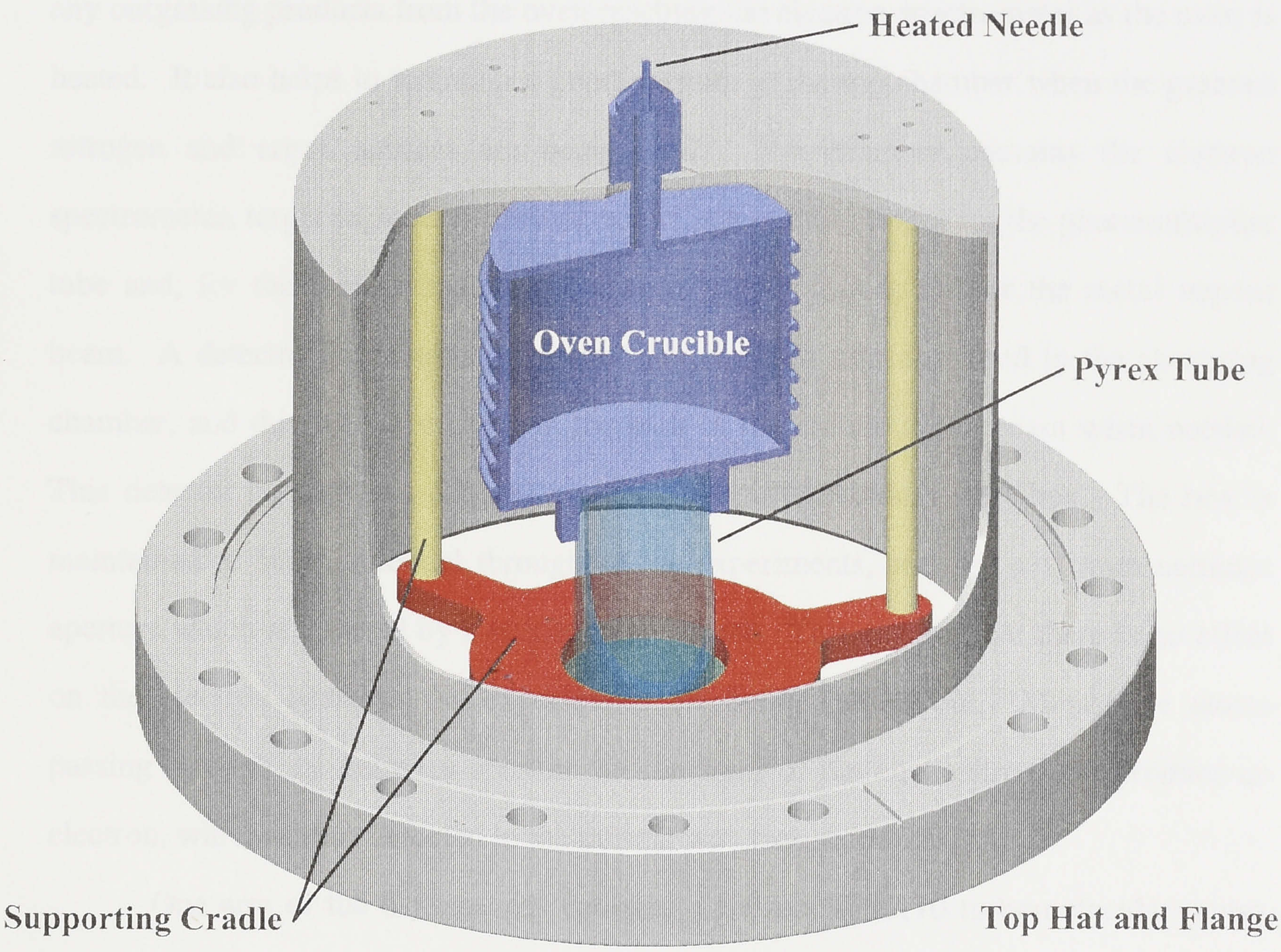

Figure 3.2: Schematic diagram of oven assembly

The oven assembly is suspended from the top hat that separates the two chambers by means of a purpose-built cradle. The oven itself stands on a 60 mm high pyrex tube, so as to isolate the oven both thermally and electrically from the cradle, and hence the top hat, which is maintained at ground potential. In this way, heat loss by thermal conduction is minimised, and the oven can be kept at the same potential as the

incident electron beam, so that the electron beam passage through the interaction region is not affected. A schematic diagram of the oven is shown in figure 3.2.

3.3 Scattering chamber

The scattering chamber is a commercial (MDC corporation), 6-way cross with arms 152 mm (6 inches) in diameter and extending 165 mm from the centre of the chamber. It has a volume of approximately 13 litres. The scattering chamber is separated from the oven chamber by a stainless steel top hat containing a 20 mm aperture, which allows the two chambers to be differentially pumped, and minimises any outgassing products from the oven reaching the electron spectrometer as the oven is heated. It also helps to maintain a good vacuum in the top chamber when the gaseous nitrogen and argon sources are being used. The chamber contains the electron spectrometer, target region, electron detectors, a re-entrant finger for the photomultiplier tube and, for the metal vapour experiments, a cold trap to collect the metal vapour beam. A detector for metastable excited argon atoms was also used in the scattering chamber, and this was positioned in the path of the atomic argon beam when needed. This detector consist of a channeltron contained in a stainless steel box. The box is maintained at beam potential throughout the experiments, and has a 10 mm entrance aperture which is covered by a stainless steel mesh. This ensures that there is no effect on the electron beam as the experiments are being carried out. Metastable atoms passing through the entrance aperture hit the front of the channeltron and produce an electron, which is then detected in the normal way (see section 3.7).

One arm of the 6-way cross contains a Balzers TPU170 turbomolecular pump, with a pumping speed of 170 l/s, which is used to evacuate the chamber. A second turbomolecular pump is located on the lower chamber to provide the differential pumping for the target source. Both pumps are backed by a Balzers DUO 2.5A backing pump and the base pressure in the upper (scattering) chamber is typically 1 x 10^{-8} Torr, with no gas load. An UHV nude ion gauge (MDC corporation) is used to monitor the pressure inside the chamber and is mounted on a 2.75 inch feedthrough located on another of the "arms" of the six way cross.

A second arm of the chamber has a 6 inch glass window through which the experiment may be observed. This is particularly useful for observing metal deposition on the interior of the apparatus, allowing it to be monitored and cleaned when necessary.

The electron spectrometer is mounted on a flange and enters the chamber horizontally, opposite the window. The spectrometer exit aperture is aligned so that the electron beam crosses at right angles to the target beam in the centre of the chamber and is collected by a Faraday cup mounted from the top hat. The operation of the electron spectrometer is discussed in detail in section 3.4.

The top flange of the chamber contains a number of electrical feedthroughs mounted on conflat flanges, a feedthrough for the cold trap and a rotating shaft feedthrough from which the rotatable electron detectors are mounted. The cold trap is a copper cylinder approximately 50 mm in diameter which extends to just above the target region. It is mounted from a re-entrant tube which extends into the chamber from the top flange. The tube is connected externally to a crucible which is filled with liquid nitrogen by an automatic controller. The trap is mounted from the liquid nitrogen cooled finger via a copper bar and alumina spacer, which electrically isolates the trap whilst keeping the two in good thermal contact. In this way, the copper trap can be maintained at -200°C and at the same potential as the electron beam, thus trapping the metal vapour beam without affecting the passage of the electron beam.

The cooling and trapping system is pictured in figure 3.3. The hot metal vapour condenses on contact with the colder surface of the copper trap, thus preventing condensation on other, less desirable surfaces such as the electron optics or other electronics contained inside the vacuum chamber. Despite this measure, the apparatus has to be periodically cleaned of metal deposits, as the trap is not 100% efficient in collecting the metal vapour.

An alternative design based on the high voltage trap proposed by Bauman and Martin (1995) was also tried in an attempt to improve the efficiency of the trapping of the cadmium beam. This design did not make any substantial improvement upon the trapping efficiency, with the critical factor being the collection angle of the trap rather

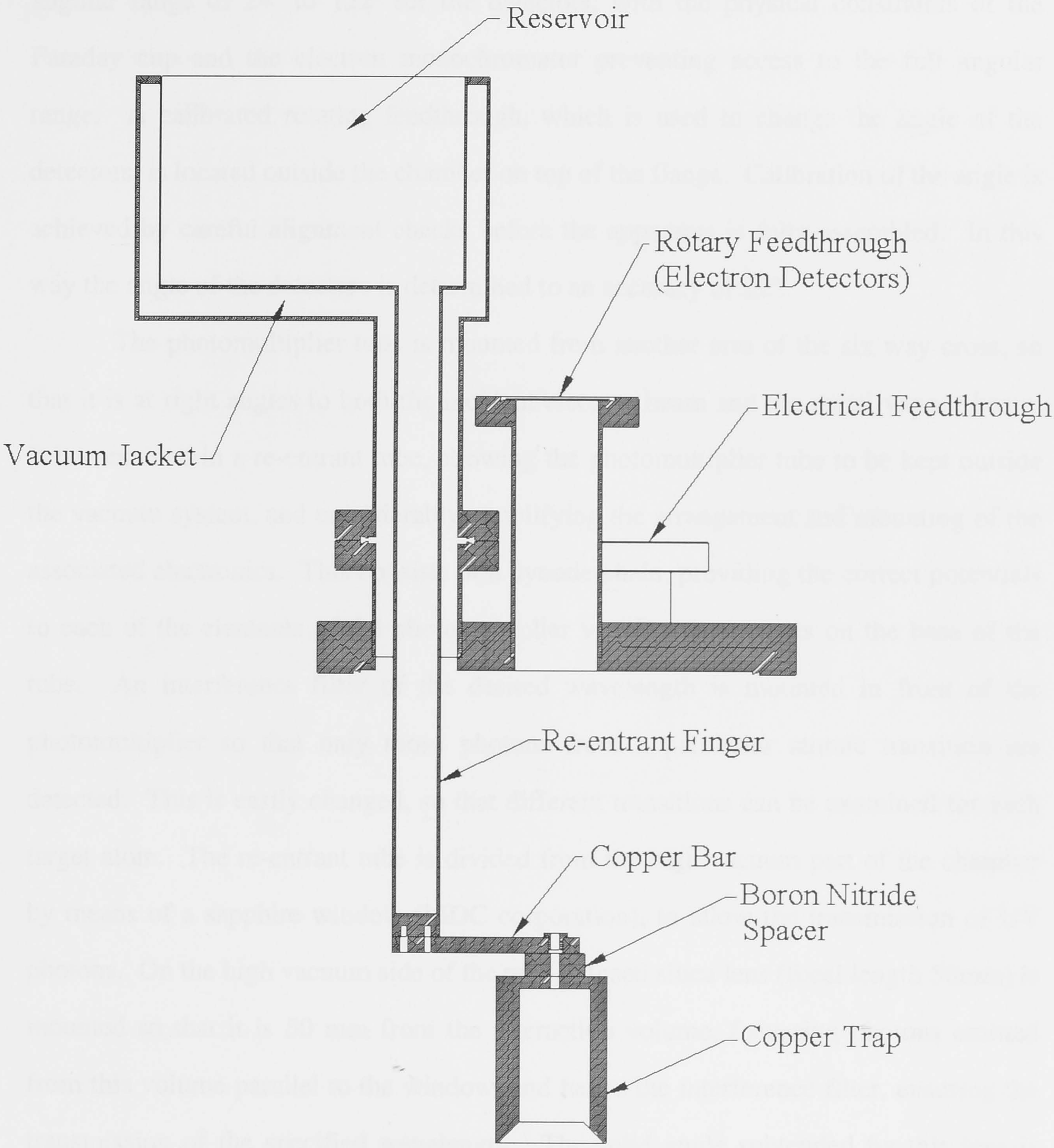

Figure 3.3: Schematic diagram of liquid nitrogen cooling system

than the high voltage element. As a result it was decided not to continue using this design, and instead to use the simpler, liquid nitrogen cooled trap.

Two electron detectors are supported by a rotating, circular platform mounted from the top flange. These detectors are connected to the bottom of two stainless steel pillars which are bolted to the platform, allowing them to rotate in the plane of the electron beam, at right angles to the metal vapour beam (the scattering plane). These detectors are further discussed in section 3.7. The turntable can provide access to an

angular range of 24° to 122° for the detectors, with the physical constraints of the Faraday cup and the electron monochromator preventing access to the full angular range. A calibrated rotating feedthrough, which is used to change the angle of the detectors, is located outside the chamber on top of the flange. Calibration of the angle is achieved by careful alignment checks before the apparatus is fully assembled. In this way the angle of the detectors is determined to an accuracy of ±2°.

The photomultiplier tube is mounted from another arm of the six way cross, so that it is at right angles to both the incident electron beam and the metal vapour beam. It is contained in a re-entrant tube, allowing the photomultiplier tube to be kept outside the vacuum system, and considerably simplifying the arrangement and mounting of the associated electronics. This consists of a dynode chain, providing the correct potentials to each of the elements of the photomultiplier via electric contacts on the base of the tube. An interference filter of the desired wavelength is mounted in front of the photomultiplier so that only those photons from a particular atomic transition are detected. This is easily changed, so that different transitions can be examined for each target atom. The re-entrant tube is divided from the high vacuum part of the chamber by means of a sapphire window (MDC corporation), to allow the transmission of UV photons. On the high vacuum side of the tube, a fused silica lens (focal length 50mm) is mounted so that it is 50 mm from the interaction volume, focussing photons emitted from this volume parallel to the window, and hence the interference filter, ensuring the transmission of the specified wavelength. The solid angle subtended by this lens is approximately 0.2 steradians. A more detailed description of the photomultiplier tube and its operation is given in section 3.8.

3.4 Electron spectrometer

3.4.1 Overview

The electron beam is produced by thermionic emission of electrons from a thoriated tungsten filament. Emitted electrons are extracted, energy analysed and collimated by a set of electron optics, referred to as the electron spectrometer.

The electron spectrometer can be divided into four basic components, the extraction optics, an initial set of transport and focussing optics - the "gun" optics, a hemispherical electrostatic energy analyser, and a second set of optics - the "target"

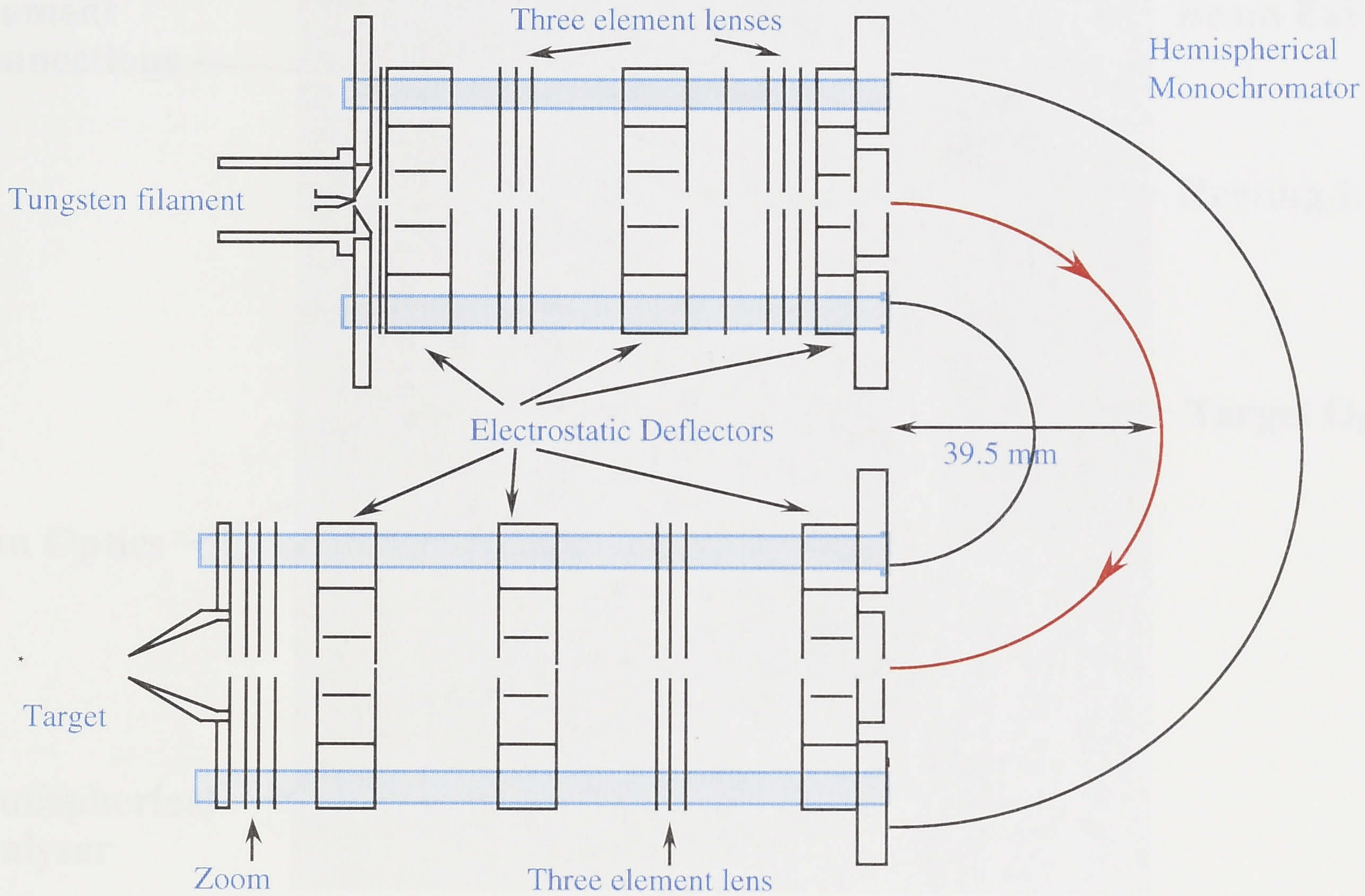

Figure 3.4: Schematic Diagram of Electron Optics

optics, which focus, collimate and set the final energy of the electron beam, and transport it to the interaction region.

A schematic diagram of the optics can be seen in figure 3.4. The extraction optics are designed to extract the emitted electrons from the thoriated tungsten filament and admit them to the entrance of the gun optics. Both the target and gun optics consist of a series of three-element aperture lenses and electrostatic deflectors. The lenses focus and collimate the electron beam and the deflectors aid in maintaining the correct direction of the beam inside the optics. The concentric hemispheres energy analyse the electrons, allowing a high resolution beam to be produced.

All the elements of the electron optics which are exposed to the electron beam are constructed from molybdenum, with the supporting structure constructed from non-

magnetic stainless steel. The various elements were electrically isolated from each other by the use of macor spacers.

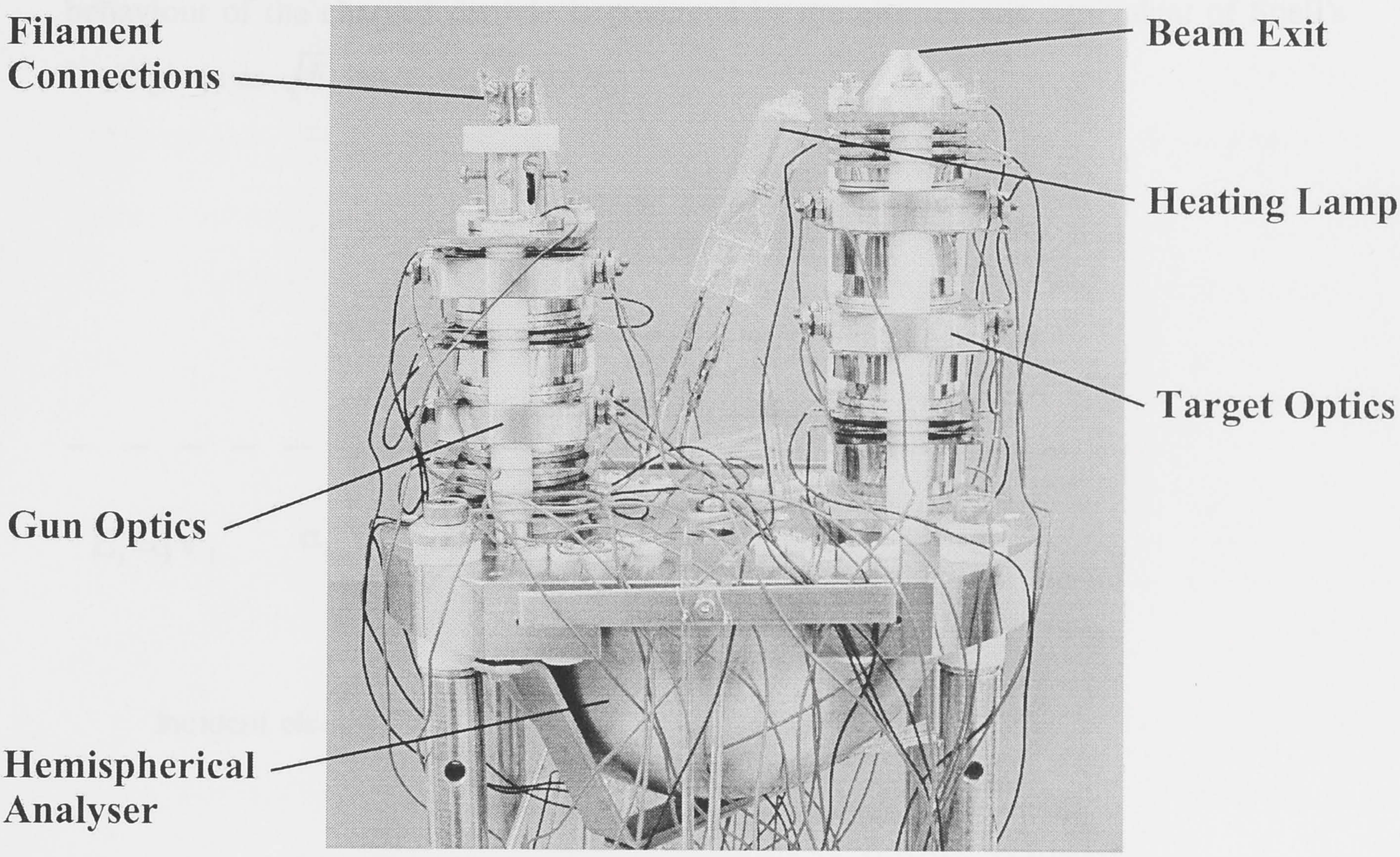

Figure 3.5: Photograph of electron spectrometer

During operation, the electron optics were kept at a temperature of approximately 120°C by two heating lamps to help avoid any metal deposition on the metal surfaces. Fields from the heating lamps had no major effect on the operation of the spectrometer. A photograph of the electron spectrometer is shown in figure 3.5.

Before discussing the separate components of the electron spectrometer, it is important to explain in some detail the operation of the electron lenses. The principles of the operation of electrostatic lenses can be found in numerous texts. In particular the books used to assist in the preparation of the following sections were "Building Scientific Apparatus" (Moore, Davis and Coplan, 1989), "Electron Optics" (Klemperer and Barnett, 1971), "Electrostatic Lenses" (Harting and Read, 1976) and "Electrostatic Lens Systems" (Heddle, 1991).

3.4.2 Principles of electron optics

It is well known that a charged particle experiences a change in velocity when passing through an electric field, as illustrated below in figure 3.6. In this case, the behaviour of the charged particle is governed by the electrostatic equivalent of Snell's Law, given as $\sqrt{E_1}\sin\alpha_1 = \sqrt{E_2}\sin\alpha_2$.

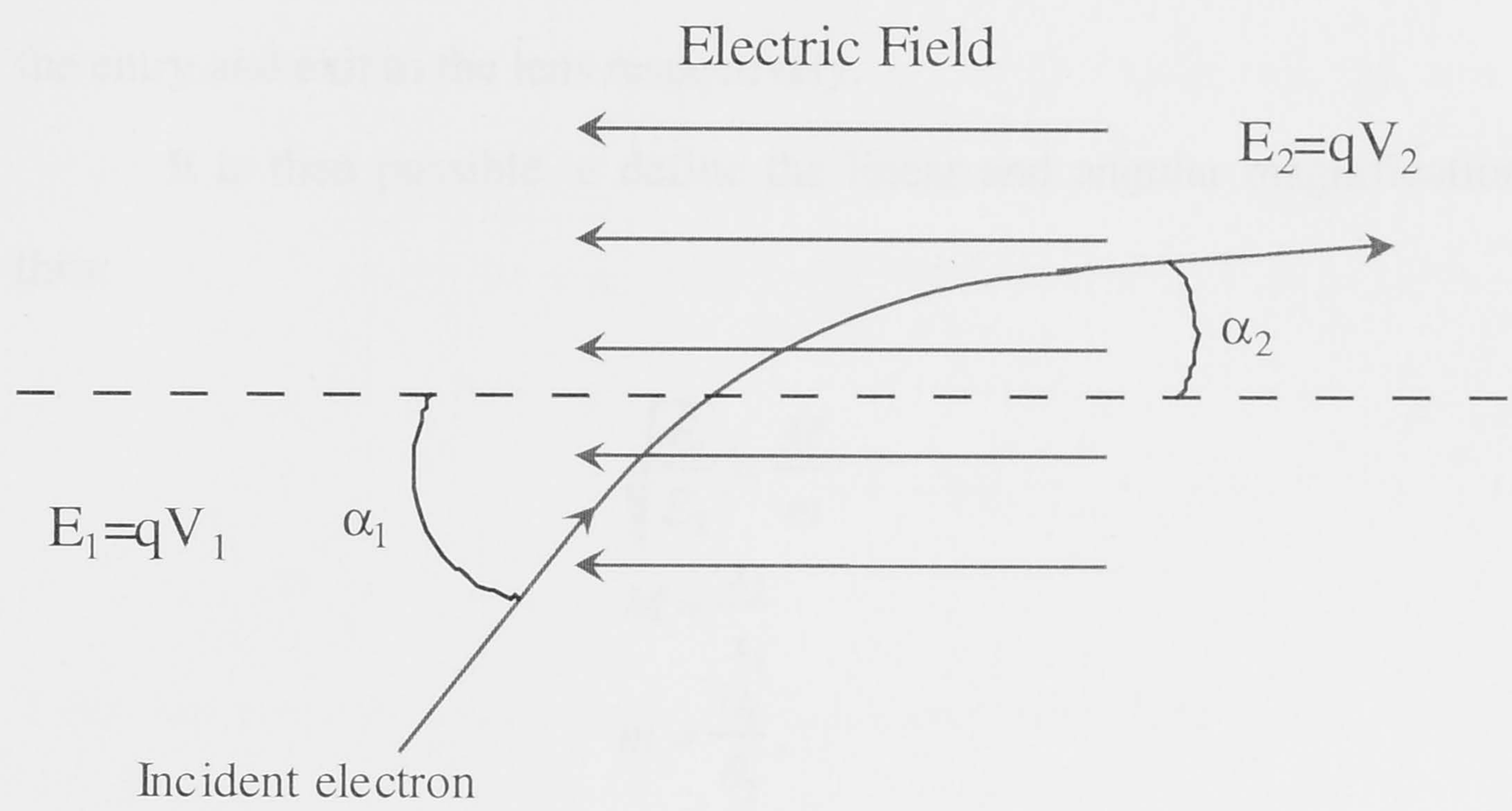

Figure 3.6: Electron in an electric field.

It is therefore easy to imagine that by a judicious arrangement of electric fields, it is possible to create a lens for charged particles, and more specifically electrons, similar to lenses used for the manipulation of light beams.

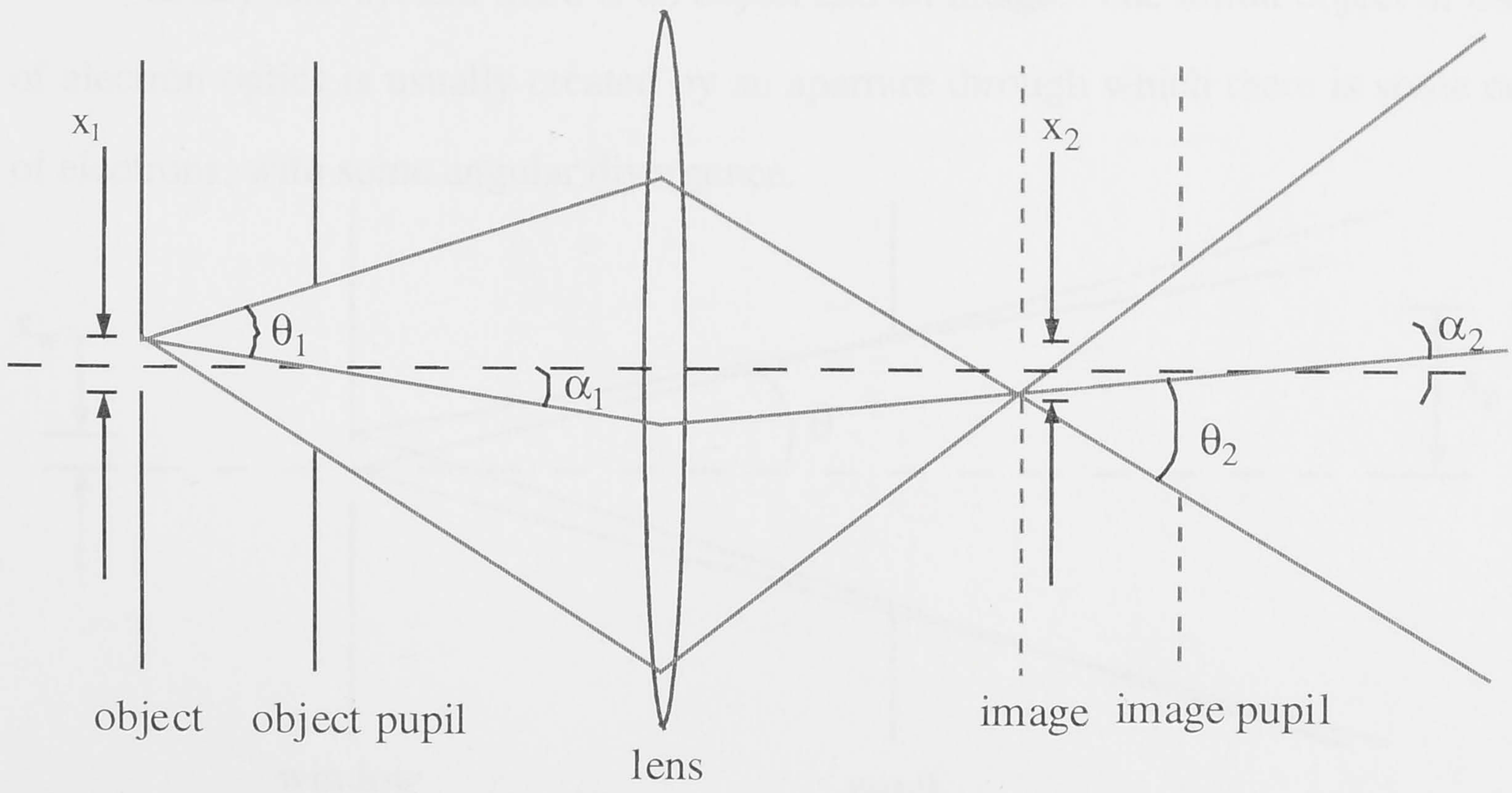

Figure 3.7: Typical object-image arrangement

A typical lens arrangement is shown in figure 3.7. In this case θ_1 is called the pencil angle and α_1 the beam angle. θ_2 and α_2 are the image pencil angle and image beam angle respectively. For most practical systems θ_1 and α_1 are small, so that $\sin\theta \sim \theta$. This is the Gaussian or paraxial approximation for optics. In Gaussian optics, the behaviour of the electron beam is governed (to first order) by the Helmholtz-Lagrange law, where $x_1\theta_1\sqrt{E_1} = x_2\theta_2\sqrt{E_2}$ with E_1 and E_2 the energies of the beam at the entry and exit to the lens respectively.

It is then possible to define the linear and angular magnifications of the beam thus:

$$\sqrt{\frac{E_1}{E_2}} = \frac{M}{m}$$

$$M = \frac{x_2}{x_1}$$

$$m = \frac{\theta_1}{\theta_2}, \qquad (3.1)$$

where M is the linear magnification and m is the angular magnification of the electron beam. If the current through the object pupil , I, is the same as the current through the image and the image pupil (as must be the case if the image and image pupil are virtual for instance) then we also have

$$\frac{I}{E_1\theta_1^2 x_1^2} = \frac{I}{E_2\theta_2^2 x_2^2}. \qquad (3.2)$$

In any lens system there is an object and an image. The initial object in the case of electron optics is usually created by an aperture through which there is some current of electrons, with some angular divergence.

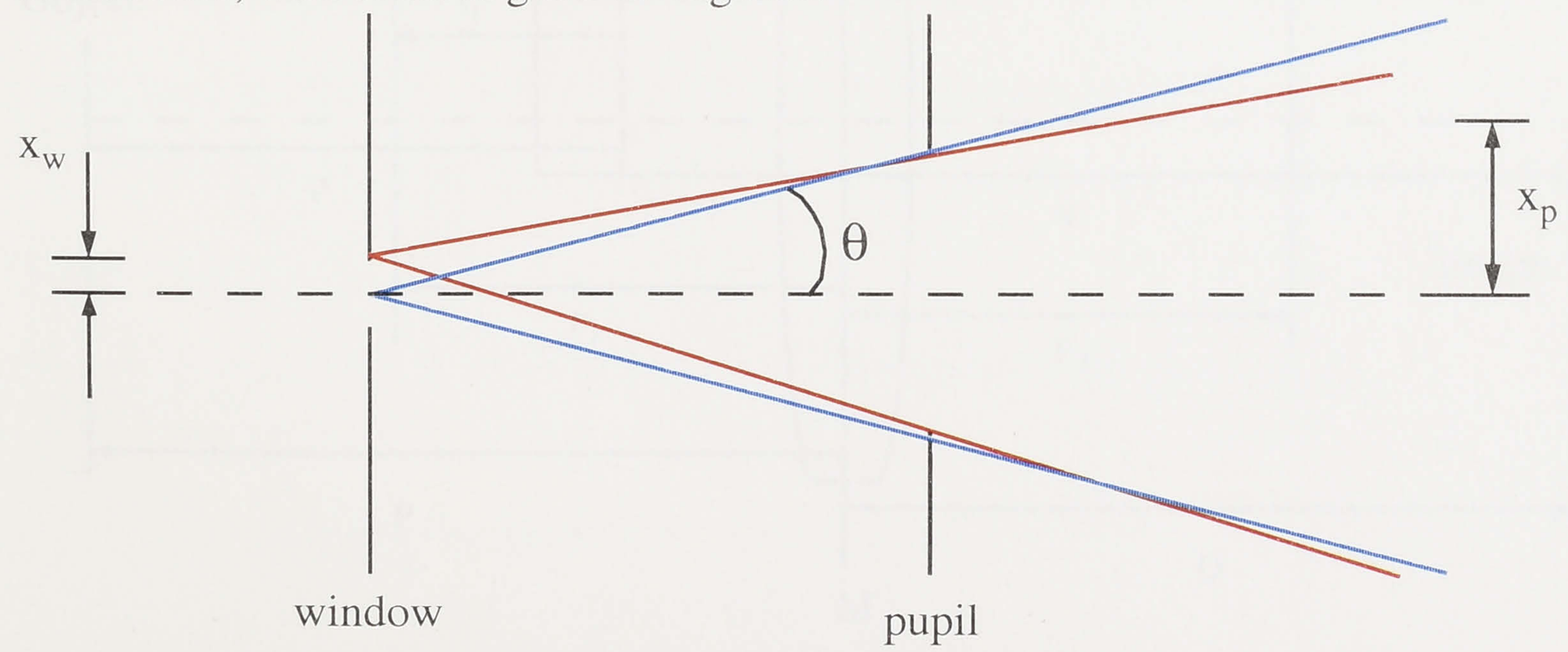

Figure 3.8: A typical window-pupil arrangement.

A straightforward way of creating an object is to use the window-pupil arrangement illustrated in figure 3.8. This shows a luminous window with the angular spread of the emerging beam limited by the pupil aperture. The brightness, β, of a point on the source (the window) at a given point (on the pupil) is

$$\beta = \frac{dI}{dA\,d\Omega}, \tag{3.3}$$

where dI is the current through the point on the source, dA is the area of the point on the source and $d\Omega$ is the solid angle defined by the point on the source. If there is cylindrical symmetry around the axis of the beam and the separation of the window and pupil is large enough, the integrated brightness at the pupil is seen to be

$$\beta = \frac{I}{\pi^2 x_w{}^2 \theta^2}. \tag{3.4}$$

From this, combined with equation 3.2, it then follows that

$$\frac{\beta_1}{E_1} = \frac{\beta_2}{E_2} \tag{3.5}$$

where β_1 is the brightness of the object pupil and β_2 is the brightness of the image pupil. It can then be seen that the ratio of brightness to energy is conserved in systems of this type.

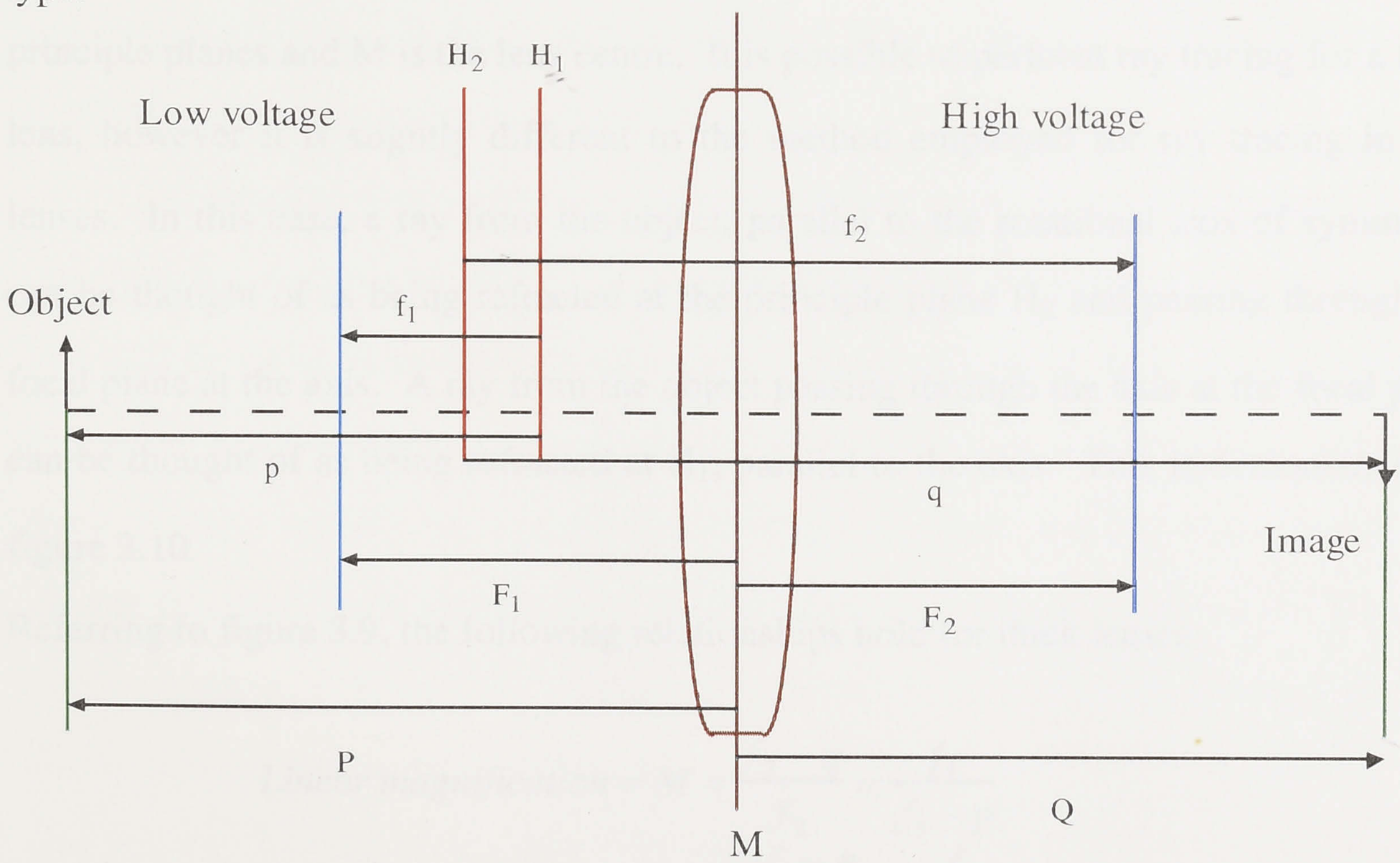

Figure 3.9: Schematic diagram of a thick lens.

Charged particle lenses can generally be approximated as thick lenses, due to the fact that the velocity of the particle changes continuously through the lens, rather than instantaneously as with conventional thin-lens photon optics. A general schematic of a thick lens is shown in figure 3.9.

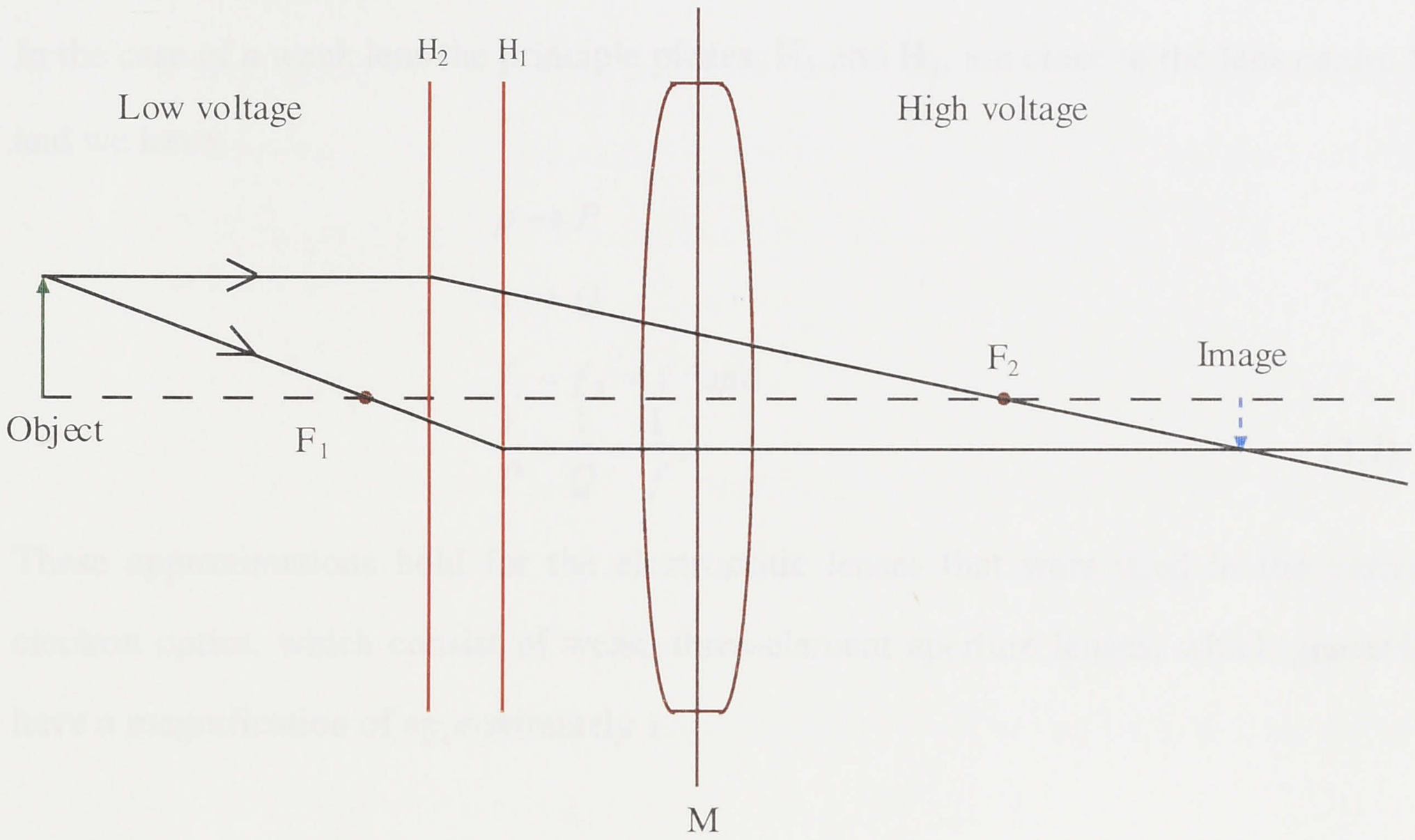

Figure 3.10: Ray tracing for thick lenses

The blue lines in figure 3.9 represent the focal planes, H_1 and H_2 are the principle planes and M is the lens centre. It is possible to perform ray tracing for a thick lens, however it is slightly different to the method employed for ray tracing in thin lenses. In this case, a ray from the object, parallel to the rotational axis of symmetry, can be thought of as being refracted at the principle plane H_2 and passing through the focal plane at the axis. A ray from the object passing through the axis at the focal plane can be thought of as being refracted at H_1, parallel to the axis. This is demonstrated in figure 3.10.

Referring to figure 3.9, the following relationships hold for thick lenses:

$$\textit{Linear magnification} = M = \frac{f_2 - q}{f_2} = \frac{f_1}{f_1 - p}$$

$$\textit{Angular magnification} = m = \frac{f_1 - p}{f_2} = \frac{f_1}{f_2 - q}$$

$$P = F_1 - \frac{f_1}{M}$$

$$Q = F_2 - Mf_2$$

$$(p - f_1)(q - f_2) = f_1 f_2$$

$$\frac{f_1}{p} + \frac{f_2}{q} = 1. \qquad (3.6)$$

In the case of a weak lens the principle planes, H_1 and H_2, are close to the lens centre M and we have

$$p \to P$$

$$q \to Q$$

$$f_1 \approx f_2 \approx f \quad \text{and}$$

$$\frac{1}{P} + \frac{1}{Q} = \frac{1}{f}. \qquad (3.7)$$

These approximations hold for the electrostatic lenses that were used in the current electron optics, which consist of weak, three-element aperture lenses, which generally have a magnification of approximately 1.

3.4.3 Aberrations

In general, electrostatic lenses suffer from aberrations which are analogous to those found in optical systems, with the addition of some other effects that are specific to this type of lens. In broad terms, there are three main sources of imperfections: geometric, chromatic and space charge effects.

Geometrical aberrations arise from deviations from the paraxial approximation, discussed in the previous section. Typically, aberrations are expressed in terms of Δr, the radial deviation from the ideal case. The most significant of these errors is spherical aberration which leads to the point object not appearing as a point image, but rather being blurred. In this case, rays passing close to the limits of the entrance pupil of the lens are focussed on the axis closer to the lens than the Gaussian focal point. This effect is demonstrated in figure 3.11. Instead of a point, the image appears as a round spot. The expression for Δr can be written as

$$\Delta r = -MC_s\alpha_0^3, \qquad (3.8)$$

where we have

$$C_s = C_{s0} + \frac{C_{s1}}{M} + \frac{C_{s2}}{M^2} + \frac{C_{s3}}{M^3} + \frac{C_{s4}}{M^4}. \qquad (3.9)$$

The expression for the axial displacement is then given by

$$\Delta l = -MC_s \frac{\alpha_0^3}{\alpha_i}. \qquad (3.10)$$

As can be seen in figure 3.11, there is a point before the Gaussian focus at which the bundle of rays has a minimum diameter, and this is known as "the disc of least confusion". It can be shown that the radius of this disc is given by

$$r_{disc} = \frac{-MC_s}{4} \alpha_0^3 \qquad (3.11)$$

(see Heddle, 1991 for instance) which, comparing with equation 3.8, means that it is 1/4 of the radius of the image at the Gaussian image plane. The disc of least confusion can be shown to be positioned at 3/4 of the distance from the image plane to the point at which the most severely distorted rays cross the axis (ie: those rays which pass through the object pupil at the widest point).

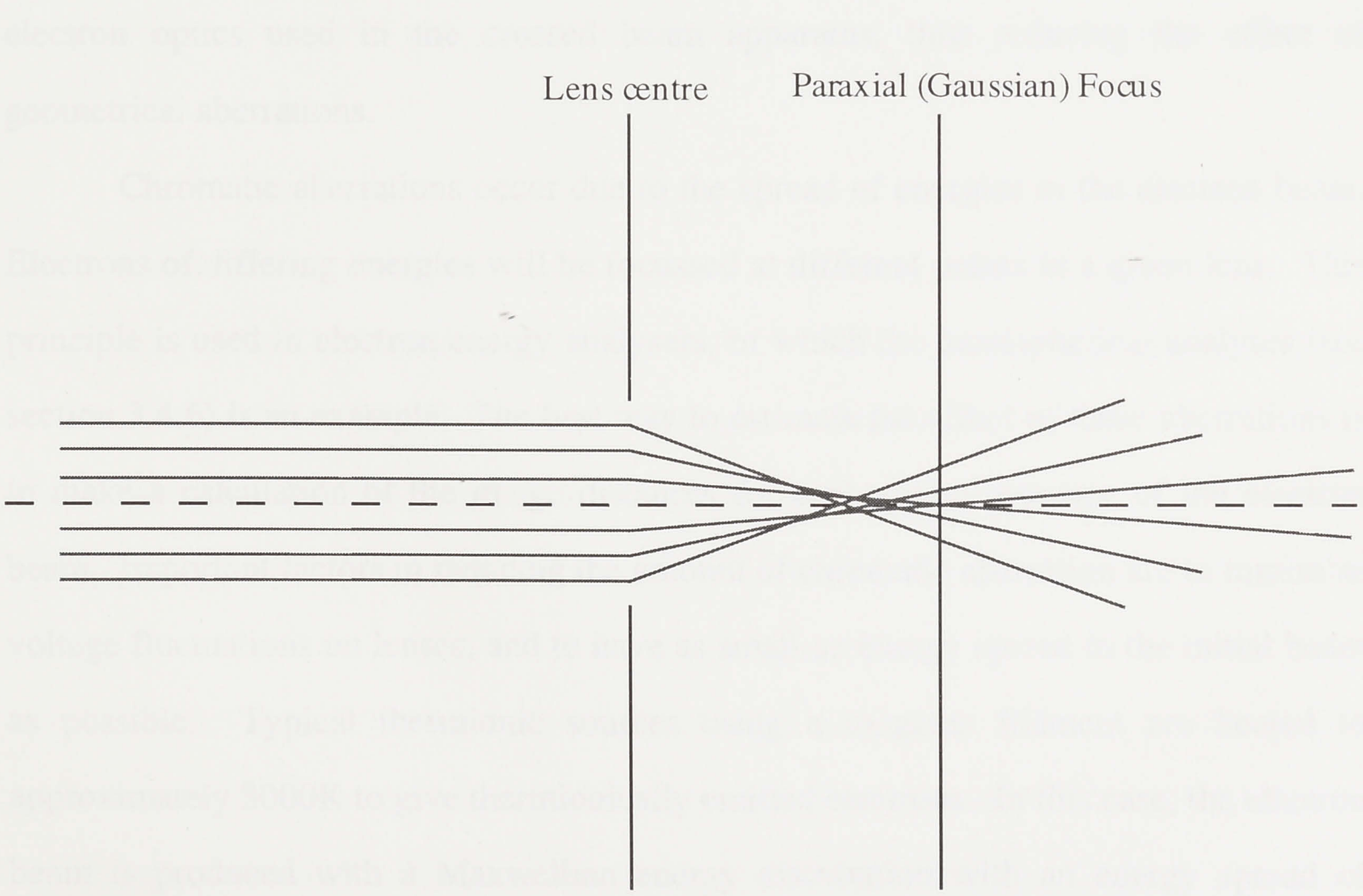

Figure 3.11: Spherical aberrations in an electrostatic lens
(Klemperer and Barnett, 1971)

Clearly, if the lens is operated so that the disc of least confusion is treated as the image, rather than the Gaussian image as might first be expected, the magnitude of the spherical aberrations can be reduced by a factor of 4. Another way of reducing spherical aberrations is to keep lens filling factors below 50% (Moore, Davis and Coplan 1989). The filling factor is defined as the ratio of the radius of the most extreme rays passing through the entrance aperture to the lens, to the radius of the lens aperture. This is easily understood when considering that the expression for Δr is proportional to α^3, thus by minimising the pencil angles the aberrations are dramatically reduced. Harting and Read (1971) have extensive tabulations of the values of C_{s0}, C_{s1}, C_{s2}, C_{s3} and C_{s4} for many types of electrostatic lenses operated at different voltages, enabling the aberrations to be calculated for the individual lenses concerned. Other geometrical aberrations include off-axis aberrations such as astigmatism, curvature of field and coma, but provided that the object is small compared to the lens diameter, the value of C_s provides a good measure of the overall geometrical aberration (Moore, Davis and Coplan 1989). These two conditions were maintained in the design of the electron optics used in the crossed beam apparatus, thus reducing the effect of geometrical aberrations.

Chromatic aberrations occur due to the spread of energies in the electron beam. Electrons of differing energies will be focussed at different points in a given lens. This principle is used in electron energy analysers, of which the hemispherical analyser (see section 3.4.6) is an example. The best way to estimate the effect of these aberrations is to make a calculation of the image distances for each energy extreme of the electron beam. Important factors in reducing the amount of chromatic aberration are to minimise voltage fluctuations on lenses, and to have as small an energy spread in the initial beam as possible. Typical thermionic sources using a tungsten filament are heated to approximately 3000K to give thermionically emitted electrons. In this case, the electron beam is produced with a Maxwellian energy distribution with an energy spread of approximately 500 meV. In the spectrometer used in the present apparatus, the source of electrons is a thoriated tungsten filament heated to approximately 2200K by passing a current of approximately 1.6A through the wire. The ability to produce electrons at this

lower temperature gives a more favourable energy spread of around 350 meV, thus reducing chromatic aberrations. There is also anecdotal evidence that sources using thoriated tungsten filaments are brighter than those with conventional tungsten filaments.

Electron-electron repulsion is also an important consideration in electron beams, giving rise to the space charge effect. This limits the amount of current that is able to pass through any given region of space, and also leads to larger divergences than those calculated from geometrical considerations. For instance, the maximum current density possible at the anode in an electron lens system is given by

$$I_{max} = 2.34\ V^{3/2}/d^2 \quad (\mu A cm^{-2}) \tag{3.12}$$

(Moore, Davis and Coplan 1989). Space charge effects can lead to a change in the focussing properties of an electron lens, as well as blurring the image, as the electrons are not able to be focussed to a point due to their mutual repulsion. In the present lens system, with the exception of the initial extraction optics and the first three-element lens, the electron current densities are well below the space charge limit, and errors due to space charge effects will be minimal compared to those due to geometric and chromatic aberrations.

3.4.4 Extraction optics

A schematic representation of the extraction optics is shown in figure 3.12. A current of approximately 1.6A is passed through the thoriated tungsten hairpin filament, heating it to approximately 2200°C. At this temperature, the filament emits electrons with an energy spread of approximately 350 meV, and a large angular divergence.

The purpose of the extraction optics is to take the thermionically emitted electrons form the thoriated tungsten filament and admit them to the gun optics of the electron monochromator. To do this, a three element system featuring a Pierce extraction stage (Pierce, 1949) is used, which is shown in figure 3.12.

The extraction system consists of a surface inclined at an angle of 67.5° to the beam axis (the Pierce element) which provides an homogenous focussing field in the region of the cathode. An additional tuning element (the grid element) is located

between the Pierce element and the anode, which is the entry into the first lens of the electron optics. Analytical modelling of this system using the SIMION design package

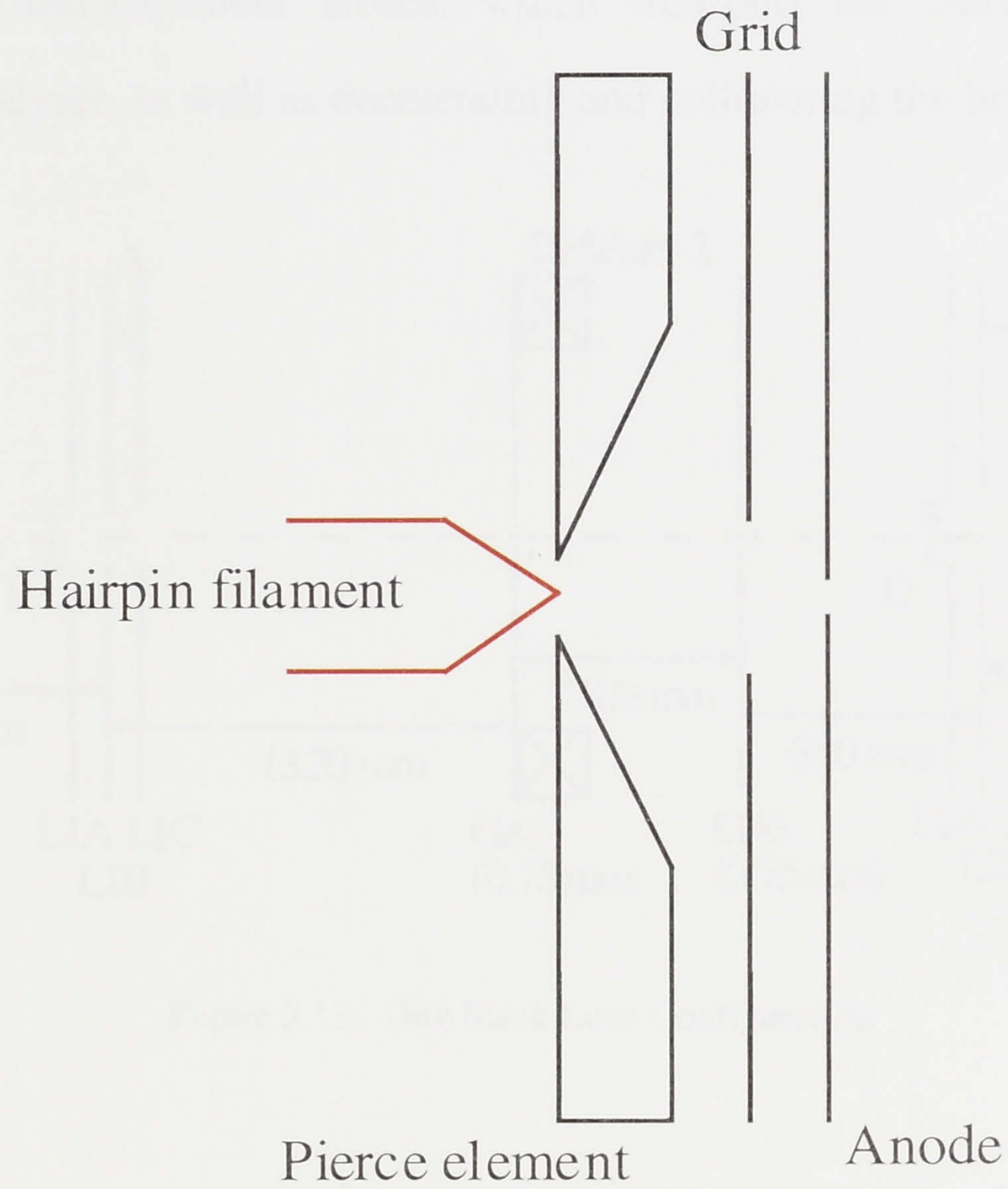

Figure 3.12: Schematic digram of Pierce extraction system

(PC/PS2 version 4.0, D. A. Dahl and J. E. Delmore, Idaho Engineering Laboratories) has shown that the optimum configuration for this type of arrangement is to have the tip of the hairpin filament protruding slightly through the Pierce aperture (Gulley 1994). The design of the extraction optics was such that the potential of the anode at the entry to the gun optics was +60V. From equation 3.12, considering that the spacing between the Pierce aperture and the anode is 4 mm and the anode aperture has a diameter of 1 mm, it can be seen that this leads to a maximum current of 13.3 μA that can be transmitted through the anode. Typical values for the potentials of the extraction optics are +4V for the Pierce element and +20V for the grid element, with the anode at +60V. The first two voltages are empirically determined, by adjusting them to the values that give the optimum current and energy resolution from the monochromator, and they may vary over time and whenever a new filament is used.

3.4.5 Gun optics

The gun electron optics is shown schematically in figure 3.13. This set of optics consists of two three-element lenses, which transport the electron beam to the hemispherical analyser, as well as decelerating and collimating the beam. There are

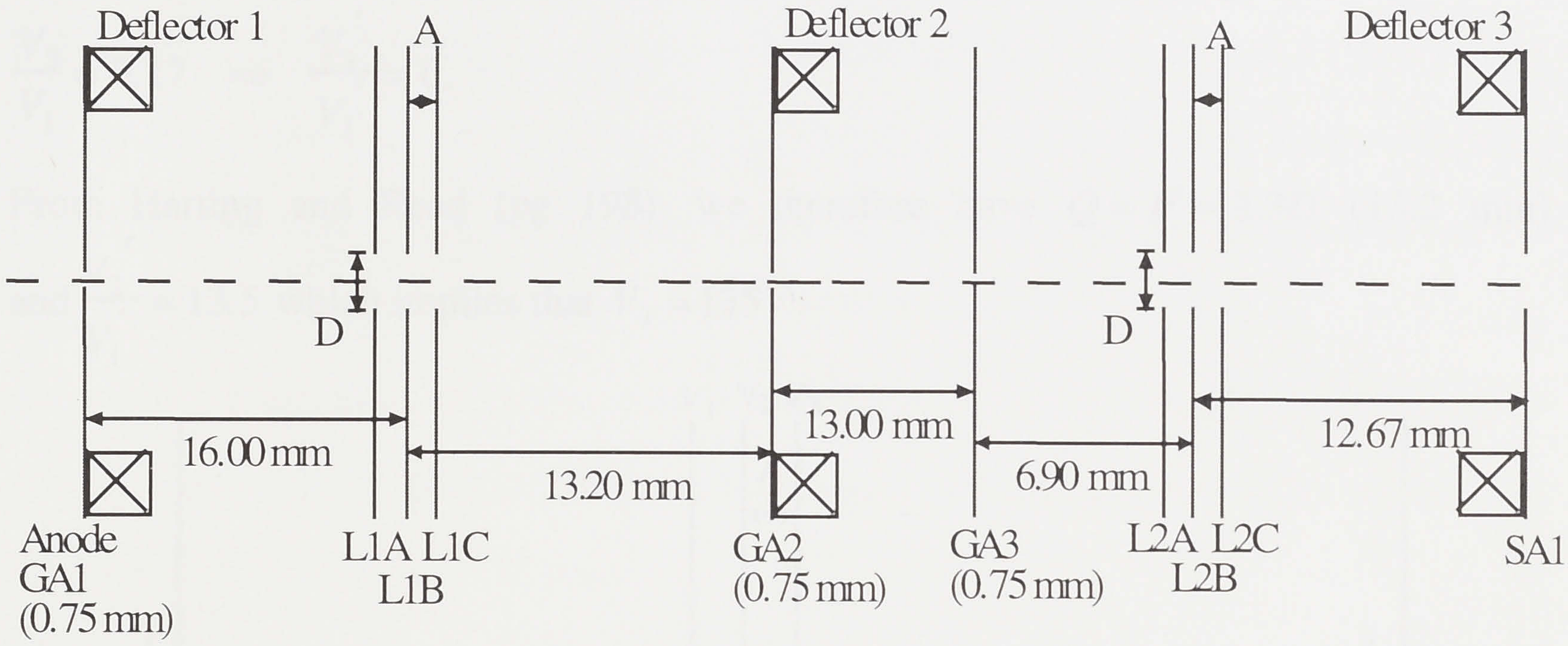

Figure 3.13: Gun Stack Lens Configuration

also 3 sets of electrostatic deflectors which play no direct role in the focussing of the beam, but allow the beam direction to be fine-tuned. As the potential of the anode element is 60V and the potential at the entrance to the hemispherical analyser (SA1) was typically taken to be 2V for design purposes, both lenses were designed to be decelerating lenses. Two lenses are required as it is difficult to decelerate the beam so dramatically (a factor of 30) with only one lens, without introducing significant aberrations into the lens system. It is important to have a minimum of aberrations at the entrance to the hemispheres as this is perhaps the most critical region in the electron optics. Separating this set of optics into the two lenses, it is then possible to examine its operation in some detail.

The first lens was designed to decelerate the electrons from 60 eV to 10 eV, and a diagram of this lens, lens 1, is shown in figure 3.14 below, omitting the deflectors. To obtain the operating parameters of this lens, the tables and diagrams of "Electrostatic Lenses", by Harting and Read (1976), were used. The parameters in this reference are only for accelerating lenses, so in this case we have to look at the "time reversed" lens

to obtain the appropriate operating voltages. Using a dash to designate the parameters of the virtual accelerating lens, in the case of lens 1 we then have:

$P \equiv Q'$ $\quad V_1 \equiv V_3'$ $\quad M = 1 \Rightarrow M' = 1$

$Q \equiv P'$ $\quad V_2 \equiv V_2'$ $\quad P = Q' = 4.0D$

$V_3 \equiv V_1'$ $\quad D = 4.0\ mm$ $\quad \frac{A}{D} = 0.5$ and

$\frac{V_3}{V_1} = 0.17 \Rightarrow \frac{V_3'}{V_1'} = 6.$

From Harting and Read (pg 198), we therefore have $Q = P' \approx 3.3D$ (13.2 mm) and $\frac{V_2'}{V_1'} \approx 13.5$ which implies that $V_2 \approx 135V$.

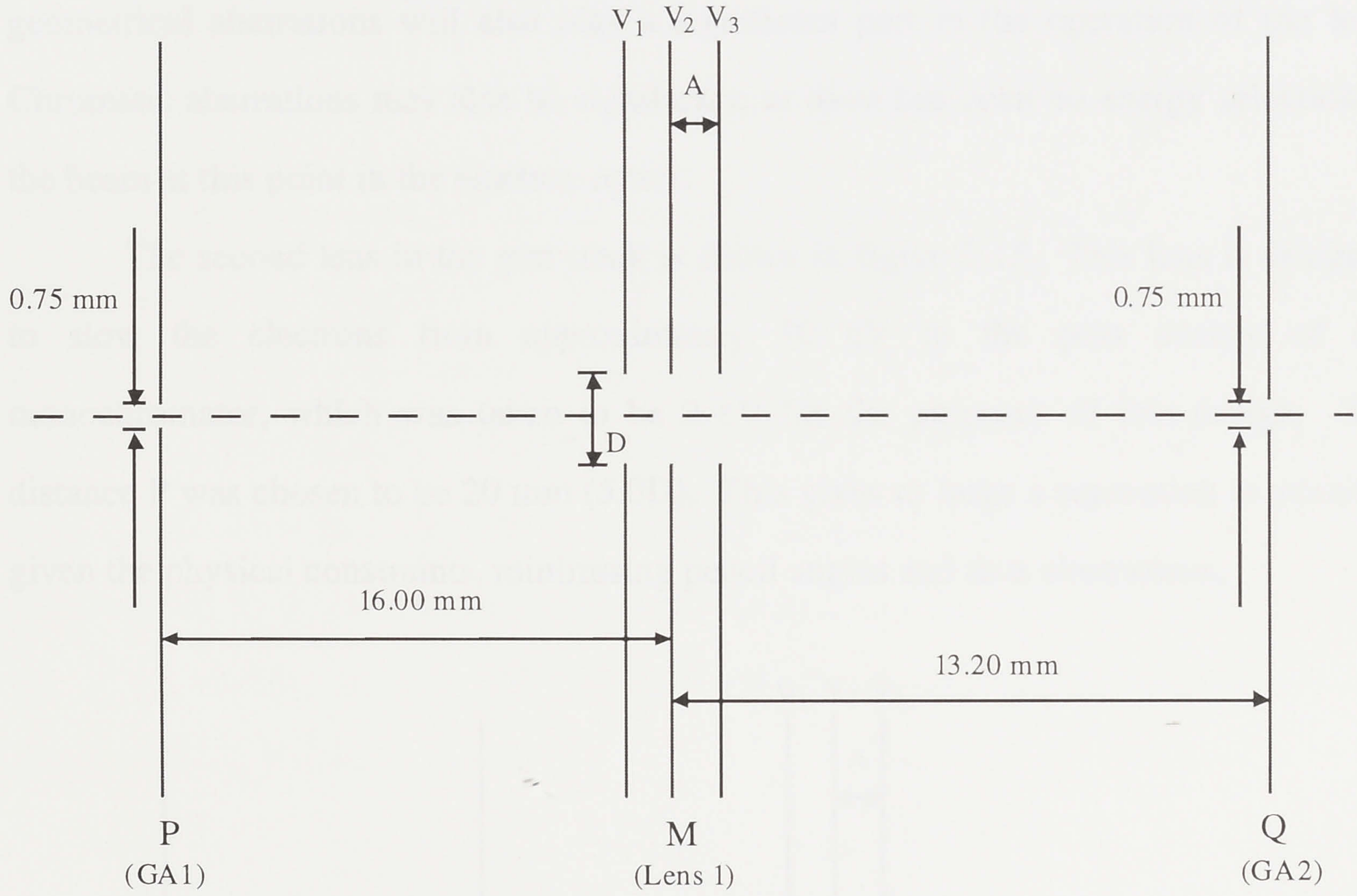

Figure 3.14: Schematic Diagram of Lens 1

It should be noted that P was chosen arbitrarily to be 4.0D (16 mm), the distance being dictated by the constraints of the physical size of the apparatus. Another point worth noting is that while the voltage ratios and values above are for an idealised situation there will be variations, individual to the electron optics, depending on such factors as the accuracy of the spacing of the lens elements. In operation, the above values can be used only as a guide to the "correct" settings, and will have to be varied in conjunction with the other elements in the electron monochromator to obtain the best

electron beam. This is, of course, true for all the lenses and other elements making up the electron monochromator.

Aberrations are likely to be at their largest in this lens for several reasons. The first is that the current density at the aperture GA1 is large, in principle with the transmitted current approaching the limit of 13.3 μA derived in section 3.4.3. This will lead to the possibility of space charge effects changing the focal properties of the lens, and possibly some broadening of the energy distribution. For instance, the beam spread from GA1 will be quite large due to these effects, implying that the filling factor for this lens will be quite high, over the recommended 50% given in section 3.4.3. As a result, geometrical aberrations will also play a significant part in the operation of the lens. Chromatic aberrations may also be significant, as there has been no energy selection in the beam at this point in the electron optics.

The second lens in the gun stack is shown in figure 3.15. This lens is designed to slow the electrons from approximately 10 eV to the pass energy of the monochromator, which was taken to be 2 eV for the purposes of this design. The distance P was chosen to be 20 mm (5.0D). This gives as large a separation as possible given the physical constraints, minimising pencil angles and thus aberrations.

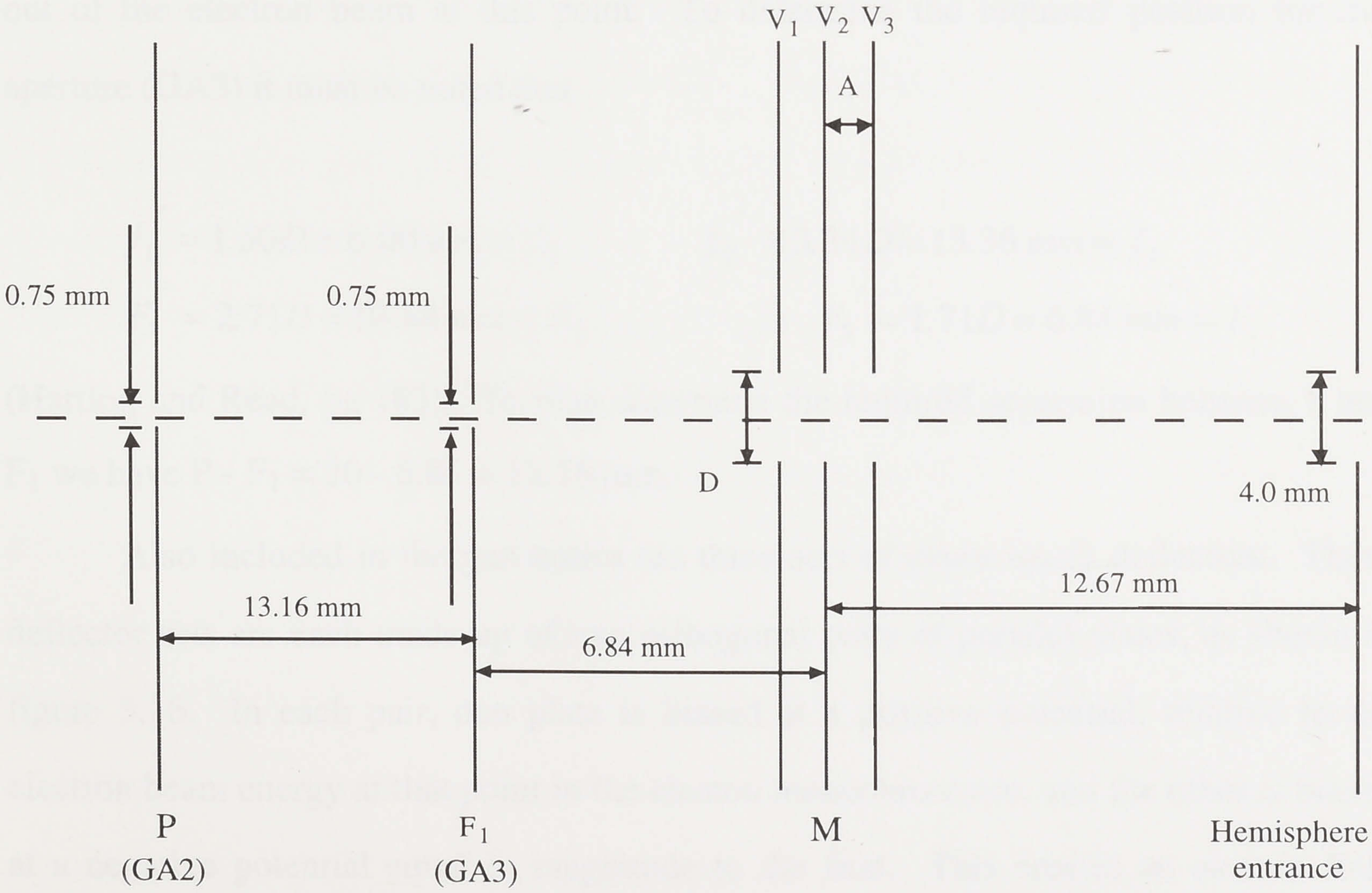

Figure 3.15: Schematic Diagram of Lens Stack 2

Again, remembering that the time reversed situation must be considered in determining the appropriate operating parameters for this lens, and applying a similar method to that used for lens 1, we then have

$$V_1 \equiv V_3' \qquad M = 1 \quad \Rightarrow \quad M' = 1$$

$$V_2 \equiv V_2' \qquad P = Q' = 5.0D$$

$$V_3 \equiv V_1' \qquad D = 4.0\ mm \qquad \frac{A}{D} = 0.5 \quad \text{and}$$

$$\frac{V_3}{V_1} = 0.2 \quad \Rightarrow \quad \frac{V_3'}{V_1'} = 5.0\,.$$

Consulting Harting and Read once more (pg 197) we find $P' = Q \approx 4.1D$ or 16.4 mm and $\frac{V_2'}{V_1'} \approx 9.0$ giving $V_2 \approx 18V$. It was decided to include an aperture in this lens at F_1, so that off-axis electrons will be rejected and the electron beam will be focussed to infinity (i.e. with no angular divergence) at the entrance of the hemispherical analyser. It is clear how this will occur by referring to figure 3.10 where it can be seen that any electrons originating at F_1 will travel parallel to the lens axis after passing through the lens. This also has the effect of greatly reducing aberrations in the electron spectrometer, as those electrons which fall outside the paraxial approximation are taken out of the electron beam at this point. To determine the required position for this aperture (GA3) it must be noted that

$$f_1' = 1.50D = 6.00\ mm = f_2 \qquad f_2' = 3.34D = 13.36\ mm = f_1$$

$$F_1' = 2.71D = 10.84\ mm = F_2 \qquad F_2' = 1.71D = 6.84\ mm = F_1$$

(Harting and Read, pg 183). To then determine the required separation between P and F_1 we have P - F_1 = 20 - 6.84 = 13.16 mm.

Also included in the gun optics are three sets of electrostatic deflectors. These deflector sets are each made up of two orthogonal pairs of parallel plates, as shown in figure 3.16. In each pair, one plate is biased at a positive potential, relative to the electron beam energy at that point in the electon monochromator, and the other is biased at a negative potential equal in magnitude to the first. This creates an electric field between each pair of plates which is capable of deflecting the electron beam, with the

amount of deflection depending on the off-axial position of the electrons. Thus, by adjusting the potential difference between the plates, the direction of the electron beam can be fine tuned and the current to the hemispherical analyser can be maximised.

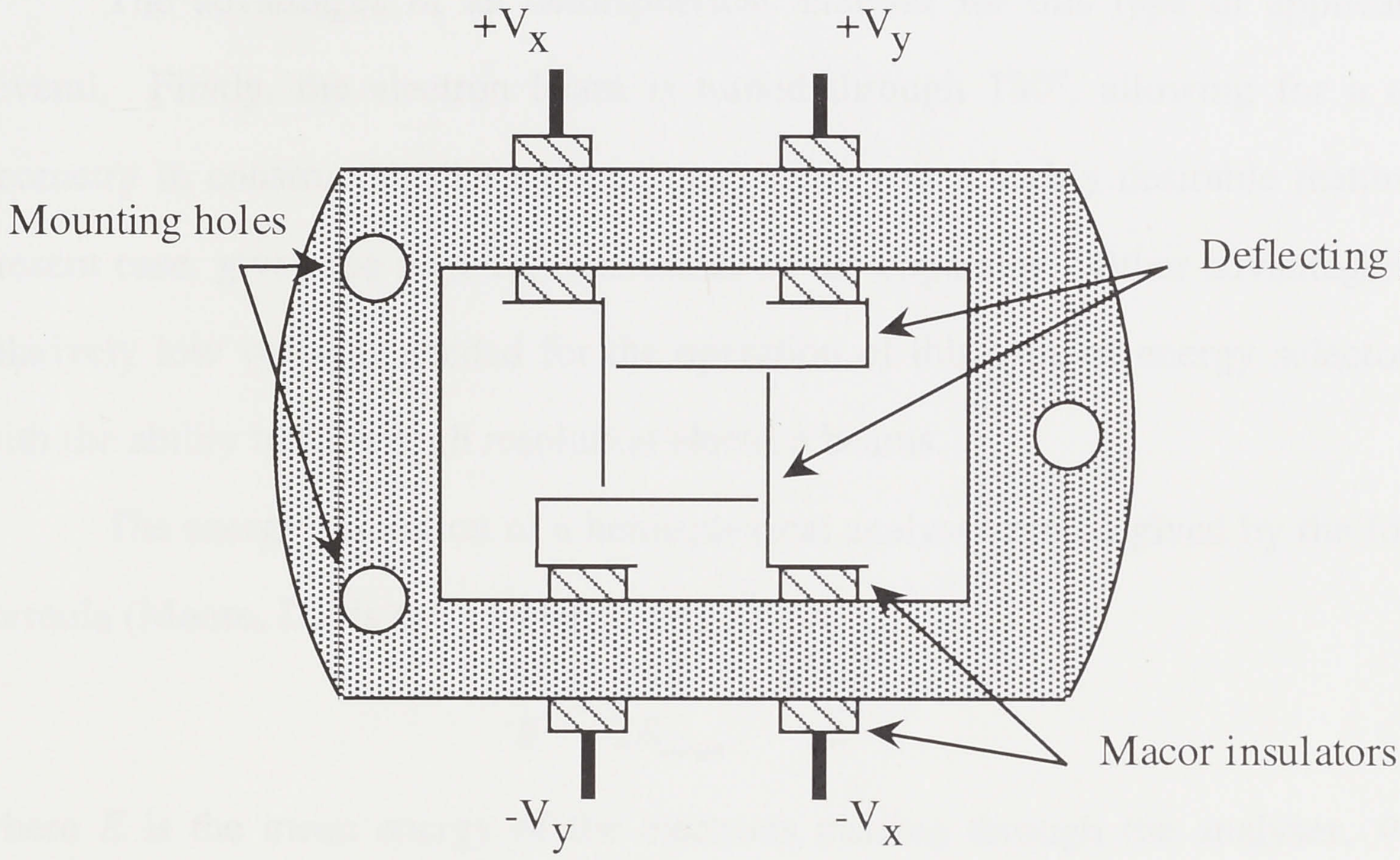

Figure 3.16: Schematic diagram of an electrostatic deflector

3.4.6 Hemispherical energy analyser

From the gun optics, the collimated electrons pass into the hemispherical energy analyser. This is a dispersive energy analyser, which focuses only those electrons of a certain energy (the pass energy) from the entrance to the exit of the hemispheres. It consists of two concentric hemispheres manufactured from molybdenum. The inner hemisphere has a radius of 27.5 mm and the outer hemisphere has a radius of 51.5 mm, giving a mean radius (R_{mean}) of 39.5 mm. Each hemisphere is kept at the appropriate potential to produce an electric field varying as the inverse square of the radius. This condition allows electrons of the desired energy to be refocussed at the exit of the hemispherical analyser, whilst electrons of other energies are dispersed across the exit plane. Given the mean radius and the desired mean potential (V_{mean}) the field at any other radius, r, is then given by

$$V_r = V_{mean}\left(\frac{2R_{mean}}{r} - 1\right). \qquad (3.13)$$

Thus by setting the potentials of the inner and outer hemispheres to the appropriate values, we can ensure the inverse square nature of the field between the two hemispheres.

The advantages of an hemispherical analyser for this type of application are several. Firstly, the electron beam is turned through 180^{o}, allowing for a compact geometry in constructing the electron gun. This was a highly desirable feature in the present case, given the physical constraints of the apparatus. Other advantages are the relatively low voltages needed for the operation of this type of energy selector, along with the ability to form high resolution electron beams.

The energy resolution of a hemispherical analyser can be given by the following formula (Moore, Davis and Coplan 1989):

$$\frac{\Delta E}{E} = \frac{\omega}{2R_{mean}} + \frac{(\Delta\alpha)^2}{2} \qquad (3.14)$$

where E is the mean energy of the electrons passing through the analyser, ω is the spatial size of the beam and $\Delta\alpha$ is the angular divergence of the electron beam at the entrance to the analyser. Clearly, to obtain the best possible resolution, it is desirable to keep the angular divergence and spot size of the beam to a minimum at the entrance to the monochromator, as well as to keep the mean analysing energy as low as possible. It is also important that the electric field at the entrance and exit plane of the hemispherical analyser maintains its inverse square behaviour, to minimise any fringing effects on the electrons in this region. Due to the fact that the three-element plate optics (cylindrical symmetry) used here have a fundamentally different symmetry to the hemispherical analyser (spherical symmetry), this is not a trivial concern. To achieve the field correction, a set of concentric hoops lie in the entrance and exit plane, consisting of 6 stainless steel rings, with radii of 32, 34.75, 41.5, 44.25 and 47 mm. The correct voltage, at each radius, to maintain an inverse square field is easily calculated from equation 3.13, and the individual hoops, illustrated in figure 3.17, are then set to this voltage. In this way, deviations from the ideal conditions are minimised, reducing aberrations in this part of the monochromator. The analyser was typically operated with a pass energy of 1.2V, which is somewhat lower than the value taken for the design of

the monochromator. This has a minimal effect on the overall operation of the optics, as long as the critical lens voltage ratios are maintained. The electron optics design was

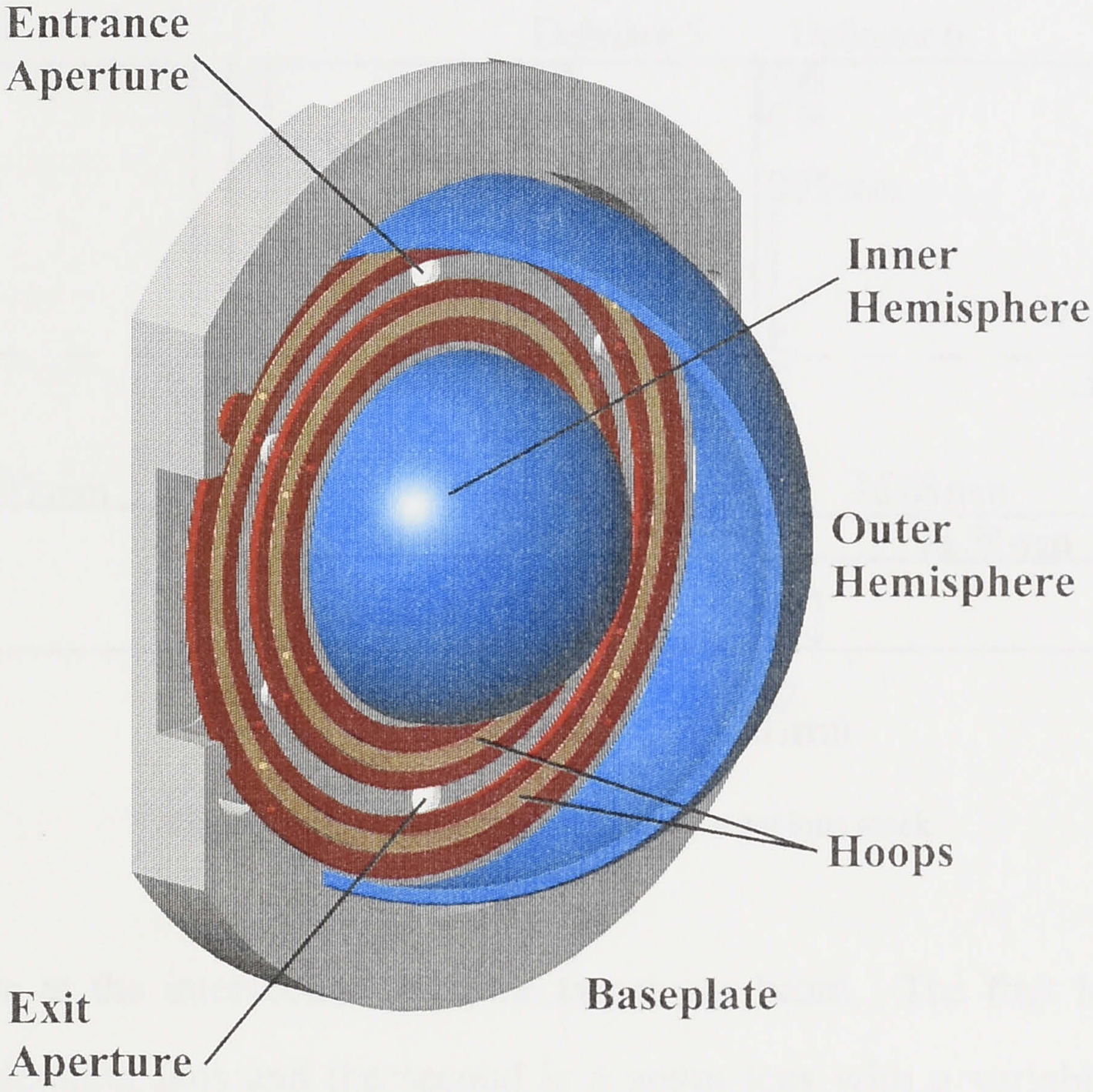

Figure 3.17: Diagram of hemispherical energy analyser and field correcting hoops

also such that the angular divergence of the electron beam at the entrance to the hemispheres should be close to zero degrees. Using equation 3.14, these values give a theoretical resolution of approximately 12 meV. Of course, as this value is the minimum attainable, in practice the resolution of the electron beam can be expected to be worse than this value, and it was in fact measured to be typically 35 meV (see chapter 4). Whilst the reasons for this are not fully understood, it is no doubt due to deviations from the ideal conditions that the optics design is based on, such as a non zero divergence at the entrance to the hemispheres, and slight deviations from the ideal conditions in the manufacture of the optics.

3.4.7 Target optics

The target optics consists of two three-element aperture lenses and three sets of deflectors. The first lens was designed to accelerate the electron beam emerging from

the hemispherical analyser to an intermediate energy of 10 eV. From there the second lens sets the electron beam to the appropriate energy whilst maintaining the focus of the

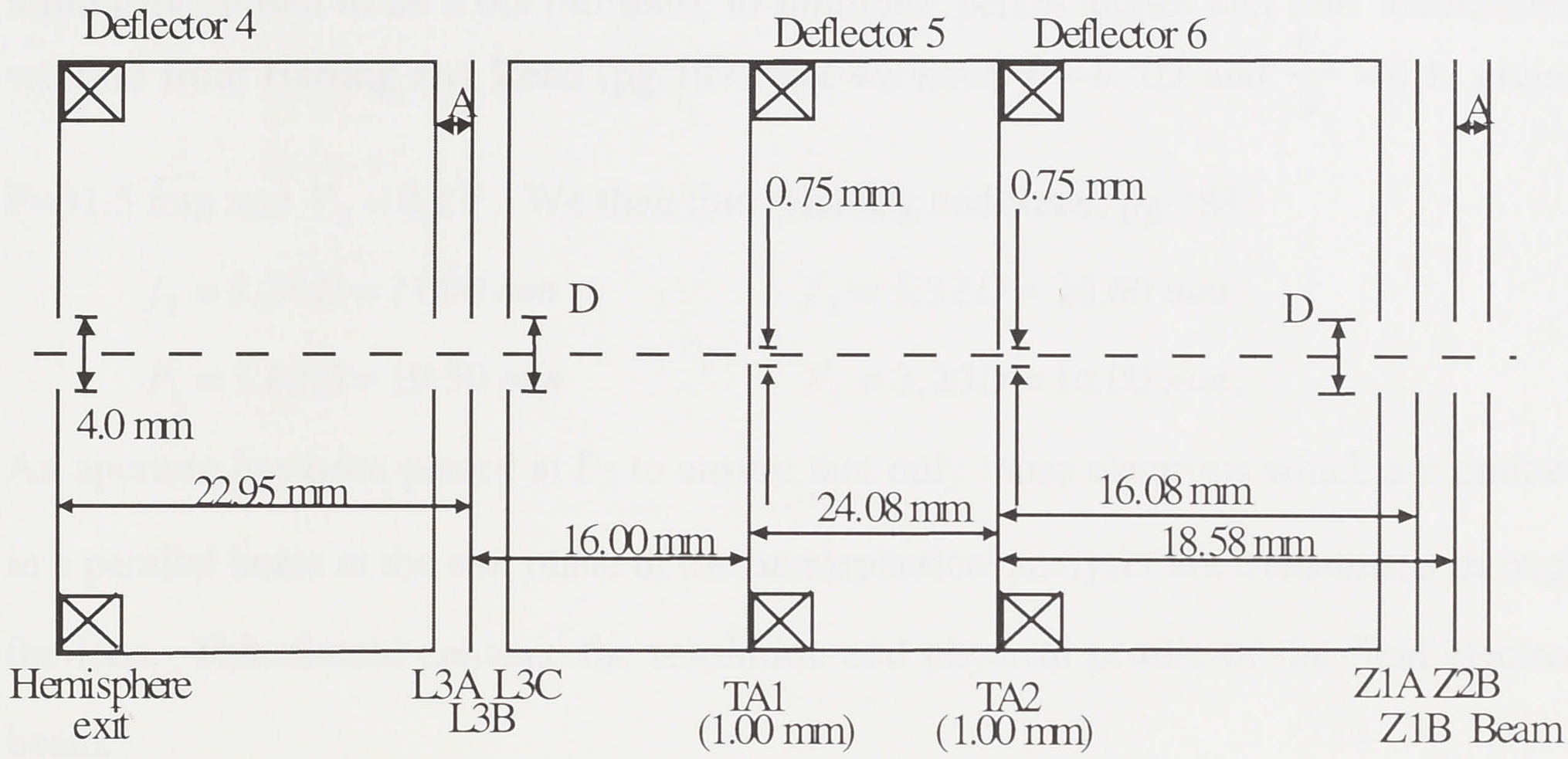

Figure 3.18: Schematic diagram of target lens stack

electron beam at the intersection with the target gas beam. The first lens is a three element accelerating lens and the second is a zoom lens with a variable lens centre, which allows a fixed focal point to be maintained for the electron beam over a variety of energies. A diagram of the lens arrangement is shown in figure 3.18 above.

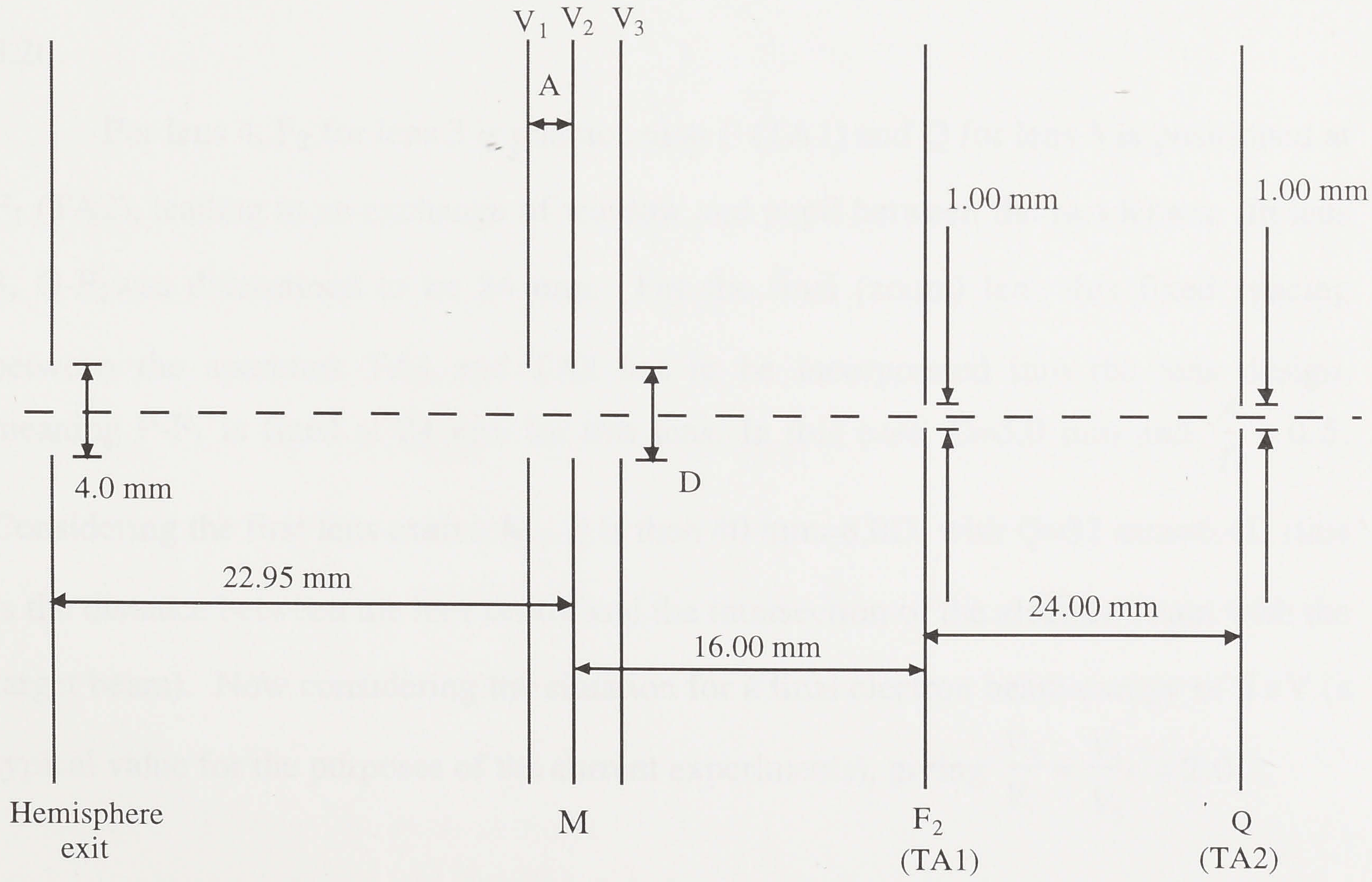

Figure 3.19: Schematic diagram of lens 3

Dealing with the first lens in this stack, lens 3 as shown in figure 3.19, we have $V_1 = 2V$ and $V_3 = 10V$, giving $\frac{V_3}{V_1} = 5.0$. With M=1, D=5.0 mm, $\frac{A}{D} = 0.5$ and Q arbitrarily chosen to be 8.0D (40 mm), to minimise pencil angles and thus aberrations, we find from Harting and Read (pg 197) that we have $P \approx 6.3D$ and $\frac{V_2}{V_1} \approx 4.1$, giving P=31.5 mm and $V_2 \approx 8.2V$. We then find (Harting and Read, pg 183)

$$f_1 = 2.38D = 11.90\ mm \qquad f_2 = 5.32D = 26.60\ mm$$

$$F_1 = 3.89D = 19.50\ mm \qquad F_2 = 3.20D = 16.00\ mm\,.$$

An aperture has been placed at F_2 to ensure that only those electrons which are emitted in a parallel beam at the exit plane of the hemispherical analyser are transmitted through the lens. This should enhance the resolution and physical profile of the final electron beam.

The final lens in the electron monochromator is a zoom lens with a moveable lens centre (Read 1983). This is incorporated into the design as it is important that the electron beam has the same profile at its intersection with the target gas beam over the range of energies examined. This minimises any spurious effects that can be associated with a different interaction volume, such as a change in the solid angle viewed by the various detectors. With this in mind, lens 4 was designed as shown below in figure 3.20.

For lens 4, F_2 for lens 3 is positioned at P (TA1) and Q for lens 3 is positioned at F_1 (TA2), leading to an exchange of window and pupil between the two lenses. In lens 3, Q-$F_2$was determined to be 24 mm. For the final (zoom) lens this fixed spacing between the apertures TA1 and TA2 has to be incorporated into the lens design, meaning P-F_1 is fixed at 24 mm for this lens. In this case, D=5.0 mm and $\frac{A}{D} = 0.5$. Considering the first lens centre, M_1, P is then 40 mm=8.0D, with Q=32 mm=6.4D (this is the distance between the lens centre and the intersection of the electron beam with the target beam). Now considering the situation for a final electron beam energy of 5 eV (a typical value for the purposes of the current experiments), giving $\frac{V_3}{V_1} = \frac{V_1'}{V_3'} = 2.0$.

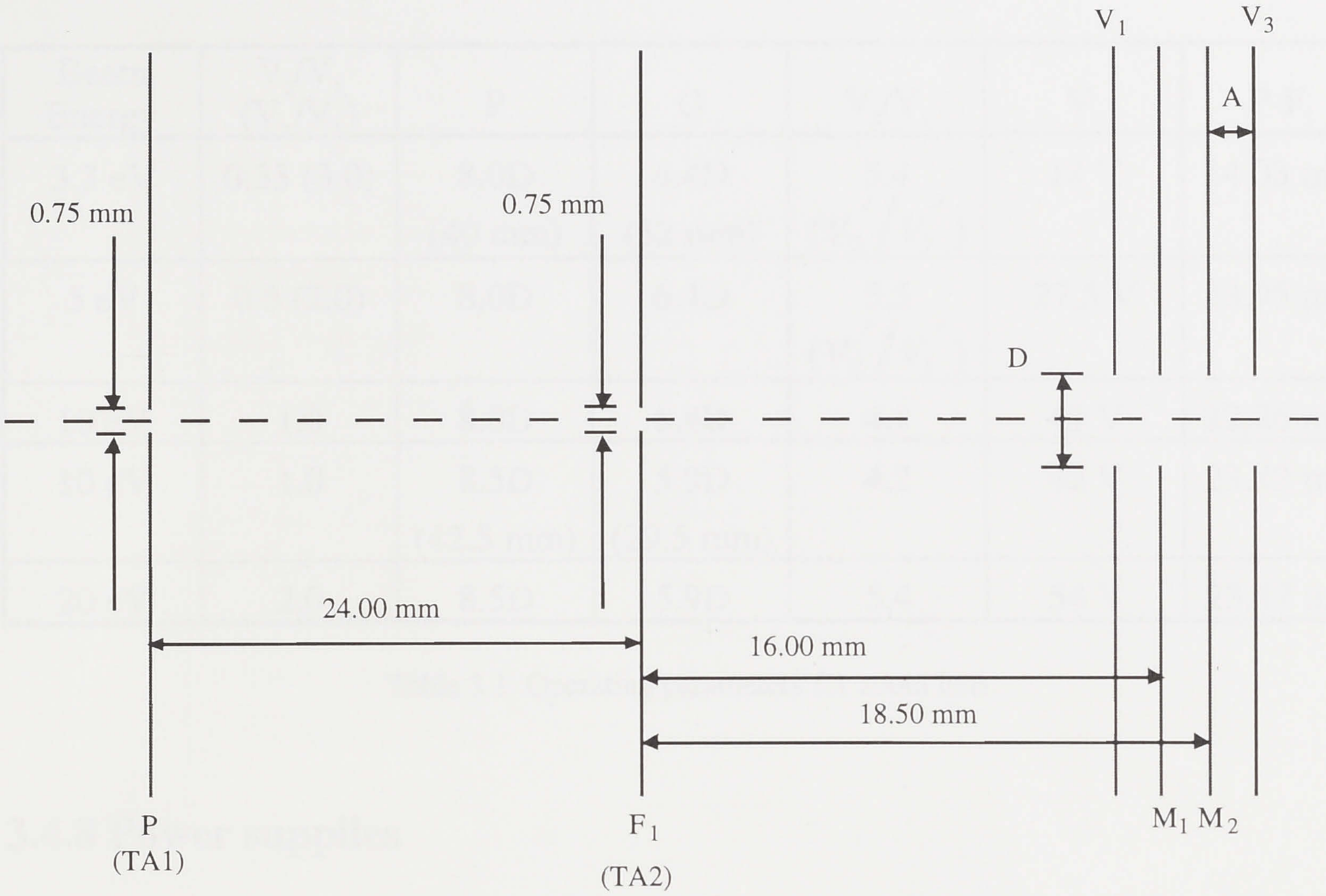

Figure 3.20: Schematic diagram of lens 4 (zoom lens)

From Harting and Read (pg 193) it can be seen that $\frac{V_2'}{V_1'} = \frac{V_2}{V_3} \approx 5.5$ and $M' \approx 1.2$, giving $V_2 \approx 27.5\,\mathrm{V}$ and $M \approx 0.83$, and also

$$f_1 = 4.23D = 21.15\,mm \qquad f_2 = 2.99D = 14.95\,mm$$

$$F_1 = 3.21D = 16.05\,mm \qquad F_2 = 3.85D = 19.25\,mm.$$

This then gives P-F_1=23.95 mm, which is acceptably close to the fixed value of 24 mm determined previously by lens 3. To consider the operation of the lens at various energies within the desired range for the experiment, the same process can be followed as outlined above. The parameters for each lens centre position at each energy can be calculated, and the ideal conditions for the operation of the spectrometer can be determined. The results of this investigation are summarised in table 3.1.

It can be seen from this table that by changing V_2 as the beam energy increases, the focus of the lens can be maintained at the target region as desired. In addition to this, by changing the lens centre from M_1 to M_2 for energies of 10 eV or greater, the operation of the lens can be maintained so that P-F_1 stays close to the fixed value of 24 mm, thus reducing aberrations that may occur with the change in this separation from the ideal conditions.

Beam Energy	V_3/V_1, (V_3'/V_1')	P	Q	V_2/V_1	V_2	P-F_1
3.3 eV	0.33 (3.0)	8.0D (40 mm)	6.4D (32 mm)	5.4 (V_2'/V_1')	18 V	24.03 mm
5 eV	0.5 (2.0)	8.0D	6.4D	5.5 (V_2'/V_1')	27.5 V	23.95 mm
10 eV	1.0	8.0D	6.4D	4.1	41 V	22.26 mm
10 eV	1.0	8.5D (42.5 mm)	5.9D (29.5 mm)	4.2	42 V	23.82 mm
20 eV	2.0	8.5D	5.9D	5.4	54 V	23.47 mm

Table 3.1: Operating parameters for zoom lens.

3.4.8 Power supplies

The power supplies to provide the appropriate voltages for each element of the electron monochromator were purpose-designed and built to the required specifications. It is important for electron optics applications that power supplies have low noise and good stability characteristics. This allows aberrations to be minimised, and the energy resolution of the electron beam to be kept as high as possible. With this in mind, the design required electronic ripple and other electronic noise kept below 5mV to keep any deleterious effects upon the operation of the monochromator to a minimum. The extraction optics required four power supplies, consisting of a 3A/3V current supply for the thoriated tungsten filament, a 0 - ±1V supply to provide the bias (contact potential) for the filament, a 0 - ±5V supply for the Pierce element and a 0 - +100V for the grid potential. For the three-element electron lenses, several 0 - +300V and 0 - +30V ground-referenced power supplies were constructed, all with low current and low noise characteristics, to minimise any effects that electronic noise may have on the electron beam. The electrostatic deflectors used 0 - ±25V supplies, that were able to be biased at the appropriate lens potential, depending upon the location of the deflectors. The hemispherical analyser power supplies were built into one unit, consisting of a single 0 - +15V independently adjustable supply which, via a system of low resistance voltage dividers, provided the voltages for the hemispheres and the correcting hoops. In this way, the master supply could be changed and all of the hemisphere-related voltages

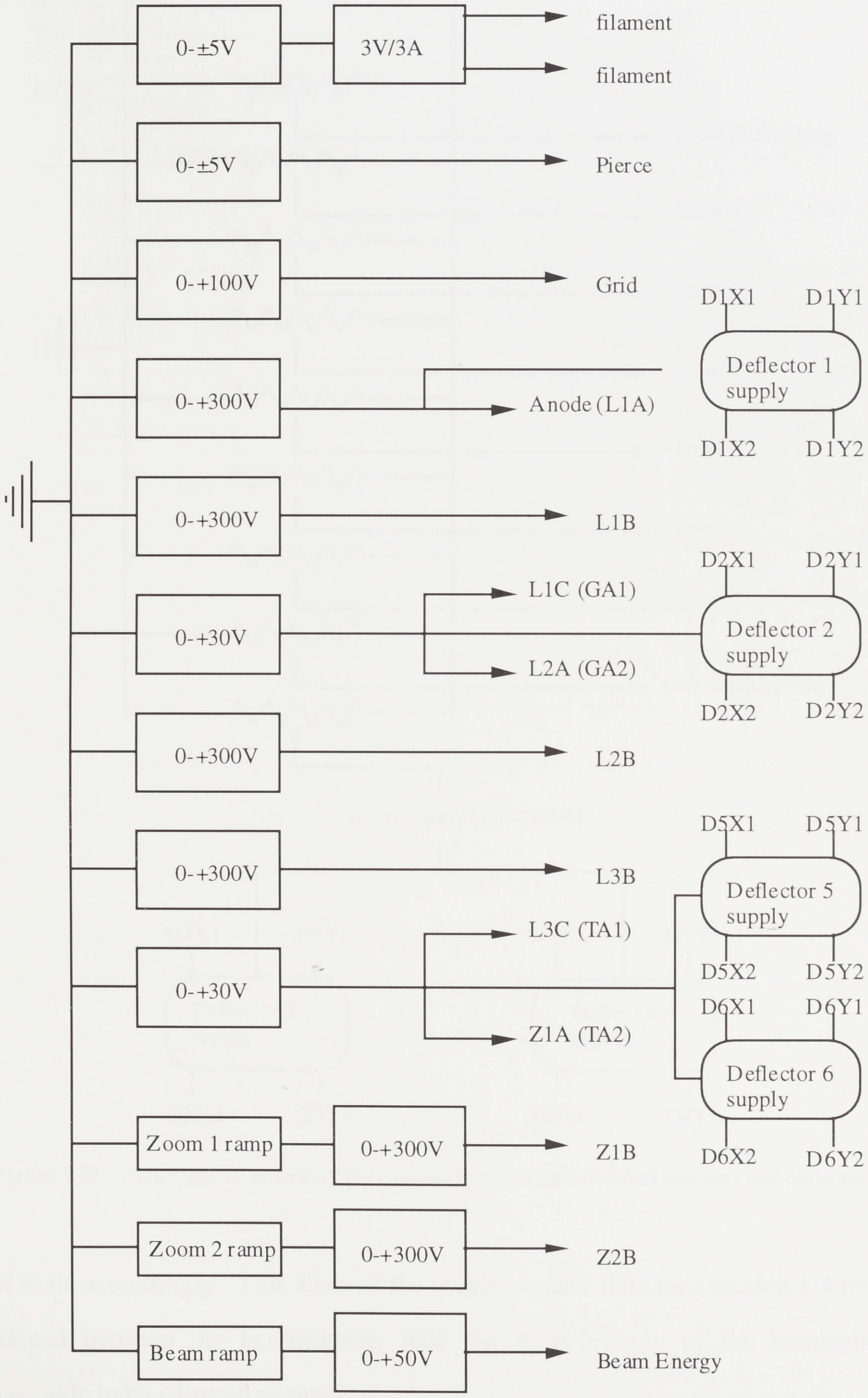

Figure 3.21: Schematic diagram of power supply connections to electron lens elements and deflectors

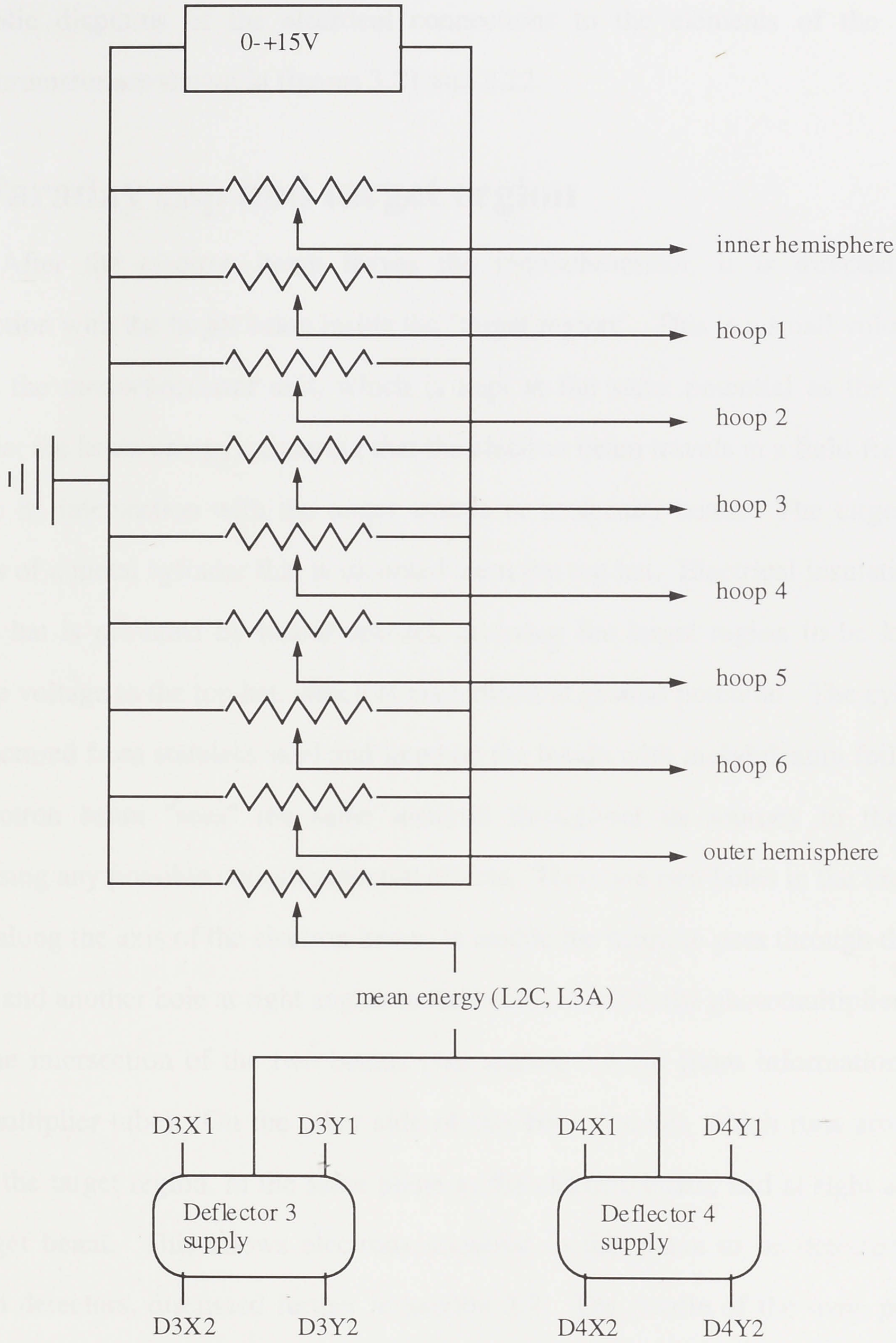

Figure 3.22: . Schematic of power supply connections for hemispherical analyser and deflectors

would scale accordingly. This allowed the inverse square field (see section 3.4.6) to be maintained between the hemispheres, with the mean energy of the hemispherical analyser able to be adjusted as required.

All the supplies were built in standard 19 inch, rack-mountable boxes allowing the power supplies to all be located together in a compact and moveable unit.

Schematic diagrams of the electrical connections to the elements of the electron monochromator are shown in figures 3.21 and 3.22.

3.5 Faraday cup and target region

After the electron beam leaves the monochromator, it is directed to the intersection with the target beam inside the "target region". This is a small volume, just outside the monochromator exit, which is kept at the same potential as the electron beam (ie: the beam energy), ensuring that the electron beam travels in a field-free region prior to its intersection with the target atomic or molecular beam. The target region consists of a metal cylinder that is mounted from the top hat. Electrical insulation from the top hat is provided by macor spacers, allowing the target region to be kept at a separate voltage to the top hat, which is maintained at ground potential. The cylinder is manufactured from stainless steel and lined on the inside with molybdenum foil, so that the electron beam "sees" the same material throughout its journey to the target, minimising any possible contact potential effects. There are two holes in the interaction region along the axis of the electron beam, to enable the beam to pass through the target region, and another hole at right angles to the beam, to allow the photomultiplier tube to view the intersection of the two beams (see section 3.8 for more information on the photomultiplier tube). On the other side of this hole is a slit, which runs around one side of the target region, in the same plane as the electron beam, and at right angles to the target beam. This allows electrons scattered in this plane to be detected by the electron detectors, discussed further in section 3.7. The needle of the oven protrudes into the target region, terminating 2 mm below the electron beam, and is also kept at beam potential so as not to affect the passage of the electron beam.

After passing through the target region, the electron beam is collected by a Faraday cup. The cup consists of a 27 mm long cylinder, with a diameter of 6 mm, which is maintained at the beam potential. A central element inside this cylinder is kept at +27 V (with respect to ground) and is conical in shape to minimise backscattering of the electron beam. A picoammeter (Keithley model 485) is connected in series with the power supply (a battery pack) for the central element, allowing the current through the

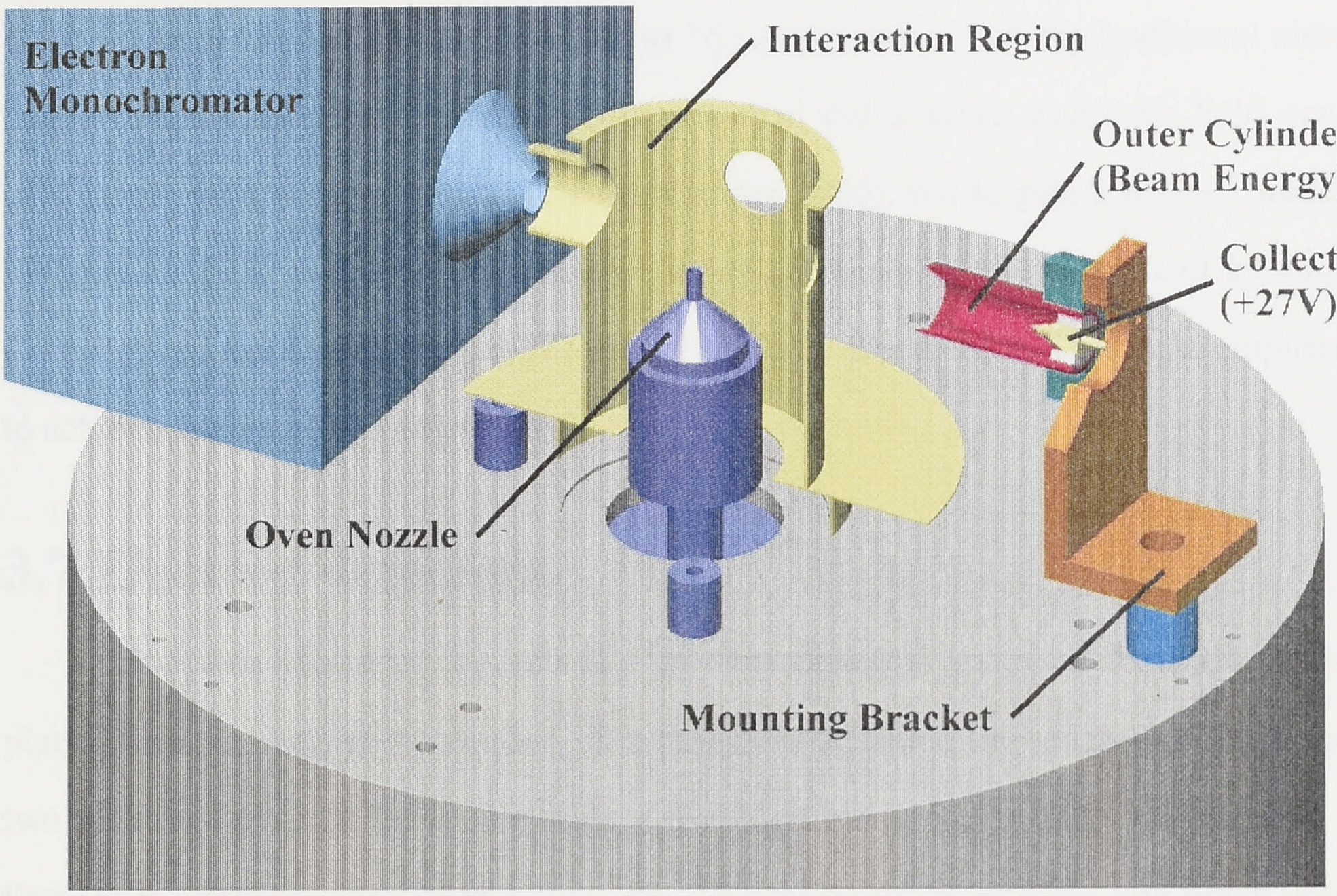

Figure 3.22: Diagram of target region and Faraday cup

interaction region to be measured and also allowing the beam to be maximised whilst adjusting the elements of the electron optics. Typically an electron current of 1 nA was obtained and used in the scattering experiments. A schematic diagram of the target region and Faraday cup is shown in figure 3.22.

3.6 Stray magnetic fields

It is well known that charges moving in a magnetic field experience a force perpendicular to the direction of their motion. In the case of low energy electrons, the force experienced as they move through the Earth's magnetic field can be enough to cause a significant deviation in their path. For instance, a 1 eV electron in the Earth's magnetic field (~0.45 Gauss) will travel in a circle of radius approximately 7.5 cm. As a result, it is important to compensate for the Earth's field in some way whilst performing the present experiments. This is done by using 3 pairs of mutually orthogonal Helmholtz coils. Each pair of coils is used to cancel the Earth's magnetic field in one direction, allowing a field free region to be established in their mutual centre, thus preventing the electron beam from experiencing any deviating force due to magnetic fields in its journey to the target. In this experiment, in order to simplify

construction, the coils were constructed to be square, rather than the traditional circular coils. In principle, the current needed to cancel out a given magnetic field can be calculated using an appropriate formula (Firester 1966), but in practice it is simpler to measure the field in the centre of the coils using a magnetometer (Schonstedt Instrument Company, model DM 2220, 0.1 mG sensitivity) and adjust the coil currents empirically to achieve the desired low field level.

3.7 Electron detectors

Scattered electrons are detected by two detectors mounted from the rotating platform in the scattering chamber. Electrons are admitted into each detector through two parallel, vertical slits 0.8 mm wide, 4 mm high and approximately 9 mm apart. The first slit is approximately 20 mm from the intersection of the electron and target beams. This gives an angular resolution of approximately $\pm 2^{o}$ in the scattering plane. The advantage of a slit aperture, as opposed to the more conventional circular apertue, is that electrons are able to be detected over a wider range of azimuthal angles, increasing the count rates in the experiment and hence reducing the counting time for the experiments.

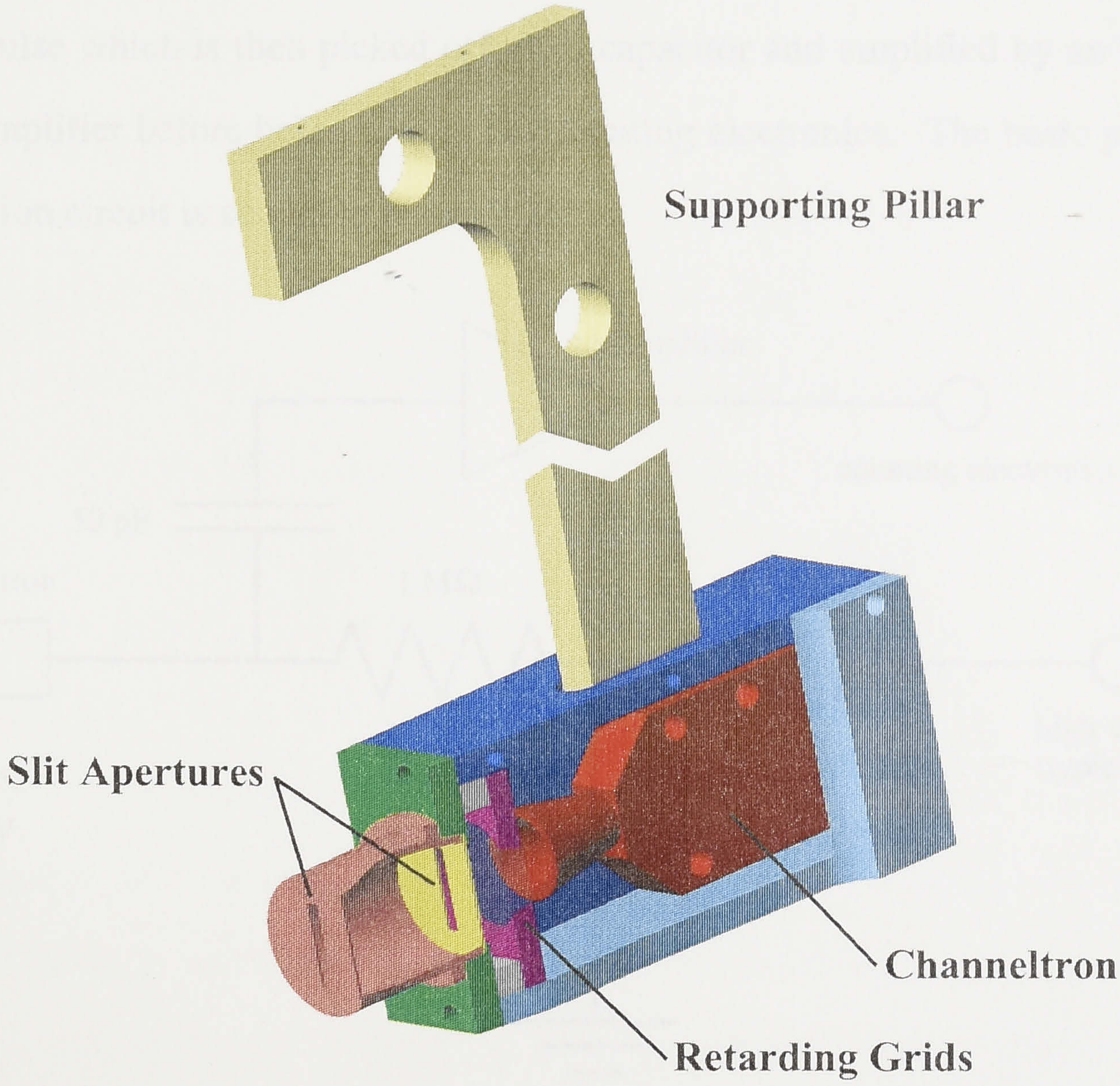

Figure 3.23: Schematic diagram of electron detector

The detectors each have a double retarding grid mounted in front of a channel electron multiplier, or channeltron (Dr. Sjuts model KBL5RS), and the total arrangement is housed in a small metal box (19x13x38 mm) which is mounted from the rotating platform via a stainless steel post. A detector and its mount are shown schematically in figure 3.23.

The retarding grid allows the selection of only those electrons which have been scattered elastically (i.e. without losing any energy) from the target. A voltage that is slightly above 0 V will admit only elastically scattered electrons, inelastically scattered electrons can only be admitted when the retarding potential is equal in magnitude to the amount of energy that they have lost. In practice, some allowance has to be made for contact potential effects in the electronics and the angular spread of the electrons entering the detectors, and the voltage necessary to admit the elastically scattered electrons was approximately 0.4 V. As the energy of the lowest lying excited state in cadmium is 3.737 eV and in magnesium is 2.711 eV, this was easily able to discriminate against any inelastically scattered electrons which would lose at least that amount of energy in a collision. Each electron hitting the channeltron gives a small (~5mV) pulse which is then picked off via a capacitor and amplified by an Ortec 9301 fast pre-amplifier before being sent to the counting electronics. The basic pick-off and amplification circuit is shown in figure 3.24.

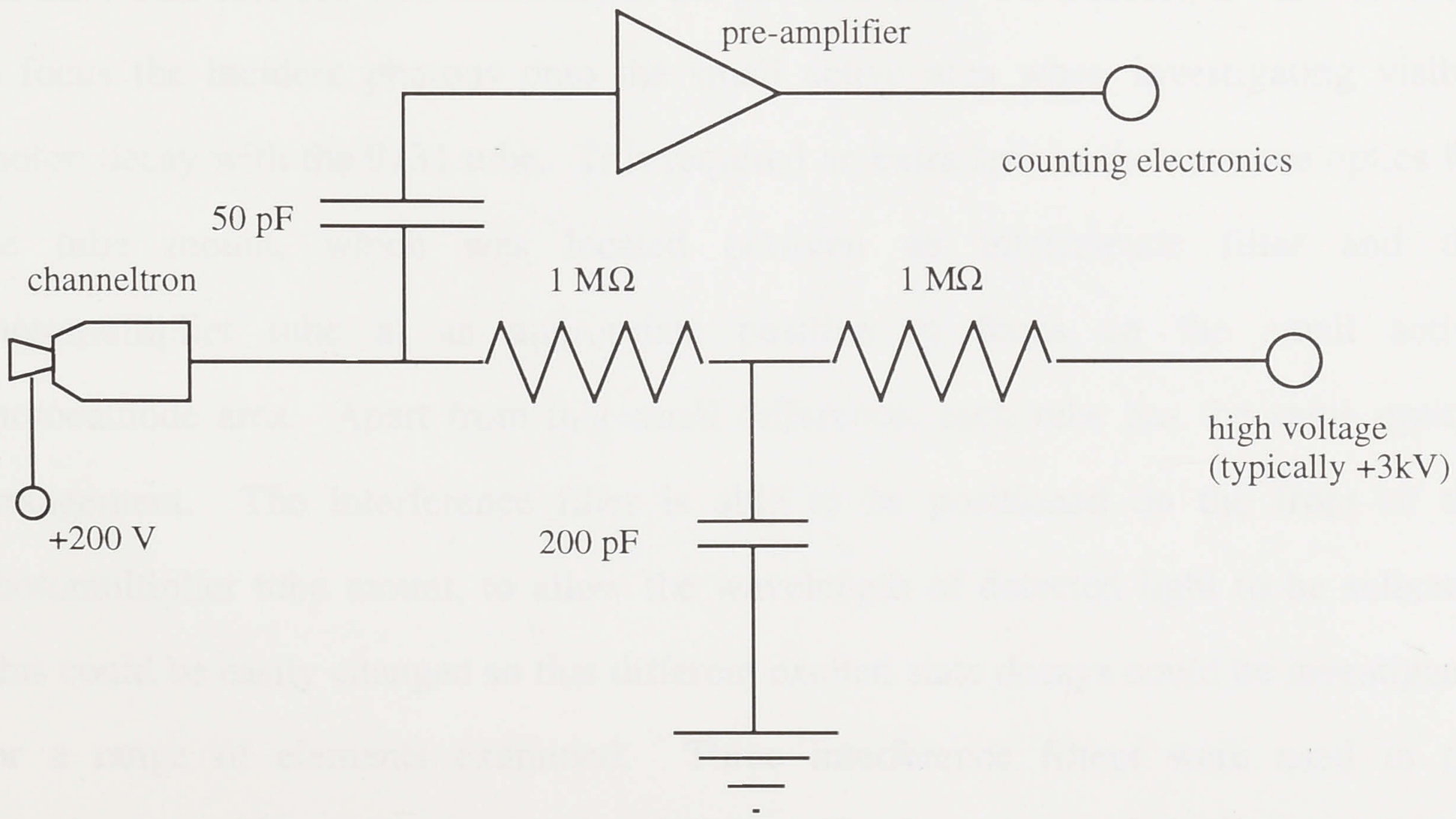

Figure 3.24: Schematic diagram of the pulse pick-off and amplification circuit

The amplified pulse travels through a discriminator (Ortec model 473A) which allows discrimination against any background electronic noise. The discriminator in turn gives a +5V pulse for each amplified channeltron pulse, and the number of pulses is monitored by a ratemeter (Ortec model 661) and recorded by a multichannel analyser which stores the number of pulses received in each channel scanned. The role of the multichannel analyser is further explained in section 3.9.

3.8 Photon detection system

Decay photons from excited states of cadmium and magnesium were detected using two interchangeable photomultiplier tubes. Photons in the ultraviolet range were detected using a Thorn EMI model 9405 photomultiplier tube, and visible photons detected using a Thorn EMI model 9131Q/100 tube. Each tube can be mounted in an aluminium half-cylinder, which is then inserted into a re-entrant tube on one flange of the vacuum chamber. This allows the photomultiplier tubes and the associated electronics to be kept outside of the high vacuum, substantially reducing problems which would be associated with mounting the required electronics inside a high vacuum environment. The mounting arrangements for each tube were slightly different, as shown by figures 3.25 and 3.26. This is due to the fact that the model 9131 tube has a 2 mm diameter active photocathode area, to reduce dark current, and the model 9405 tube has the whole face (25 mm diameter) as the photocathode. As a result, it was necessary to focus the incident photons onto the small active area when investigating visible photon decay with the 9131 tube. This required an extra lens in the entrance optics for the tube mount, which was located between an interference filter and the photomultiplier tube at an appropriate position to focus on the small active photocathode area. Apart from this small difference, each tube has the same optical arrangement. The interference filter is able to be positioned on the front of the photomultiplier tube mount, to allow the wavelength of detected light to be selected. This could be easily changed so that different excited state decays could be investigated for a range of elements examined. Three interference filters were used in the experiments, with centre wavelengths of 228 nm (for the cadmium $3s3p\ ^1P_1 \rightarrow 3s^2\ ^1S_0$

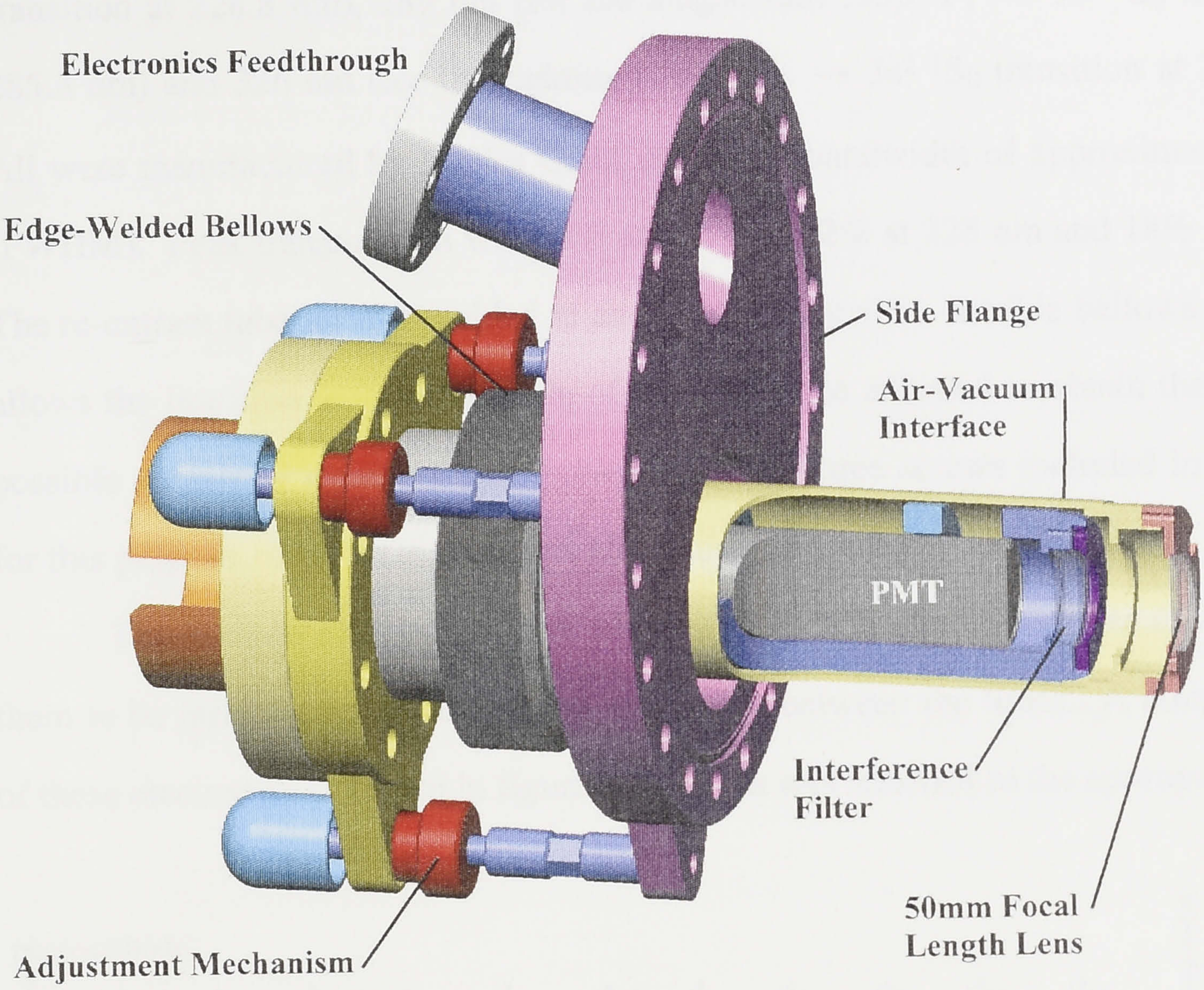

Figure 3.25: Photomultiplier tube arrangement for detection of UV photons

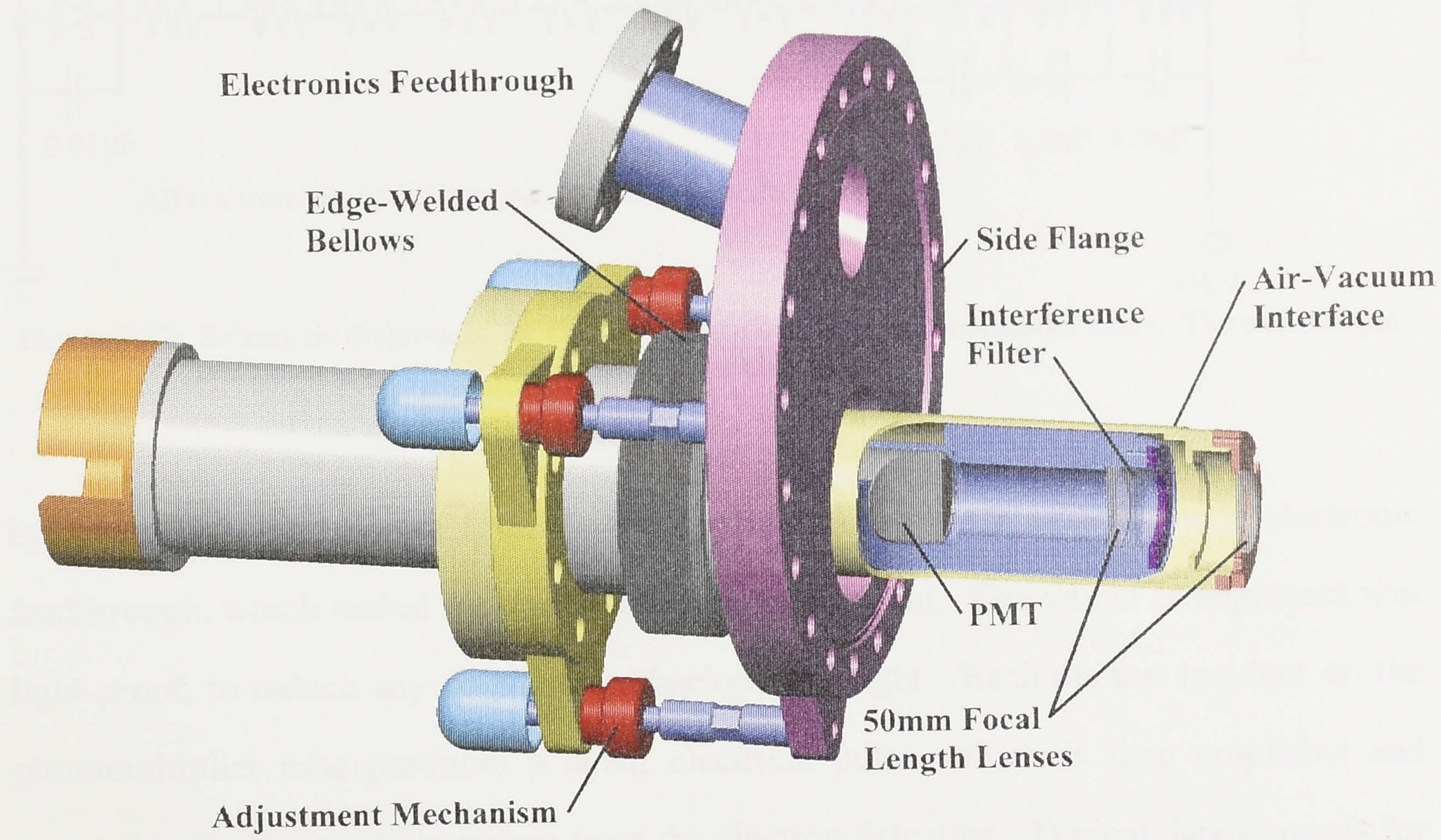

Figure 3.26: Photomultiplier tube arrangement for detection of visible photons

transition at 228.8 nm), 289 nm (for the magnesium 3s3p $^1P_1 \rightarrow 3s^2\ ^1S_0$ transition at 285.3 nm) and 326 nm (for the cadmium 3s3p $^1P_1 \rightarrow 3s^2\ ^1S_0$ transition at 326.1 nm). All were manufactured by Melles Griot and had a bandwidth of approximately 10 nm (FWHM). Peak transmission was 58% at 326 nm, 22% at 228 nm and 18% at 289 nm. The re-entrant tube itself is welded to an 8 inch flange via a flexible bellows. This then allows the insertion length and angle of the tube to be adjusted to obtain the maximum possible signal, by means of manipulation via the three screws included in the design for this purpose. This arrangement is also shown in figures 3.25 and 3.26.

The dynode electronics were identical for each photomultiplier tube, allowing them to be mounted in one unit, interchangeable between the tubes. A circuit diagram of these electronics is shown in figure 3.27. This was attached to the appropriate tube

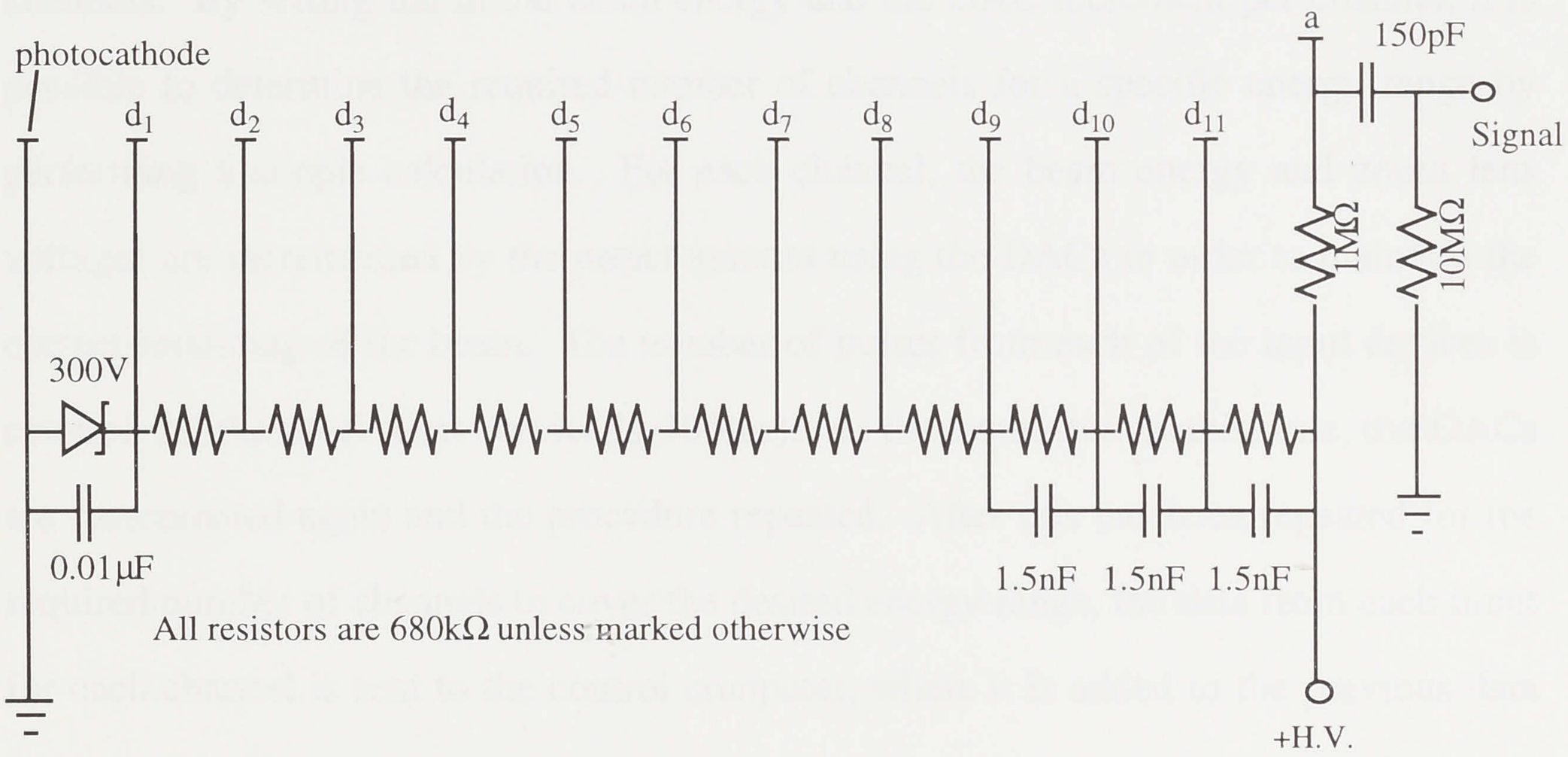

Figure 3.27: Schematic diagram of the electronic circuit for the photomultiplier tubes. The external pin connections are also shown

by a standard plug (Thorn EMI model B14B) and then to a custom made electronic feedthrough, which sealed the photomultiplier tube mount. The whole arrangement was light-proof, to reduce any counts from background light. Each photon incident on the photomultiplier tube produces a small electrical pulse, which is then amplified and counted in the same way as pulses from the electron detectors. Typical dark currents for the two tubes, which were operated at room temperature, were approximately 10 Hz for the UV tube and 50 Hz for the visible tube.

3.9 Data collection and analysis

Data from the experiment is collected by a custom built multichannel analyser (MCA) which records the number of detected particles (photons or electrons) as a function of incident energy. The computer controlled MCA has several digital-to-analog converter outputs (DACs) which are used to incrementally increase the electron beam energy and the appropriate zoom lens voltage, whilst the 5 input channels are used to count the number of pulses from the electron detectors or photomultiplier tube at each energy. Operating parameters for the MCA are predetermined by the operator, and relayed to the MCA by means of a computer program written specifically for the task. This gives the voltage increment for the beam energy and zoom lens DACs, and the dwell time (the time for which data is collected) for each of a chosen number of channels. By setting the initial beam energy and the DAC increment per channel, it is possible to determine the required number of channels for a specific energy range by performing a simple calculation. For each channel, the beam energy and zoom lens voltages are incremented by the preset amount using the DACs in order to maintain the correct focussing of the beam. The number of pulses from each of the input devices is counted for the dwell time (typically 100ms). At the expiration of this time, the DACs are incremented again and the procedure repeated. After this has been repeated for the required number of channels to cover the desired energy range, the data from each input for each channel is sent to the control computer, where it is added to the previous data and saved to file. The energy range is then scanned again. Cumulative data from each input is able to be viewed as the experiment is operating, allowing the progress of the experiment to be monitored. The experiment can then be halted after a predetermined time, or by the operator when it is decided that sufficient data has been collected. The software to control the experiment was specifically written for these experiments, using the Delphi 2 (Borland International) software package, and allows all the necessary experimental parameters to be monitored and collated simultaneously. Data is saved in simple text files, which were then able to be accessed and analysed using standard graphical analysis software after the completion of the experiment. The techniques used for the analysis of the data are discussed in chapter 4.

3.10 Metastable Cadmium Detection

This section outlines an attempt that was made to investigate the production of metastable cadmium atoms as a function of energy, in a similar way to measurements that have been performed on mercury by Newman et al. (1985). The two metastable states of interest to this study are the 5p $^3P_{0,2}$ states, at energies of 3.74 eV and 3.95 eV. These states are long-lived because photon decay to the ground state (the only state of cadmium below them in energy) is a dipole forbidden transition.

In metastable production experiments, the metastable atoms are detected by colliding with a surface that has a work function that is lower than the energy of the excited metastable state. This process causes an electron to be released from the surface which can then be detected by a channeltron. For experiments on rare gases, such as helium or argon, the front cone of a channeltron provides an adequate surface, as the work function is typically around 6-8 V, which is much smaller than the energies of the lowest metastable state (19.82 eV in helium and 11.54 eV in argon) being detected. The major difficulty in metastable production experiments on heavy metals is that the energy of the metastable states is much lower so that an alternative, low work function, surface is required. Several experiments in the past have measured excitation of various metastable states of mercury. The first metastable excitation measurements in mercury were made by Lichten (1958) on the 6p $^3D_3$ excited state which occurs at an energy of 8.792 eV, and this was followed by experiments by Borst (1969 and 1977), Newman et al. (1983 a, b and 1985) and Koch et al. (1984). The later experiments all measured lower lying metastable states, down to the first metastable state in mercury at an energy of 4.660 eV (6p $^3P_0$), using a variety of methods. The measurements by Newman et al. (1983a,b and 1985) were of the most interest with regards to this work, as their measurements were made using a samarium surface, which has a work function of approximately 2.7 eV. The first metastable states in cadmium are the 5p $^3P_{0,2}$ states at energies of 3.737 eV and 3.949 eV, which means that it should be possible to detect these states by impact on a samarium surface. In order to measure a metastable excitation function for cadmium, a detector was designed and built to take advantage of the low work function of samarium, and the final design is shown in figure 3.28. The

detector assembly is a box with an entrance aperture that was positioned directly in the cadmium beam, after its intersection with the electron beam. Two macor pillars were used to mount the detector box from the top hat, to ensure electrical isolation from the top hat which is kept at ground potential. The entrance aperture is a square, 11x11 mm, which is covered with a fine copper mesh. Both the mesh and the detector box were kept at the beam potential during the experiments, so that the electron beam was not

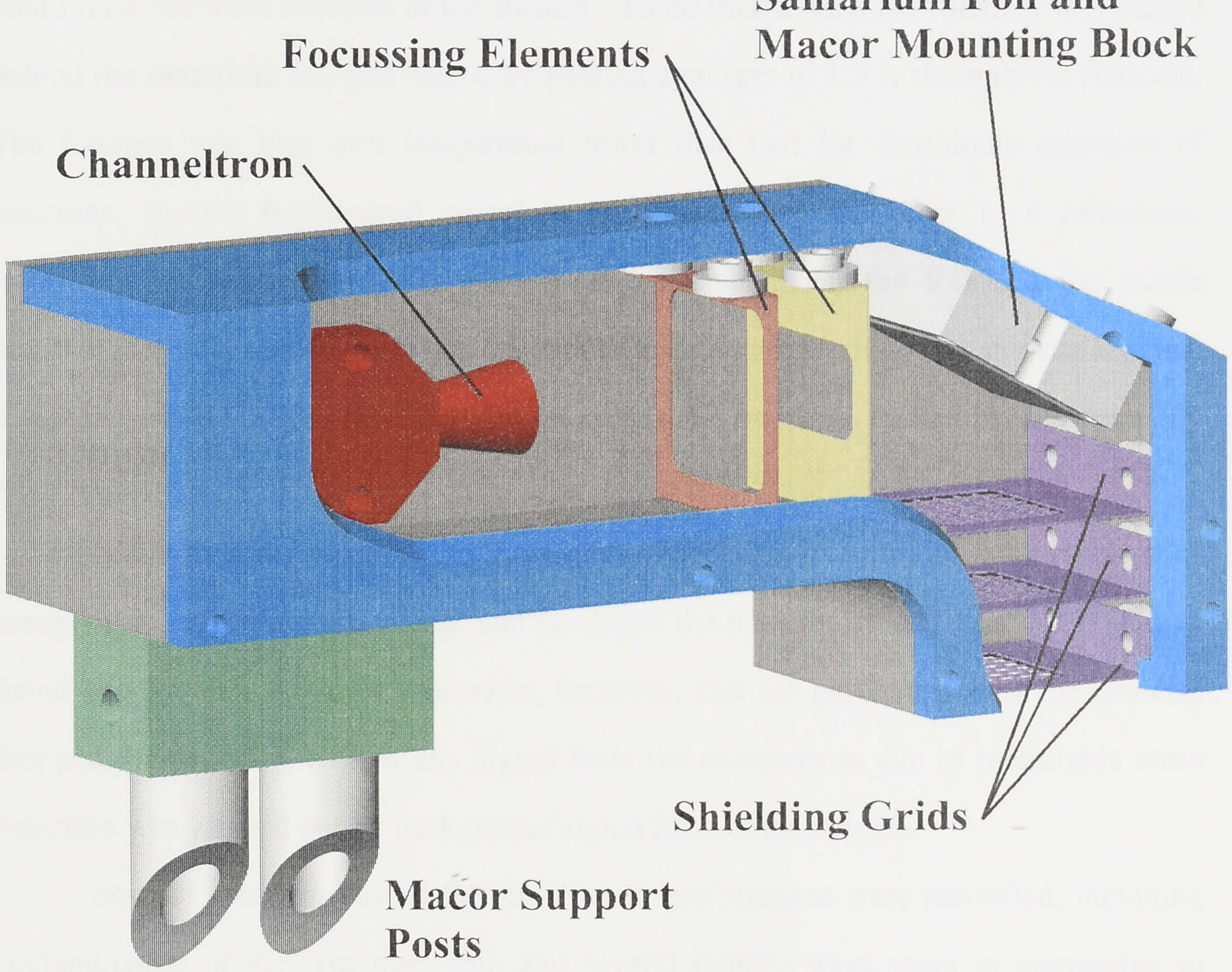

Figure 3.28: Metastable cadmium detector

affected, and so there was no field penetration from any of the other elements housed inside the detector box. A small (12.5x12.5 mm) square of samarium foil is mounted at an angle of 30° to the incident cadmium beam, at the end of the entrance channel which is approximately 20mm long. Between the foil and the entrance aperture are two further mesh covered apertures, also 11x11 mm, which were maintained at potentials of +20 V and -5 V, to ensure that no electrons or ions penetrated into the detector. At 90° to the

entrance channel is another channel of approximately 60 mm in length, inside of which there are two electrostatic focussing elements and a channeltron. The samarium foil was kept at a slightly negative potential to ensure that any electrons originating at the foil (from a metastable collision) would be directed away from the foil and, via the focussing optics, onto the collecting cone of the channeltron. One critical aspect of the detector was to ensure that the samarium foil remained free of contamination which could raise the work function of the surface. To do this, a tungsten filament was placed behind the samarium foil and heated by passing a current of 1.5 A through the filament. The filament was kept at a temperature lower than that for thermionic emission of electrons, so that background signal to the channeltron was kept to a minimum. However, this temperature was enough to radiatively heat the foil and the whole detector assembly so that there was no cadmium deposition evident on any surface, and it was presumed that this also kept the samarium foil free from contamination from any other source.

Initial measurements of the metastable production in cadmium as a function of energy were extremely promising, and produced the data shown in figure 3.29. It was found shortly after this data was taken, however, that the performance of the detector dropped dramatically, so that any signal from the channeltron due to metastable atom detection was washed out by background signal from other sources.

Several possible reasons for this drop in performance were identified, including contamination of the samarium foil, and several months were spent in attempting to rectify the problem. Changing the samarium foil had no effect on the performance of the detector, and no other solutions to the problems with performance were able to be found in this period. As a result, it was decided to abandon the attempt to measure metastable excitation in cadmium during the course of this thesis.

Despite the problems encountered in this case, there are promising signs for future attempts to be made for these types of measurements. The fact that at least one metastable production spectrum was obtained indicates that these experiments should be possible. When the gap between the work function of the surface and the excited state energy of the metastable atom is small, the efficiency of ejection of an electron from a

surface struck by the atom is approximately linearly proportional to the difference between the excited state energy and the work function. It may be that this difference between the work function of samarium and the energy of the cadmium metastable states (approximately 1 eV) means that small environmental factors can have enough effect to render the experiments very difficult. Thus a new detector design, which gives more control over the cleanliness of the samarium surface for instance, may be more successful. Measurement of the metastable excitation functions for other atoms with higher energy metastable states should be possible using this sort of detection scheme, as the efficiency of detection should rise.

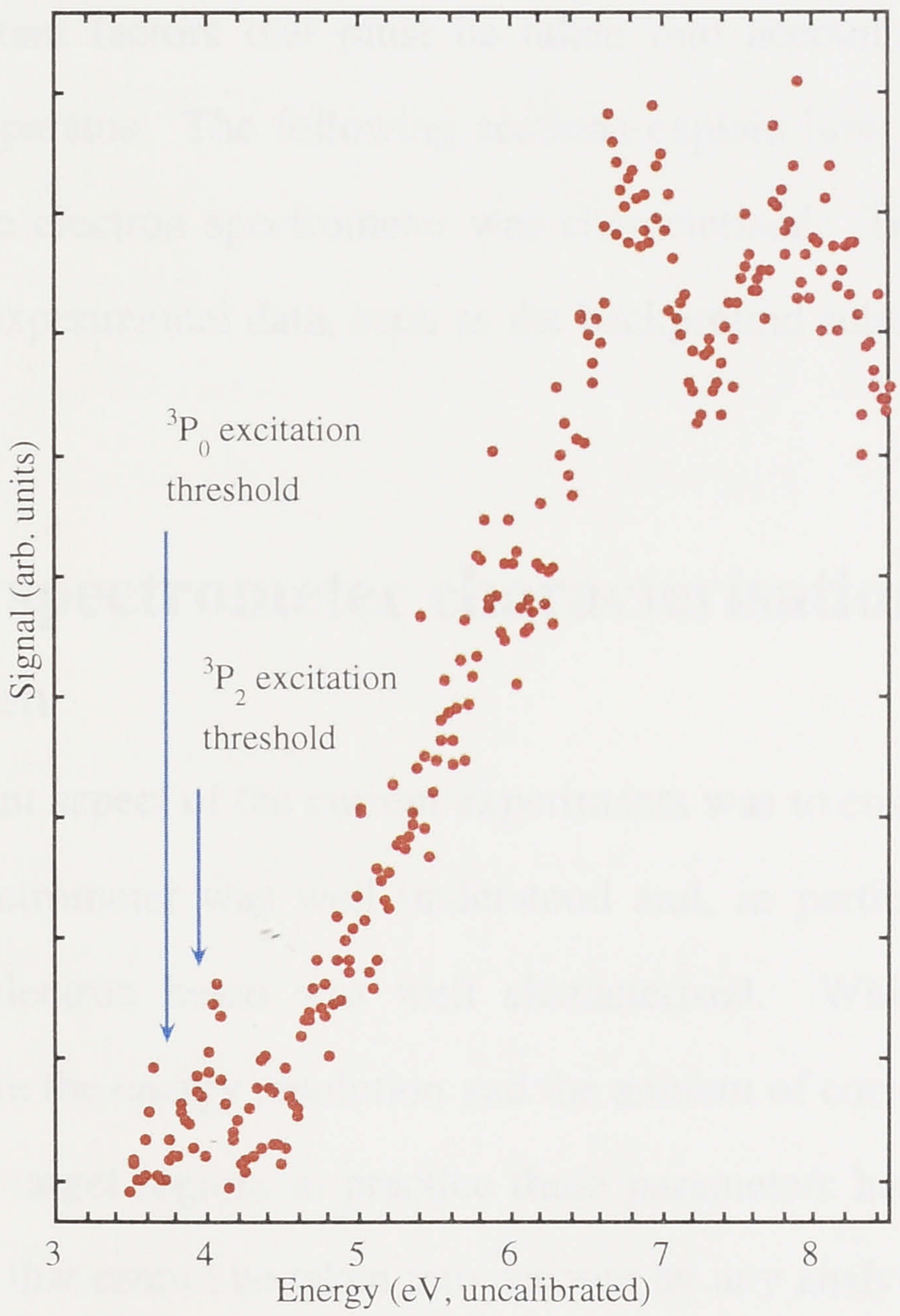

Figure 3.29: Metastable excitation spectrum for cadmium. Approximate positions of the metastable state excitation thresholds are shown by the blue arrows.

Chapter 4

Experimental Techniques

In this chapter a brief overview of some of the techniques used to collect and analyse the data will be given. When examining negative ion resonances, there are several very important factors that must be taken into account, such as the energy resolution of the apparatus. The following sections explain how the energy resolution and operation of the electron spectrometer was characterised. The techniques used in the analysis of the experimental data, such as the background subtraction technique, are also discussed.

4.1 Electron spectrometer characterisation

4.1.1 Introduction

One important aspect of the current experiments was to ensure that the operation of the electron spectrometer was well understood and, in particular, that the energy resolution of the electron beam was well characterised. Whilst it is possible, in principle, to calculate the energy resolution and the amount of current transmitted by the spectrometer to the target region, in practice these parameters have to be measured to allow for variations that cannot be taken into account by any analytical model. It is also important to ensure that the operation of the spectrometer is stable, so that the same conditions are maintained throughout the duration of the experiments.

In this case, it is straightforward to monitor the electron current produced by the spectrometer as experiments are being performed, by means of the Faraday cup. The current in all of the scattering experiments presented in this thesis was typically 1nA, and it remained reasonably stable during the long data collection times that were often required. Some deterioration in the electron beam would occur over time (i.e. the

magnitude of the current would drop slowly over several days), but this was usually addressed by stopping data collection and retuning the electron monochromator, before recommencing experiments.

In the present experiments, almost all of the negative ion resonance features which have been observed in the metal vapour targets have energy widths which are substantially larger than that of the electron beam. Thus it was not possible to monitor the energy resolution continuously from the experiments themselves. This had to be done separately to the metal vapour experiments, and two different gas-beam experiments were used to measure the energy resolution; electron scattering from argon and nitrogen. Both of these experiments made use of the fact that in each case there is a negative ion resonance feature in the systems studied which has a small natural width. If a feature such as this has a much narrower energy width than the resolution of the electron beam, then its width in a measured cross section will be largely due to the energy spread in the electron beam. Thus, by measuring the width of the feature in the cross section, it is possible to obtain a measure of the energy resolution of the electron spectrometer.

4.1.2 Electron scattering from argon

The first experiment performed to measure the energy resolution of the electron beam was metastable atom production in electron scattering experiments from argon. Brunt et al. (1976) and Buckman et al. (1983b) measured the production of the $3p^5 4s$ (J=0, 2) metastable states of argon, in a crossed beam configuration, and found many negative ion resonance features in the resulting spectrum. The feature of particular interest in the present case is the first feature in the "e-series" identified by Buckman et al. In their measurements, this feature is located at an energy of 12.925 eV, and has an energy width of 12.5 meV, which was comparable to the energy resolution of the spectrometer used in their experiments. This is an indication that the natural energy width of the resonance is very small (<1 meV), and hence it is ideal for this sort of characterisation. This feature has been classified as one of the family of $Ar^- 3p^5(4p^2\ ^1D)$ resonances. The critical point for the current measurements is, however, that it has an

extremely small energy width. On this basis, any measurements of this feature that are made using the current experimental apparatus will give a good and direct indication of the energy resolution of the electron beam.

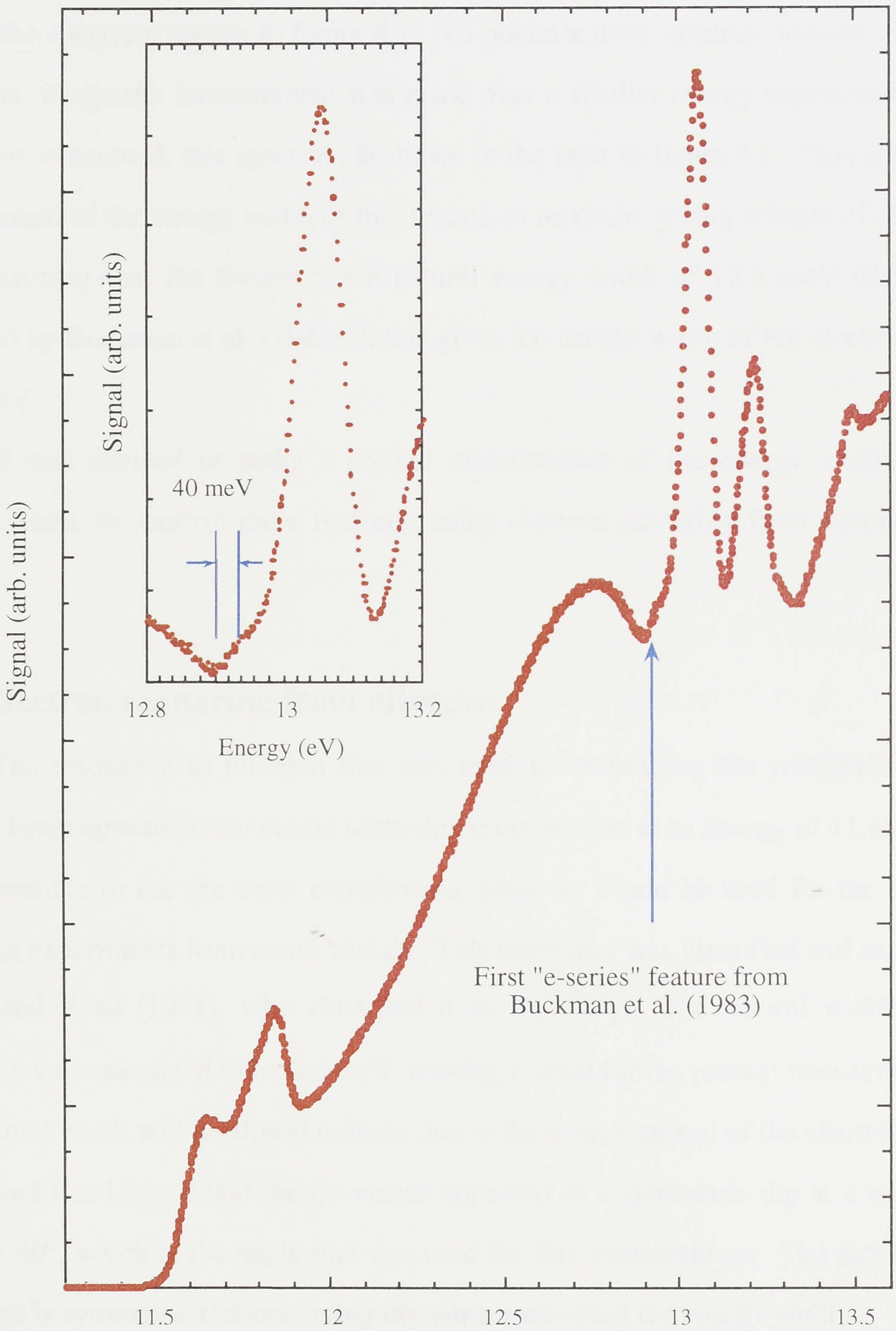

Figure 4.1: Metastable production in electron scattering from argon
Inset: Spectrum over reduced energy range

To perform these measurements, a metastable detector was placed in the path of an incident argon beam, at right angles to the electron beam, as described in chapter 3. The energy of the electron beam was increased from 11.25 to 13.6 eV in 2.135 meV steps, with the number of metastable atoms produced at each energy recorded. This yielded the spectrum shown in figure 4.1. To obtain a more accurate indication of the resolution, a separate measurement was made over a smaller energy region containing the feature concerned, this spectrum is shown in the inset in figure 4.1. This allowed a measurement of the energy width of this feature to be made, giving a value of 40 meV. Even assuming that the feature has a natural energy width of 12.5 meV (the width measured by Buckman et al. (1983b)), this gives the energy width of the electron beam as 38 meV.

It was decided to make a second measurement of the energy width of the electron beam, to confirm these findings, using electron scattering from nitrogen as a guide.

4.1.3 Electron scattering from nitrogen

The resonance in nitrogen that was used for measuring the resolution of the electron beam appears in the elastic scattering cross section at an energy of 11.48 eV, so it was possible to use the same experimental setup as would be used for the electron scattering experiments from heavy metals. This resonance was identified and studied by Comer and Read (1971), who classified it as $N_2^-\ ^2\Sigma^+_g$. The natural width of the resonance was calculated to be 0.6 meV, making it ideal for the present measurement as it's apparent width will be almost entirely due to the energy spread of the electron beam. Comer and Read found that the resonance appeared as a symmetric dip at a scattering angle of 40^o, which is the angle that was used for this measurement. The fact that the resonance is symmetric reduces ambiguity when measuring the energy width.

For these measurements the same experimental setup was used as intended for the experiments from metal vapours, with the nitrogen source admitted into the upper chamber through a large aperture in the top hat separating the two chambers. This procedure has been further discussed in chapter 3. The high temperature oven for the

production of a metal vapour beam can be in place whilst the experiment is being carried out, meaning that the measurement of the resolution can take place immediately before the experiments on the metal atoms. This has the advantage that there is no need to make any changes to the experimental configuration between the measurements, so that conditions for each experiment can be as close as possible.

The spectrum obtained for elastic electron scattering from nitrogen at 40^{o} can be seen in figure 4.2a. As shown in this data, the full width at half maximum (FWHM) of the dip due to the resonance is approximately 35 meV. This is consistent with the result obtained with argon in the previous experiments. This is typical of the resolution with which the experiments on cadmium and magnesium were carried out.

To check the stability of the operation of the electron spectrometer, in addition to monitoring the current that was produced whilst the experiments were taking place, the measurements on nitrogen were repeated when the experiments on cadmium were completed, and before the commencement of experiments on magnesium. The spectrum obtained on this occasion is shown in figure 4.2b. It can be seen that there is no change in the energy resolution measured in the two separate experiments, giving confidence that the operation of the spectrometer remained stable throughout the course of all the experiments on the metal atoms.

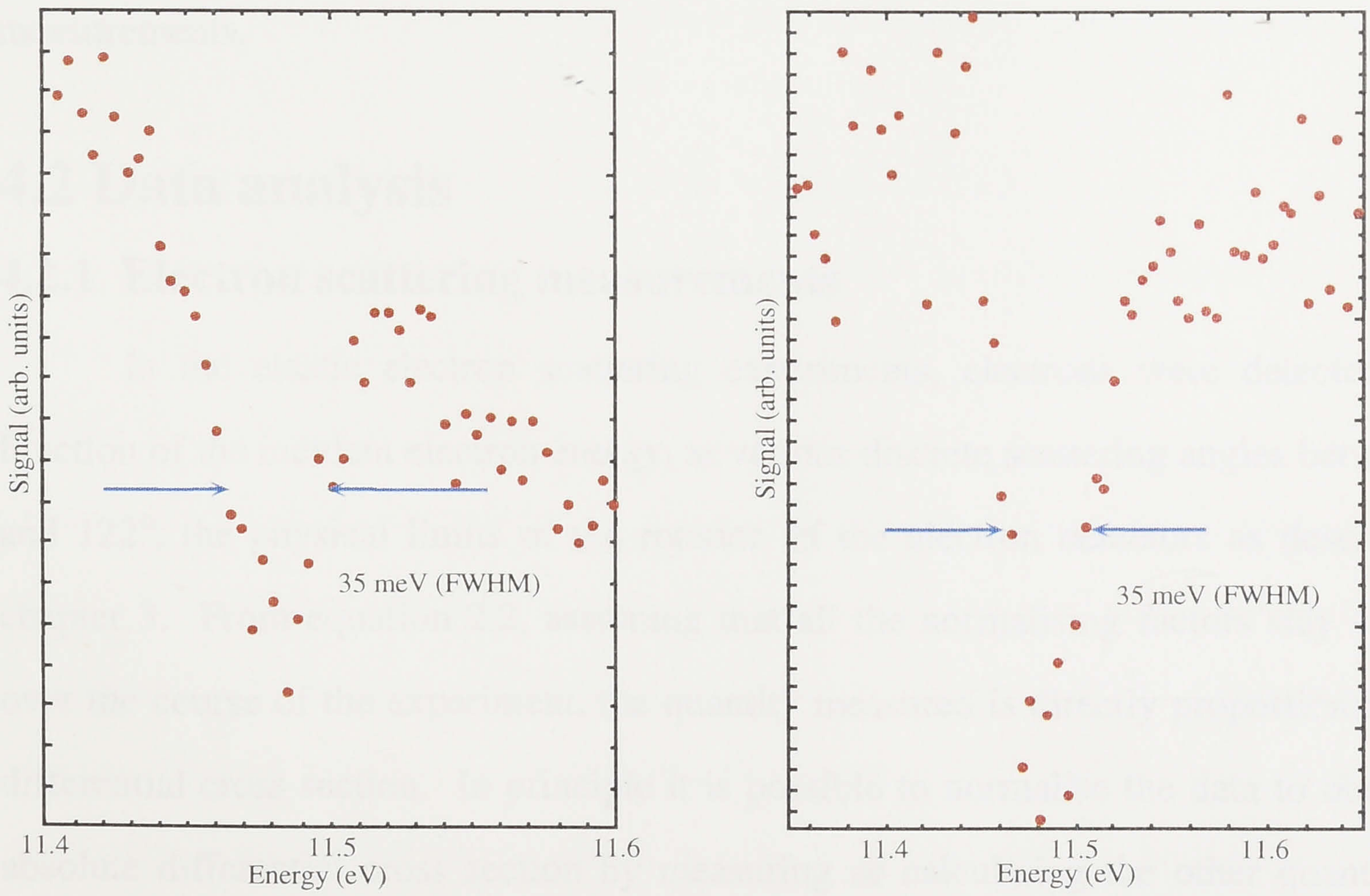

Figures 4.2a&b: Elastic electron scattering from nitrogen, at a scattering angle of 40 degrees

4.1.4 Energy calibration

It is very important to know the precise energy of the electron beam in these types of experiments, so that a proper determination of where the negative ion resonances occur can be made. Whilst the nominal energy of the electron beam can be measured simply by a voltmeter on the last element of the electron optics, typically there is some offset (up to 400 meV) between this reading and the true energy of the electron beam due to factors such as contact potential effects between the various elements in the electron spectrometer. In the present experiments the most reliable technique was to observe the onset of the photon decay channels. These energies are precisely known from spectroscopic observations and calculations. In the case of cadmium, the spectroscopic decay channels which were examined were the 5p $^1P_1$ and 5p $^3P_1$ states to the $5s^2\ ^1S_0$ ground state with threshold energies of 5.417 eV and 3.804 eV respectively (C. E. Moore, 1971). For magnesium, the transition used was that from the 3p $^1P_1$ state to the $3s^2\ ^1S_0$ ground state at an energy of 4.349 eV (C. E. Moore, 1971). In this way, the energy scale of the experimental data could be determined with an accuracy of approximately 25 meV. This technique had the added advantage that the energy offset was able to be measured during the experiments, as the photon decay measurements for metal vapours were made in parallel with the electron scattering measurements.

4.2 Data analysis

4.2.1 Electron scattering measurements

In the elastic electron scattering experiments, electrons were detected, as a function of the incident electron energy, at various discrete scattering angles between 24 and 122°, the physical limits of the rotation of the electron detectors as described in chapter 3. From equation 2.2, assuming that all the normalising factors stay constant over the course of the experiment, the quantity measured is directly proportional to the differential cross section. In principle it is possible to normalise the data to obtain the absolute differential cross section by measuring or calculating the other quantities in equation 2.2, but in practice the errors in this method make it highly inaccurate.

Measurement of the differential cross section for electron scattering has the advantage of leading to a direct identification of the classification of any observed negative ion states. If the resonance occurs in a single partial wave, then the angular distribution of the autodetached electron is governed by the Legendre polynomial of that particular partial wave, $P_l(cos\theta)$. The form of the Legendre polynomials for different values of l are given below.

$$P_0(\cos\theta) = 1$$
$$P_1(\cos\theta) = \cos\theta$$
$$P_2(\cos\theta) = 1 - 3\cos^2\theta$$
$$P_3(\cos\theta) = 3\cos\theta - 5\cos^3\theta$$
$$\text{etc.} \qquad (4.1)$$

Thus if the autodetached electron has l=0 (s-wave), the angular distibution is isotropic, if it has l=1 (p-wave) there is a minimum in the resonance contribution at a scattering angle of 90°, if it has l=2 (d-wave), there will be a minimum in the contribution at 54° and 126°, and so on for higher values of the angular momentum. By measuring the angular distribution of the autodetached electron, and if the initial and final state of the electron-atom scattering system is known (in the current experiments only elastic scattering is investigated), the resonance classification can then be inferred from relatively simple arguments based on conservation of angular momentum and parity.

4.2.2 Background subtraction and normalisation

Some of the resonances that have been studied in the present experiments make quite a small contribution to the cross section in which they are observed. It is useful to be able to enhance the presence of the resonance when it is very small, so that is possible to effectively investigate the variation of the resonance strength with scattering angle. One method used to achieve this is to subtract the contribution from the background cross section, thus leaving only the variation due to the resonance. There are a number of possible ways to perform this procedure. In the present case, the experimental data is first fitted with a smooth curve, mimicking the directly scattered background. This background is then subtracted from the experimental data, leaving

only the contributions of the negative ion resonances. This can then be expressed as a percentage of the directly scattered background, so that the contribution of the resonance to the scattering cross section at different angles can be compared, despite the difference in absolute magnitude of the cross section between the different angles and energies.

When the resonance being investigated is larger, and able to be clearly distinguished from the directly scattered cross section, it is still useful to compare the relative magnitude of the resonance feature at different angles. That is, to measure the relative contribution of the resonance to the cross section at each angle. To do this, the measured distribution is normalised to the maximum number of counts (ie: the largest cross section) in the energy distribution. This then gives a normalised measure of the size of the resonance contribution, allowing the contribution at different angles to be compared.

Chapter 5

Results

In this chapter, the results of the experiments on magnesium and cadmium will be presented, and the observations of resonances and their behaviour in the various spectra noted. Discussion and analysis of the results will be presented separately in chapter 6. This has proved advantageous because of the similarities between the electronic structure of the two elements. Each has a similar outer electron configuration, with magnesium having a $3s^2$ outer shell, and cadmium $5s^2$, the major difference between the two being the presence of a full inner d-shell in cadmium. By presenting the analysis of the results in the next chapter, the resonance structure of the two elements can be discussed in tandem, allowing the similarities and differences between the two elements to be highlighted.

5.1 Magnesium

5.1.1 Background

In this section, data is presented for the energy dependence of elastic electron scattering and the excitation function for the 3s3p $^1P_1$ excited state in magnesium. The latter is measured by detecting photons at a wavelength of 285.3 nm which arise from the 3s3p $^1P_1 \rightarrow 3s^2\ ^1S_0$ decay. There has been little previous experimental work investigating negative ion resonances in magnesium. The only direct investigations of resonances have been by Burrow et al. (1976) in electron transmission experiments, Shpenik et al. (1979) who investigated excited state excitation functions and Burrow (1998) who once again used the electron transmission technique, but with substantially improved energy resolution. Resonances have also been observed in experiments by Karstensen and Köster (1971), Aleksakhin et al. (1973), Leep and Gallagher (1976) and

Shafran'osh et al. (1994). These latter experiments investigated the excitation of various excited states of magnesium, but little or no analysis was applied to any resonance structures observed. In the energy range investigated in these experiments, only Shpenik et al. have proposed classifications for any observed resonances. Burrow (1998) has observed many resonances in the energy region investigated in the present experiments, but no classifications have been proposed for any of these, mainly due to the lack of information about their decay channels.

Theoretical effort in magnesium has concentrated on the low lying resonance which was observed by Burrow et al. (1976) at 0.15 eV, below the energy region of this experiment. Calculations for this resonance have been performed by Van Blerkom (1970), Hunt and Moiseiwitsch (1970), Hazi (1978), McCurdy et al. (1981) and Krylstedt et al. (1987). The only theoretical calculations which deal with resonances in the energy region of this experiment are by Van Blerkom (1970), Fabrikant (1974) and Gedeon et al. (1999). All of these authors have found resonances occuring at the threshold for excitation of the 3p ^{3}P states in magnesium, at an energy of 2.7 eV.

Data in this section will be presented in two separate energy regions, from 2 eV to 4 eV and from 4 eV to 7.644 eV (the first ionisation threshold of magnesium). The reason for this is that a resonance observed at the threshold of the 3p ^{3}P states dominates the differential elastic electron scattering cross section in the first energy region, and warrants analysis separately from the rest of the resonances observed. Electron scattering data has been taken at scattering angles of 24°, 54°, 90° and 120° in each energy range, along with the 285.3 nm photon decay spectrum.

5.1.2 Region 1: 2 eV to 4 eV

In this region there is one resonance feature apparent, which is centred on 2.80 eV and has a width of approximately 250 meV. At 24° it appears as a peak in the differential cross section, at 54° it has all but disappeared, at 90° the resonance again appears, this time as a strong step in the cross section and it appears again as a peak at a scattering angle of 120°. The electron scattering data is shown in figures 5.1, 5.2, 5.3

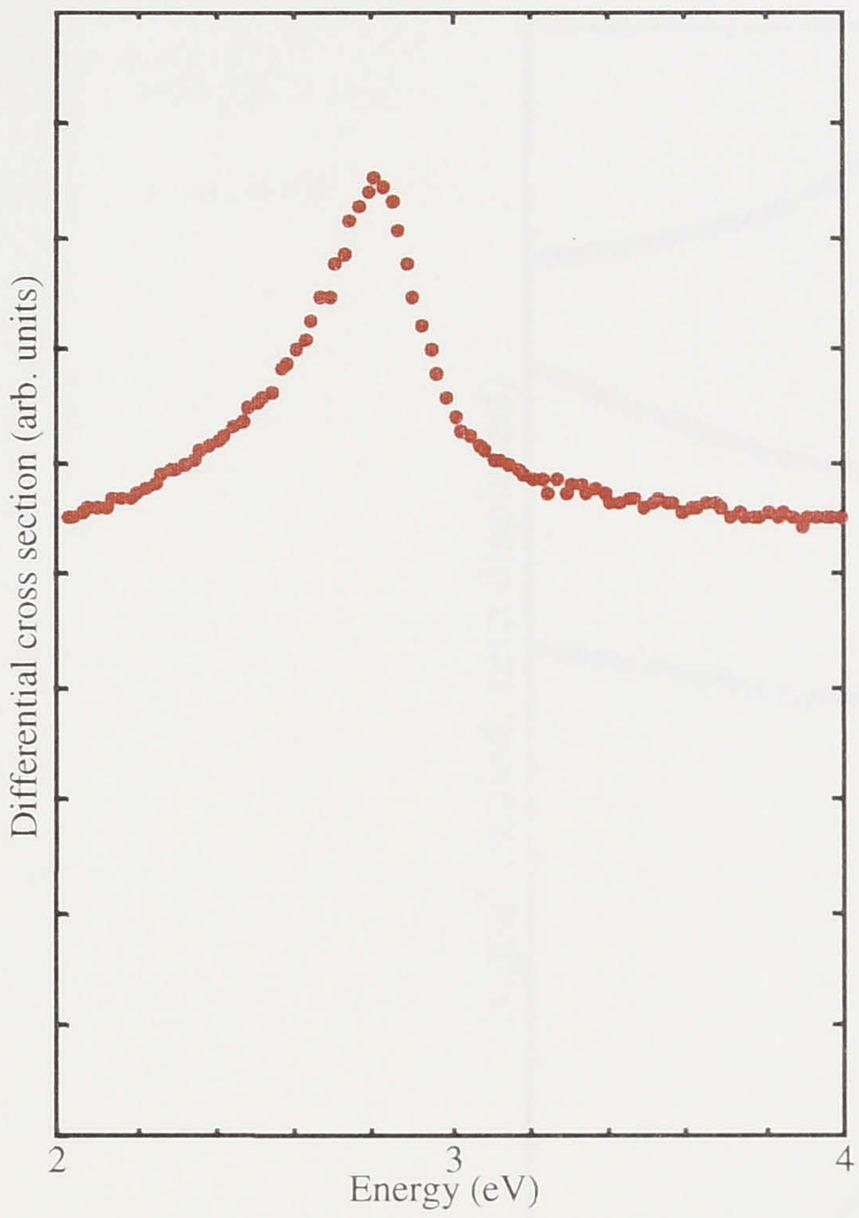

Figure 5.1: Elastic electron scattering from magnesium at 24 degrees

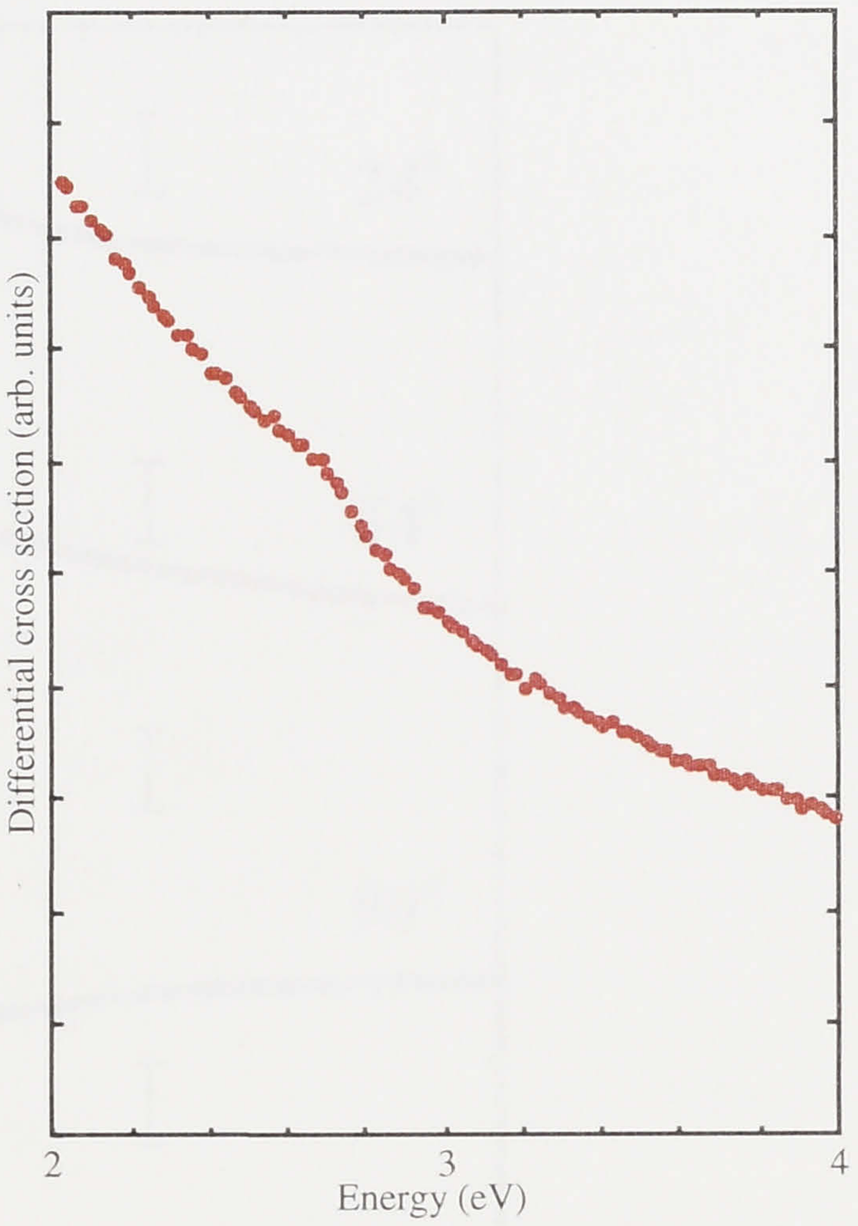

Figure 5.2: Elastic electron scattering from magnesium at 54 degrees

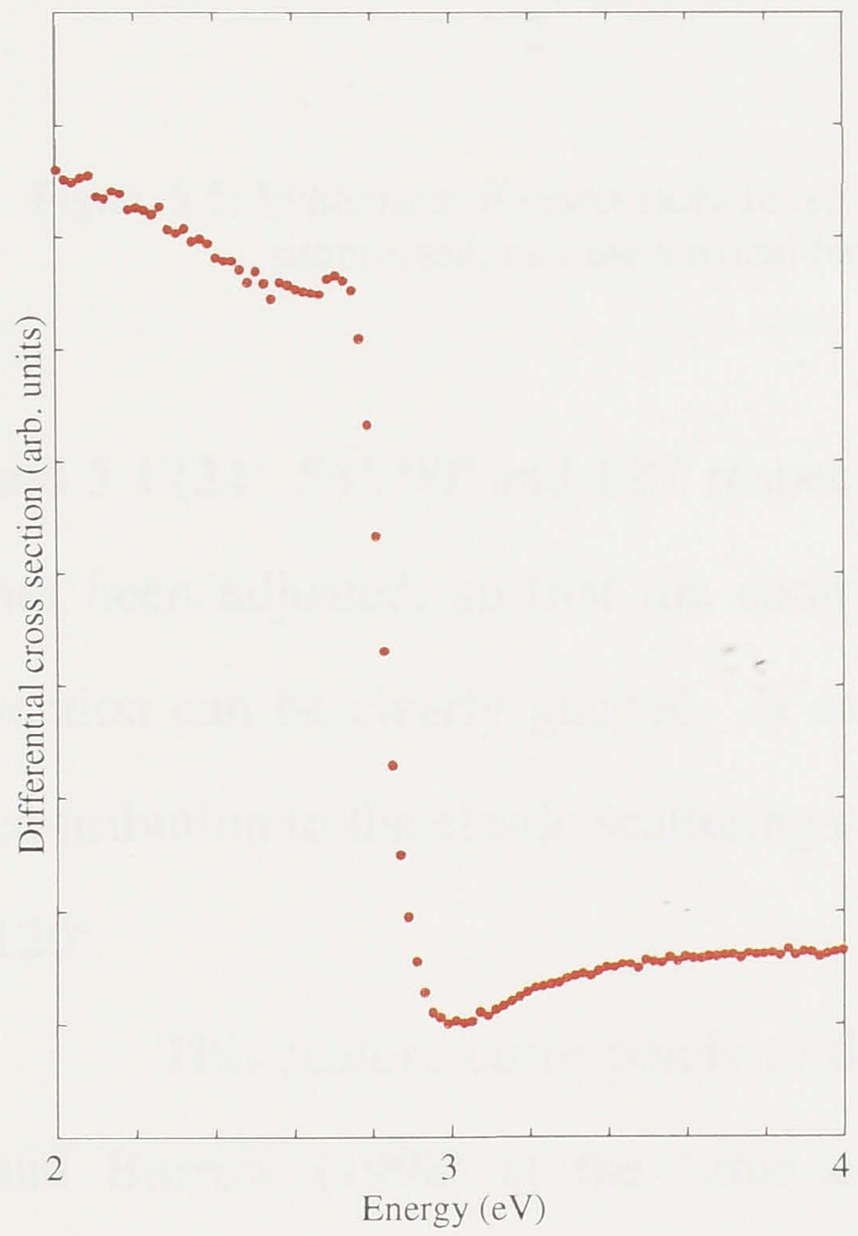

Figure 5.3: Elastic electron scattering from magnesium at 90 degrees

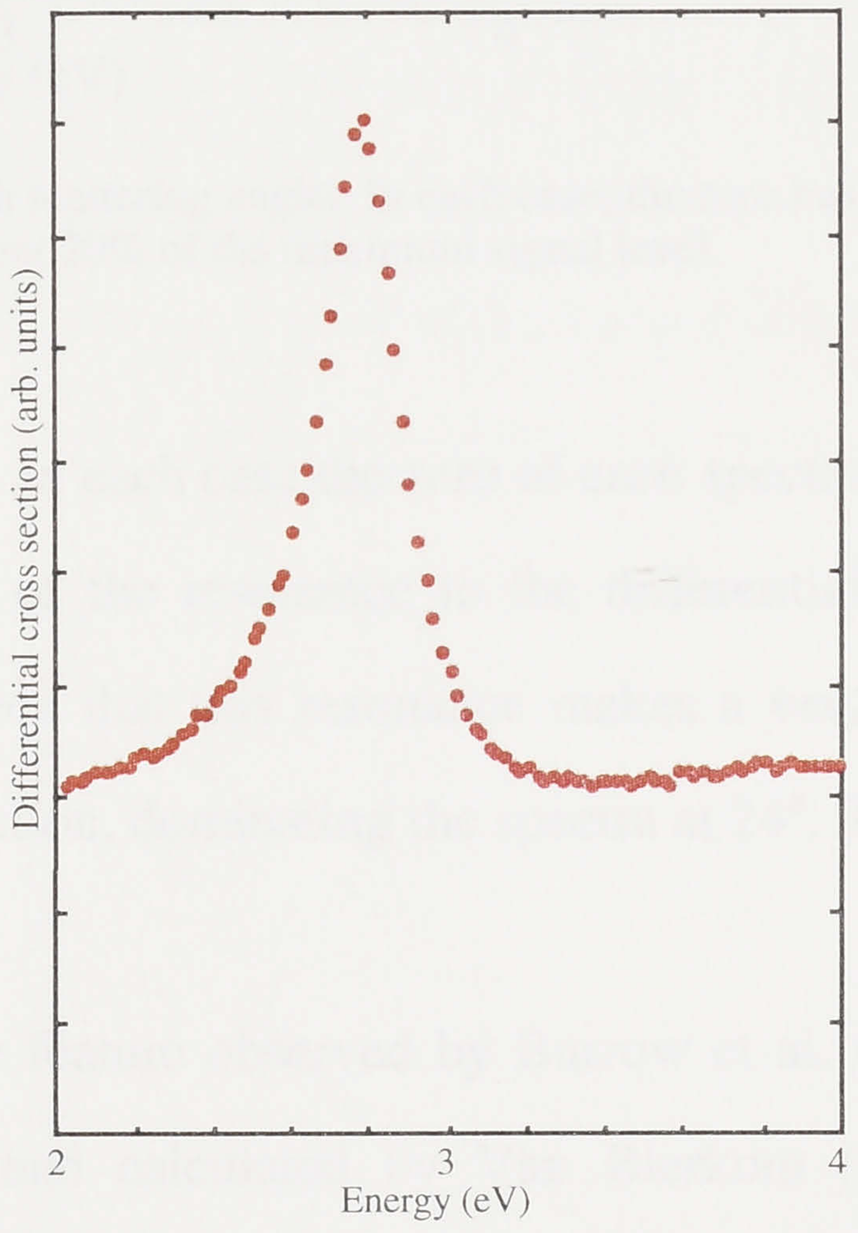

Figure 5.4: Elastic electron scattering from magnesium at 120 degrees

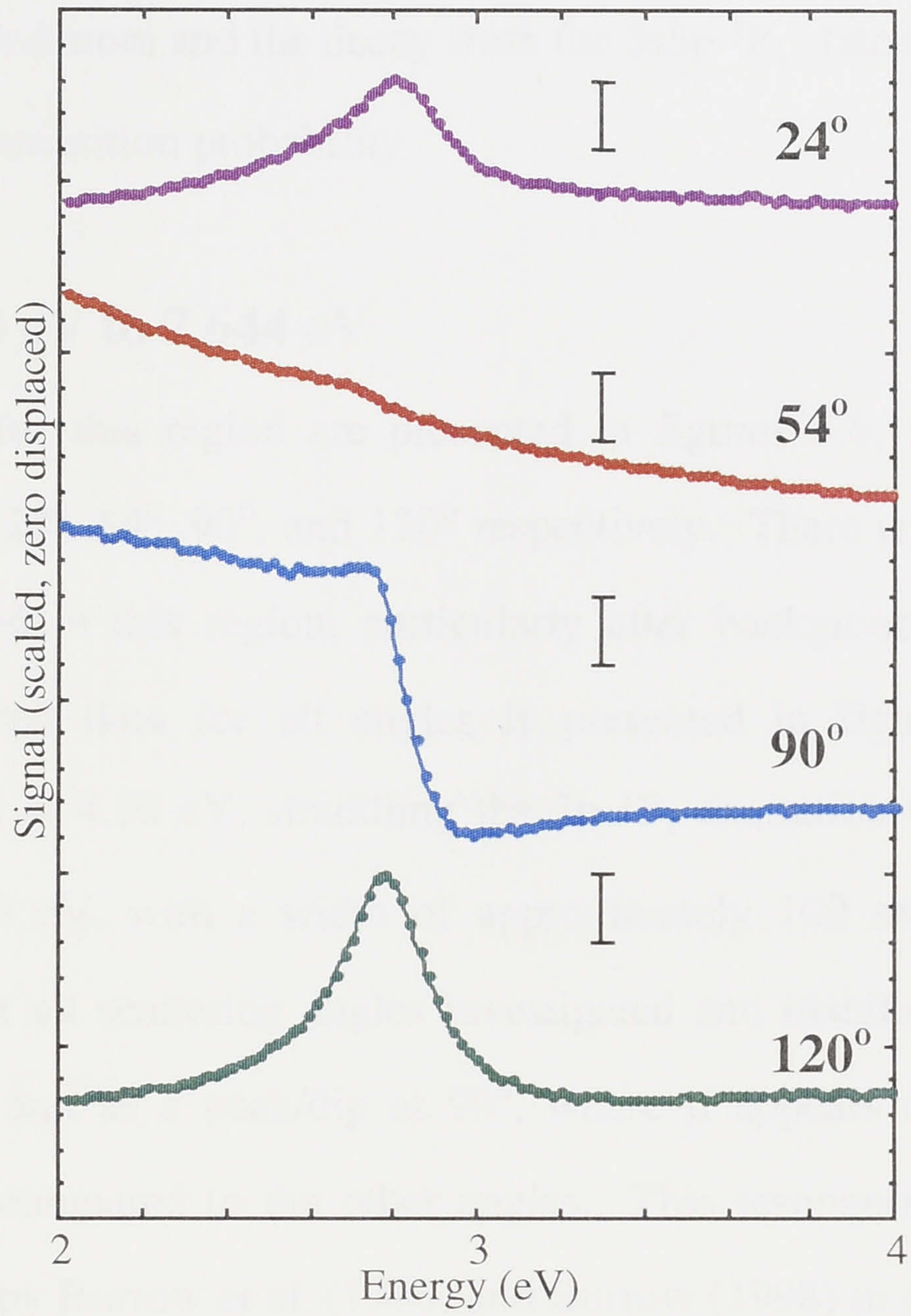

Figure 5.5: Behaviour of resonances in region 1 with scattering angle. In each case, the zero has been suppressed, and the vertical bars represent 20% of the maximum signal level.

and 5.4 (24°, 54°, 90° and 120° respectively). In each case the zero of each spectrum has not been adjusted, so that the contribution of the resonance to the differential cross section can be clearly gauged. It can be seen that this resonance makes a very large contribution to the elastic scattering cross section, dominating the spectra at 24°, 90° and 120°.

This feature corresponds to the large feature observed by Burrow et al. (1976) and Burrow (1998) at the same energy, and calculated by Van Blerkom (1970), Fabrikant (1974) and Gedeon et al. (1999). Figure 5.5 shows the variation of this resonance with scattering angle and it can be clearly seen in this case there is a distinct minimum in the resonance contribution at 54°, indicating that it decays to the ground state by autodetachment of a d-wave electron.

Photon decay data is unavailable for this energy region, as the threshold for the excitation of the 5p $^1P_1$ state lies above the upper limit of this energy region. Unlike

cadmium, it was not possible to investigate the $^3P_1$ excitation function as magnesium is a strongly L-S coupled atom and the decay from the 3s3p $^3P_1$ state to the $3s^2$ $^1S_0$ ground state has a very low transition probability

5.1.3 Region 2: 4 eV to 7.644 eV

The results for this region are presented in figures 5.6, 5.7, 5.8 and 5.9 for scattering angles of 24°, 54°, 90°, and 120° respectively. There are several resonances that can be observed in this region, particularly after background subtraction. The background subtracted data for all angles is presented in figure 5.10. The first resonance is centred at 4.30 eV, straddling the 3p $^1P_1$ excitation threshold for neutral magnesium at 4.349 eV, with a width of approximately 100 meV (FWHM). This resonance appears at all scattering angles investigated and manifests itself as a dip at 24°, 54° and 120°, and as a peak/dip at 90°, where it appears to have a somewhat reduced magnitude compared to the other angles. This resonance corresponds to the resonance observed by Burrow et al. (1976) and Burrow (1998) in electron transmission experiments at the same energy. The next feature apparent in the electron scattering experiments is at 4.85 eV, a structure which appears as a weak peak at a scattering angle

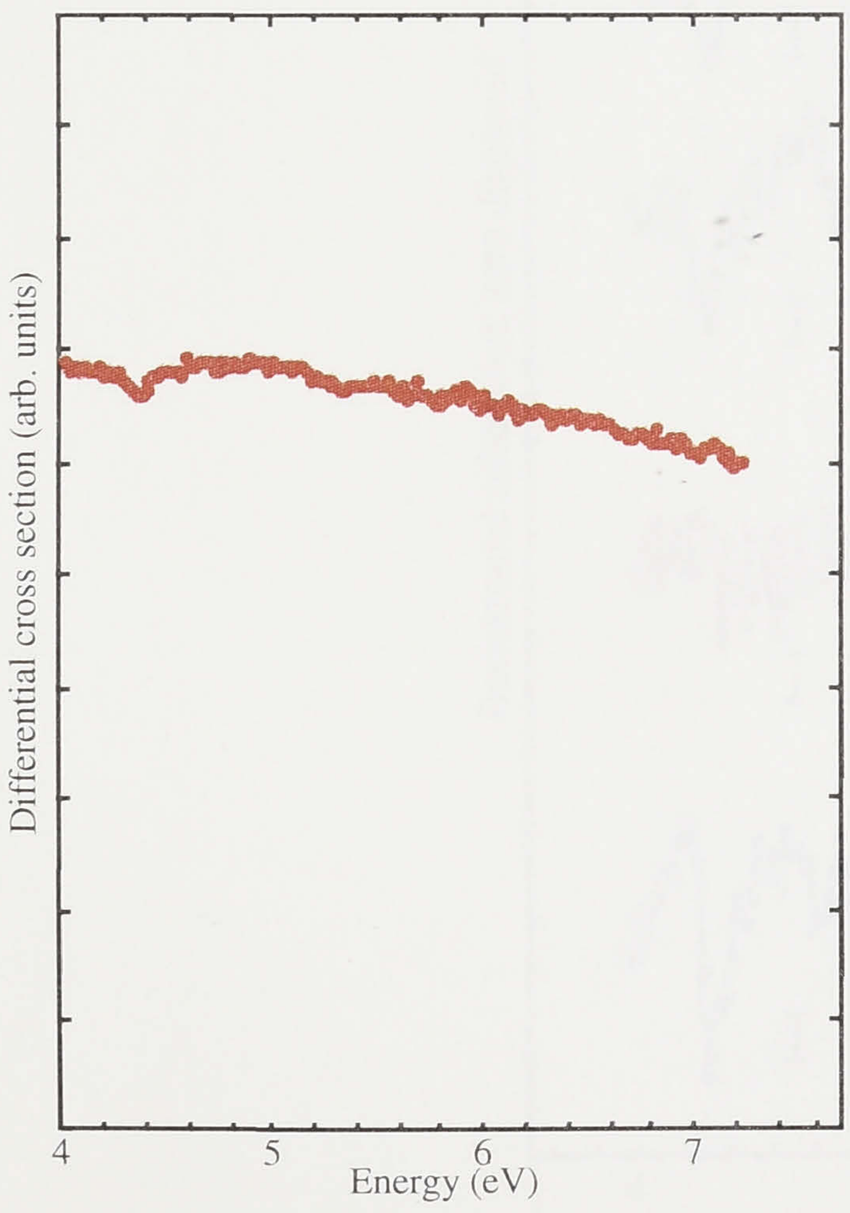

Figure 5.6: Elastic electron scattering from magnesium at 24 degrees

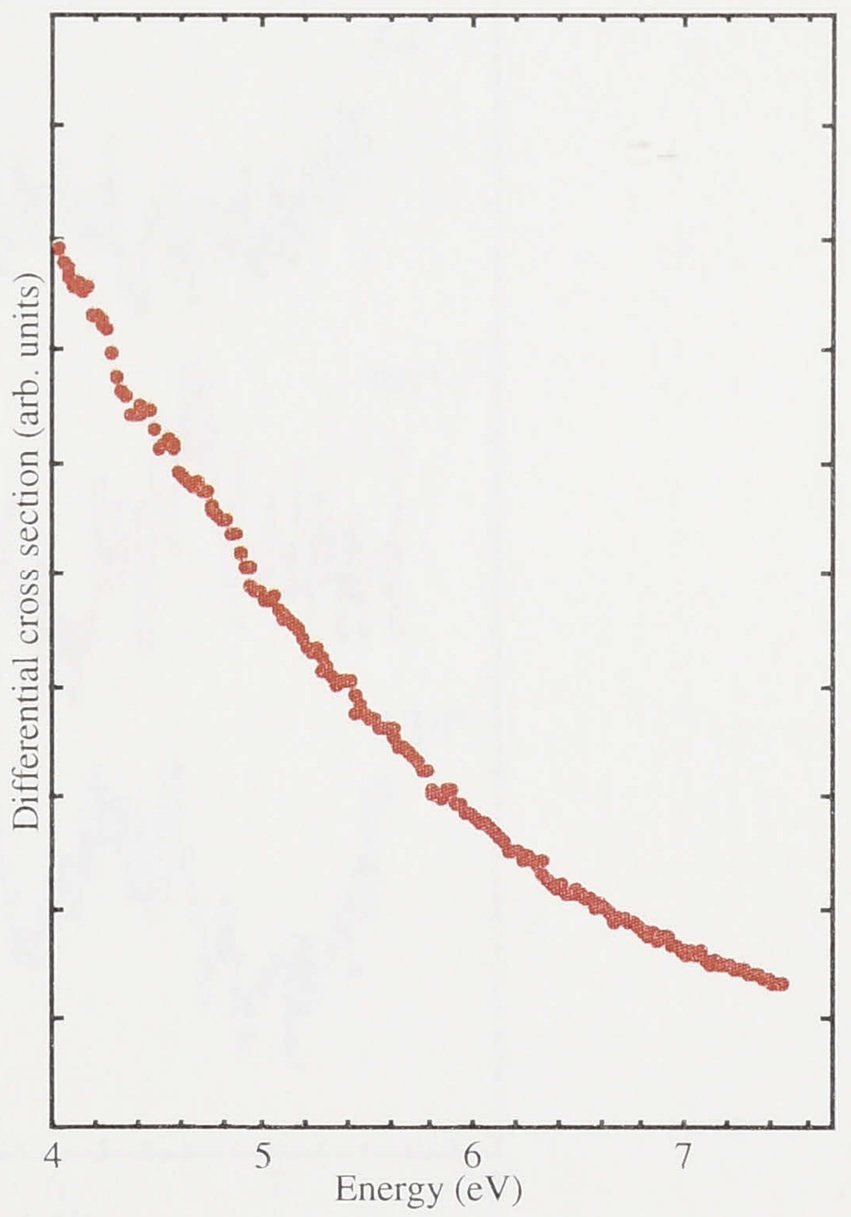

Figure 5.7: Elastic electron scattering from magnesium at 54 degrees

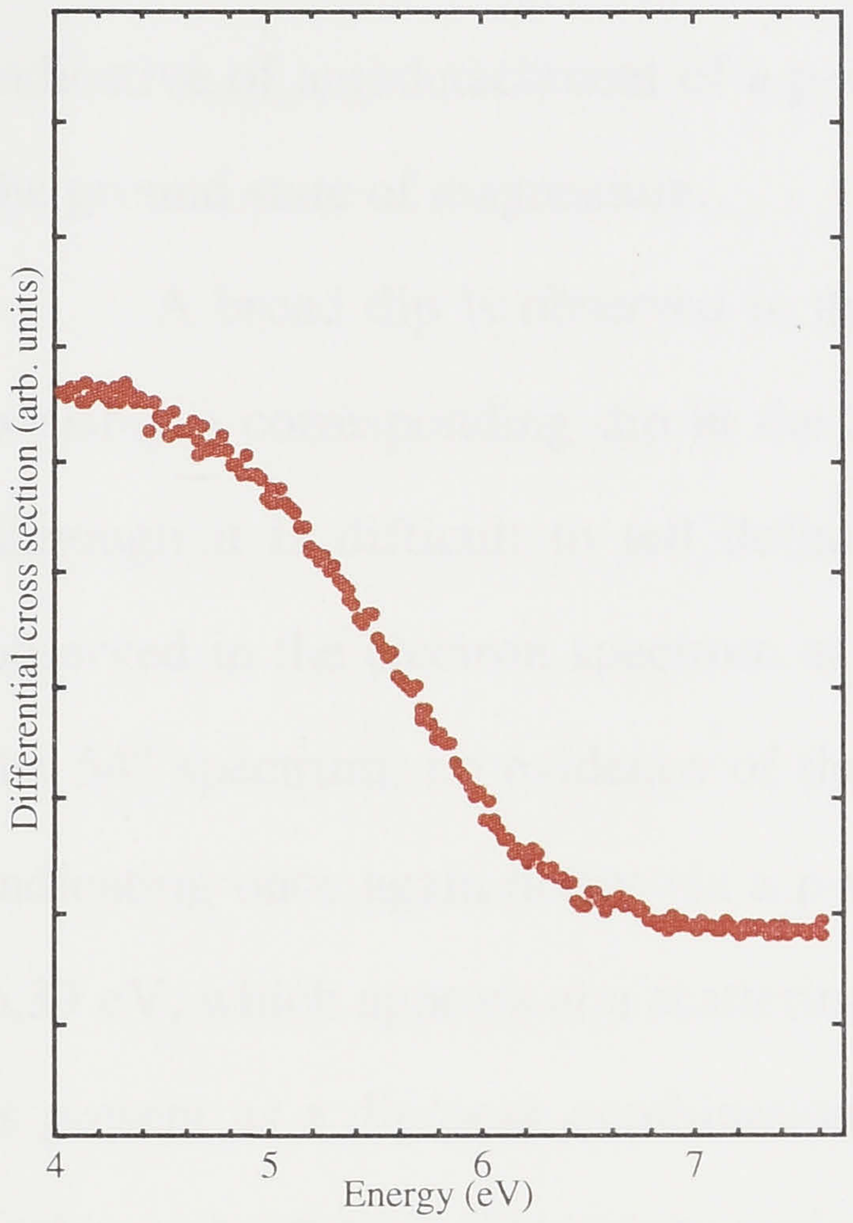

Figure 5.8: Elastic electron scattering from magnesium at 90 degrees

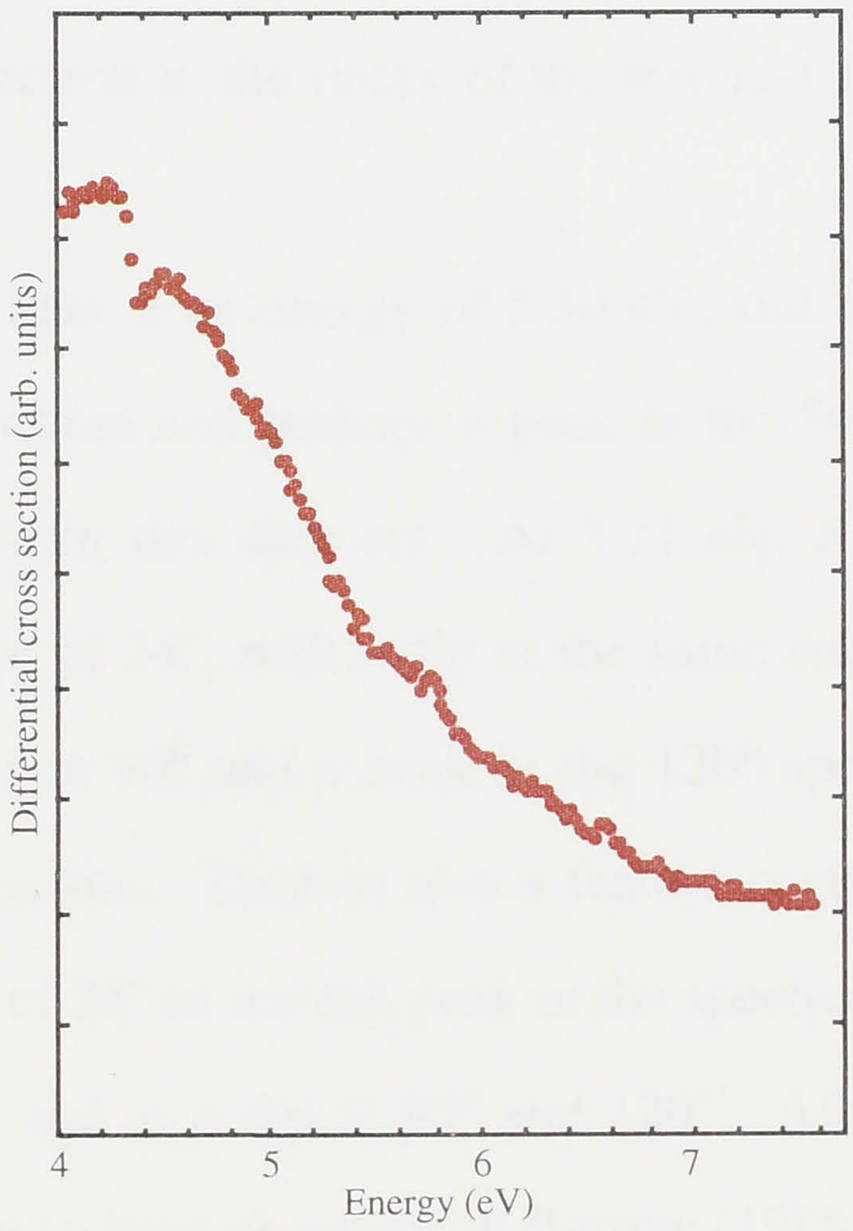

Figure 5.9: Elastic electron scattering from magnesium at 120 degrees

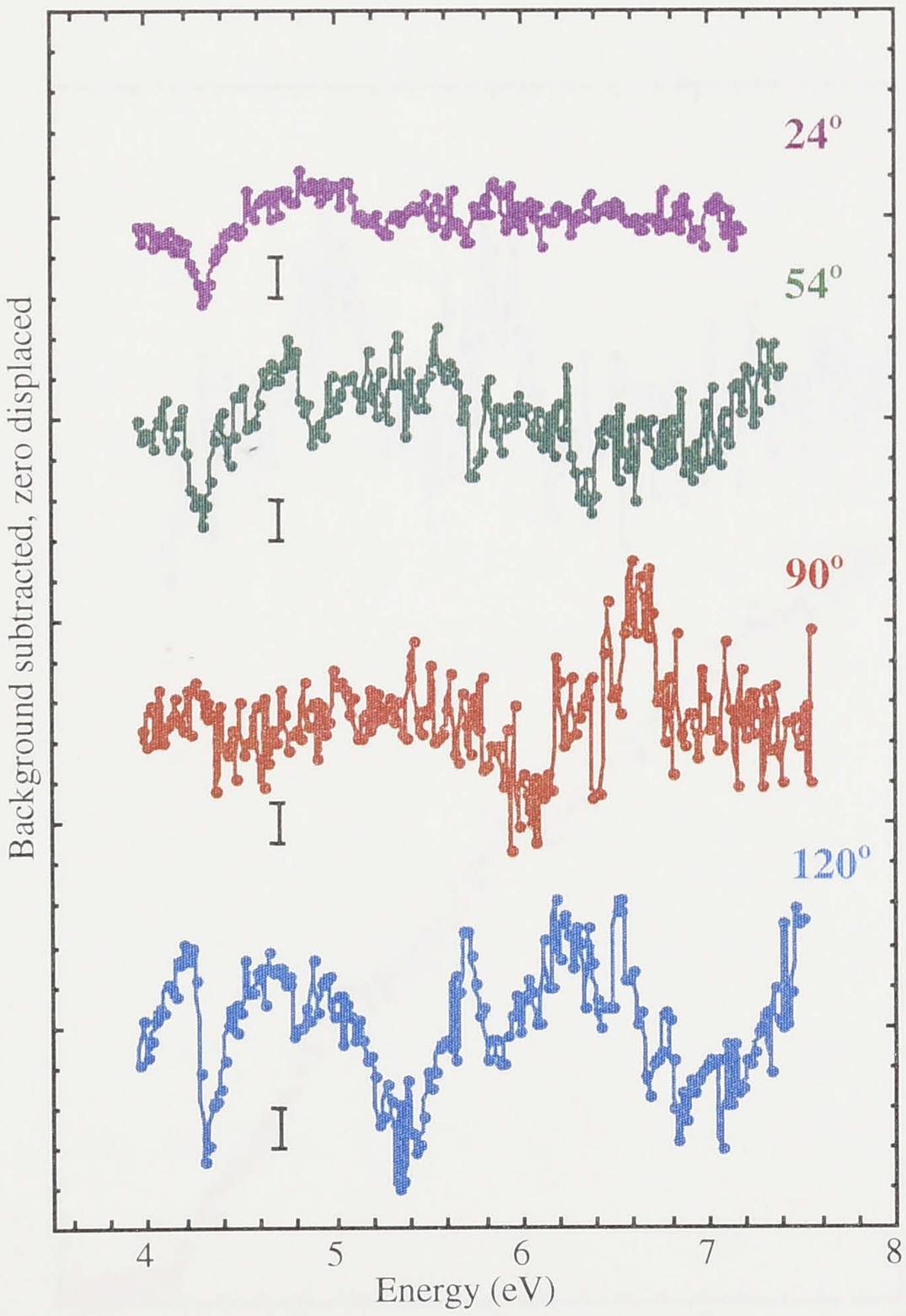

Figure 5.10: Behaviour of resonances in region 2 with scattering angle. The data has had a smoothly varying background subtracted and the zero has been suppressed at each angle. Bars represent 2% of the total scattered signal.

of 24°, a peak/dip at 54°, it is not present at 90° and appears as a dip at 120°. This is indicative of autodetachment of a p-wave electron in the decay of the resonant state to the ground state of magnesium.

A broad dip is observed in the 120° data at an energy of 5.30 eV, and there is possibly a corresponding dip in the 24° spectrum and perhaps a peak in the 54° data, although it is difficult to tell definitively from this data set. At 5.71 eV, a dip is observed in the electron spectrum at an angle of 24°, with a dip at the same energy in the 54° spectrum, no evidence of the feature at 90° and a peak in the 120° spectrum, indicating once again decay via a p-wave electron. There is also a feature occuring at 6.39 eV, which appears at a scattering angle of 24° as a weak peak in the spectrum, and is present as a dip/peak combination at 54° and as a dip at 90° and 120°. All of the features observed in this energy region have also been observed by Burrow (1998) at the same energies in his electron transmission experiments.

Figure 5.11 shows the 3p $^1P_1$ decay photon spectrum, and it can be seen that there is a sharp onset to the spectrum, with a step-like feature at the threshold energy of

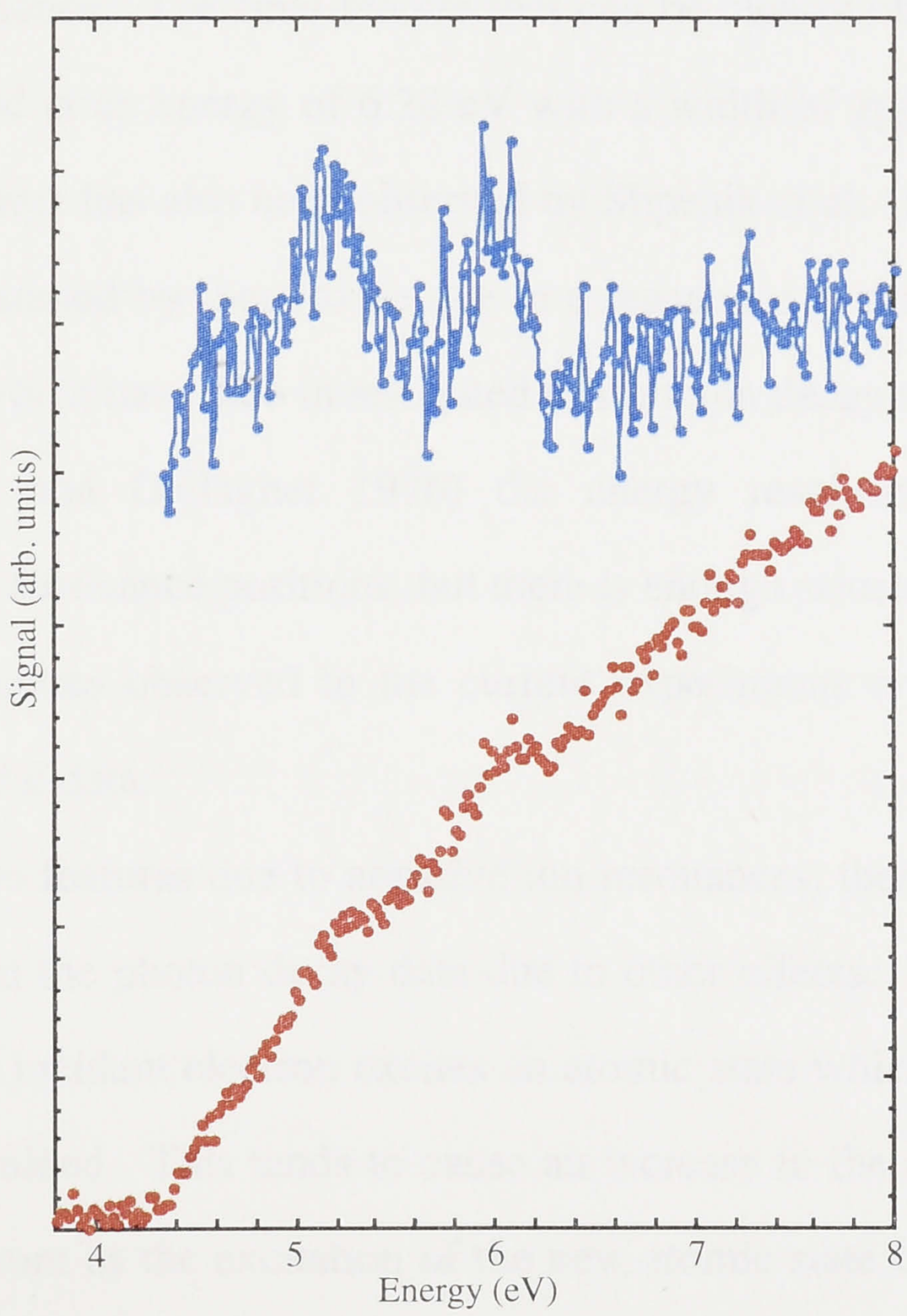

Figure 5.11: Photon decay spectrum for the 3s3p $^1P_1 \rightarrow 3s^2\ ^1S_0$ transition at 285.3 nm in region 2. The red points are the experimental data, the blue points are the scaled, background subtracted data.

4.349 eV. This is indicative of a resonance which may have an energy above or below 4.349 eV but has a width such that it straddles the excitation threshold. This corresponds to the observations in the electron scattering spectra, where a resonance was observed at an energy of 4.30 eV and was broad enough (~100 meV FWHM) that it overlapped the $^1P_1$ state excitation threshold. It is possible that the resonance observed in the elastic scattering channel was made up of more than one term, and that it is only one of the possible terms that is responsible for the feature in the photon excitation function. This will be further discussed in the following chapter. This feature is also apparent in the photon decay data of Shpenik et al. (1979) for the same transition, although it is not attributed to a resonance in that case. The next obvious feature is a change in slope at approximately 5.20 eV, with another change in slope at an energy of 5.50 eV, although the second change appears as a broad dip in the background subtracted data, and may be due to a resonance. The feature at 5.2 eV is observed in the data of Shpenik et al. (1979) and is attributed to a resonance in their analysis. There also appears to be a change in slope at 5.5 eV in their data, which has not been attributed to a resonance. The final feature that can be clearly observed in the present data is a dip, centred at an energy of 6.28 eV with a width of approximately 100 meV (FWHM). This feature has also been observed by Shpenik et al. (1979), at an energy of 6.3 eV, and was assumed by them to be due to a resonance at this energy. In the two other experiments which have also investigated this photon decay transition (Aleksakhin et al. 1973, Leep and Gallagher 1976) the energy resolution is insufficient to definitively identify resonance positions, but there is enough structure in these spectra to suggest that the features observed in the current experiments are also present in the previous experimental data.

In addition to features due to negative ion resonances, there is the possibility of structure occuring in the photon decay data due to other effects. The first is a cascade effect, where as the incident electron excites an atomic state which can then decay into the state being examined. This tends to cause an increase in the observed slope of the photon decay spectrum as the excitation of the new atomic state becomes energetically possible. Another possible effect is when the threshold for excitation of a new state is

passed and causes a reduction in the slope of the photon decay spectrum as a new scattering channel is opened. These effects will be taken into account where appropriate in the analysis presented in the following chapter.

5.2 Cadmium

5.2.1 Background

In electron scattering experiments on cadmium, elastic electron distributions together with results from two different photon decay channels were examined. The photon decay channels were the $5s5p\ ^3P_1 \rightarrow 5s^2\ ^1S_0$ (ground state), which takes place at 326.1 nm, and decay from the $5s5p\ ^1P_1 \rightarrow 5s^2\ ^1S_0$ occurring at 228.8 nm. Attempts were made to examine other decay channels, but it was found that the transitions were too weak to be able to be detected with the current experimental arrangement. This was probably due to the relatively low quantum efficiency of the photomultiplier tubes (approximately 12%) which, when combined with the transmission of the interference filters, gives an overall efficiency estimated at less than 5%. Some other photon decay transitions have been studied in the past, particularly by Zapesochnyi et al. (1973) and Shpenik et al. (1973), using an experimental system consisting of an electron beam (broader and with a much higher current than in the present experiments) incident on a gas cell, with photons detected by a monochromator combined with a photomultiplier tube. In these cases, the detection efficiency is much higher than is attainable in the present experiments.

There are very few electron scattering experiments in which resonances have been observed in cadmium. In addition to the above experiments, Burrow et al. (1976) observed a number resonances in their electron transmission experiments, and Bartsch et al. (1992) also observed a resonance occuring at 4 eV in their measurements of spin asymmetries in electron scattering fom cadmium. This same feature is also present in the experiments of Panajotovic et al. (1994), although it appears at a significantly lower energy. No energy calibration was performed for these latter measurements, and this feature is most likely the same resonance as that appearing at 4 eV in the previously mentioned experiments. Burrow (1998) has performed experiments similar to those in

the previous work by Burrow et al., but with an improved energy resolution and larger energy range, and has observed a significantly larger number of resonances than seen in the previous data. However, little analysis has been performed on any of the previous experimental data, with no classifications proposed for any but the lowest resonance in cadmium.

Few theoretical calculations have been carried out for resonance formation in cadmium. Sin Fai Lam (1981) and Zollweg (1968) have calculated the position of a low lying shape resonance that has been observed by Burrow (1976) at 0.33 eV, but these calculations lie below the energy region for the experiments presented here. Bartschat (1998) has performed R-matrix calculations on resonances in electron scattering and photon excitation functions for the energy regions examined here, and the experimental data has been compared to this theory where possible.

In the current measurements, the electron scattering data was taken in three energy regions, and the resonance structure in these regions will be presented separately. These regions are from 3.0 to 5.0 eV incident electron energy, 5.0 to 8.99 eV and 10.5 to 13.5 eV. The main reason for the separation into different regions is due to the variation of the elastic electron scattering cross section of cadmium with both angle and energy. As both incident electron energy and scattering angle increase, the cross section for elastic electron scattering from cadmium decreases significantly. Measurements by Marinkovic et al. (1991) show that at 3.4 eV the elastic scattering cross section drops by more than an order of magnitude over the angular range investigated (20^{o} to 150^{o}). As the energy increases to 6.4 eV and then 10 eV, this decrease is even more pronounced so that there is 3 orders of magnitude difference between the 10 eV elastic scattering cross section at 20^{o} and 90^{o}. In addition to this, the magnitude of the cross section at 10 eV is substantially smaller than that at 3.4 eV at all scattering angles. This observation has also been borne out by the calculations of McEachran and Stauffer (1992) and McEachran (1997). As a result of this, to perform the current experiments it was necessary to run the apparatus for long periods of time, requiring very good stability. Separating the experiment into three energy regions ensured that the resonance features in each region could be comprehensively examined, with a minimum of intervention in

the running of the experiment. The energy regions themselves are not continuous, with a gap of approximately 1.5 eV between the second and third regions. This was decided upon after examination of the electron transmission data of Burrow (1998), which is highly sensitive to negative ion resonances. In this data, there is no evidence of resonance features between 9.0 and 10.5 eV (the region just above the ionisation potential), and to optimise the efficiency of data collection in the current series of experiments, it was decided that it was unnecessary to examine this region in detail.

5.2.2 Region 1: 3.0 eV to 5.0 eV

In this energy region, two features are apparent in the electron scattering data, straddling the position of the 5s5p $^3P_{0,1,2}$ energy levels of neutral cadmium which occur at energies of 3.737 eV, 3.804 eV and 3.949 eV (Moore 1971). The first feature occurs at an energy of 3.60 eV with an energy width of approximately 90 meV (FWHM), and appears as a peak at scattering angles of 24° (figure 5.12), 90° (weakly, figure 5.14) and 120° (figure 5.15) with no evidence of the resonance feature at 54° (figure 5.13). The second feature is considerably broader and is centred at 4.08 eV with a width of ~220 meV. At 24° it appears as a peak, with a very weak peak present at 54°, a peak-dip appearance at 90° and a peak again at a scattering angle of 120°. Figure 5.16 summarises this variation with scattering angle, and gives an estimate of the ratio of resonant to direct scattering. The larger feature, centred at 4.08 eV, appears to be due to the same resonance observed at 4.0 eV in the experiments of Burrow et al. (1976), Burrow (1998) and Barstch et al. (1992), and at 3.23 eV by Panajotovic et al. (1994). Only in the case of Burrow (1998) is there evidence of the lower energy, smaller, feature. This is possibly due to insufficient energy resolution, or insufficient sensitivity to such smaller features in the other experiments. Panajotovic et al. have examined this resonance at three different scattering angles, and have found it to be present at angles of 20°, 120° and 146°, with a width of 310 meV. Although the stated resolution of their experiments is 50 meV, it is probable in this case that the two resonances were not able to be distinguished from each other, leading to the larger measured width.

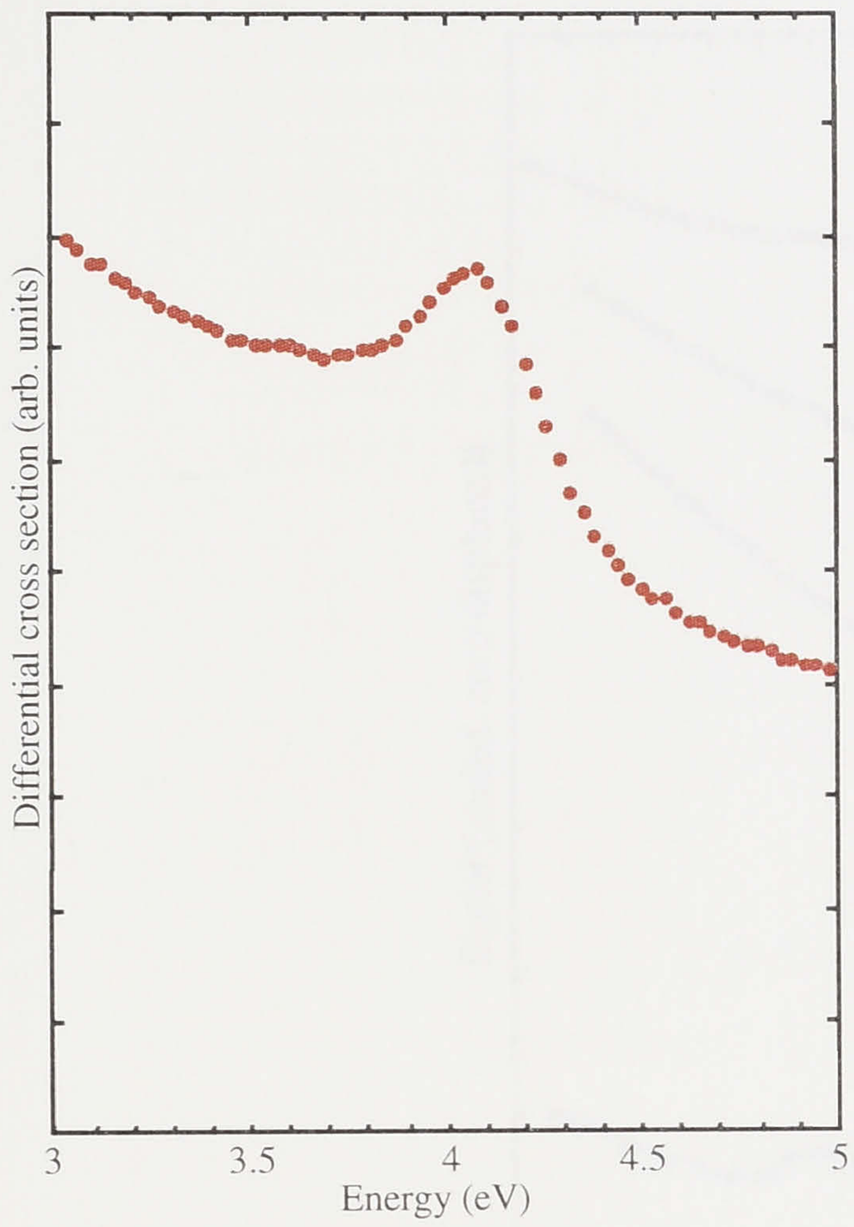

Figure 5.12: Elastic electron scattering from cadmium at 24 degrees

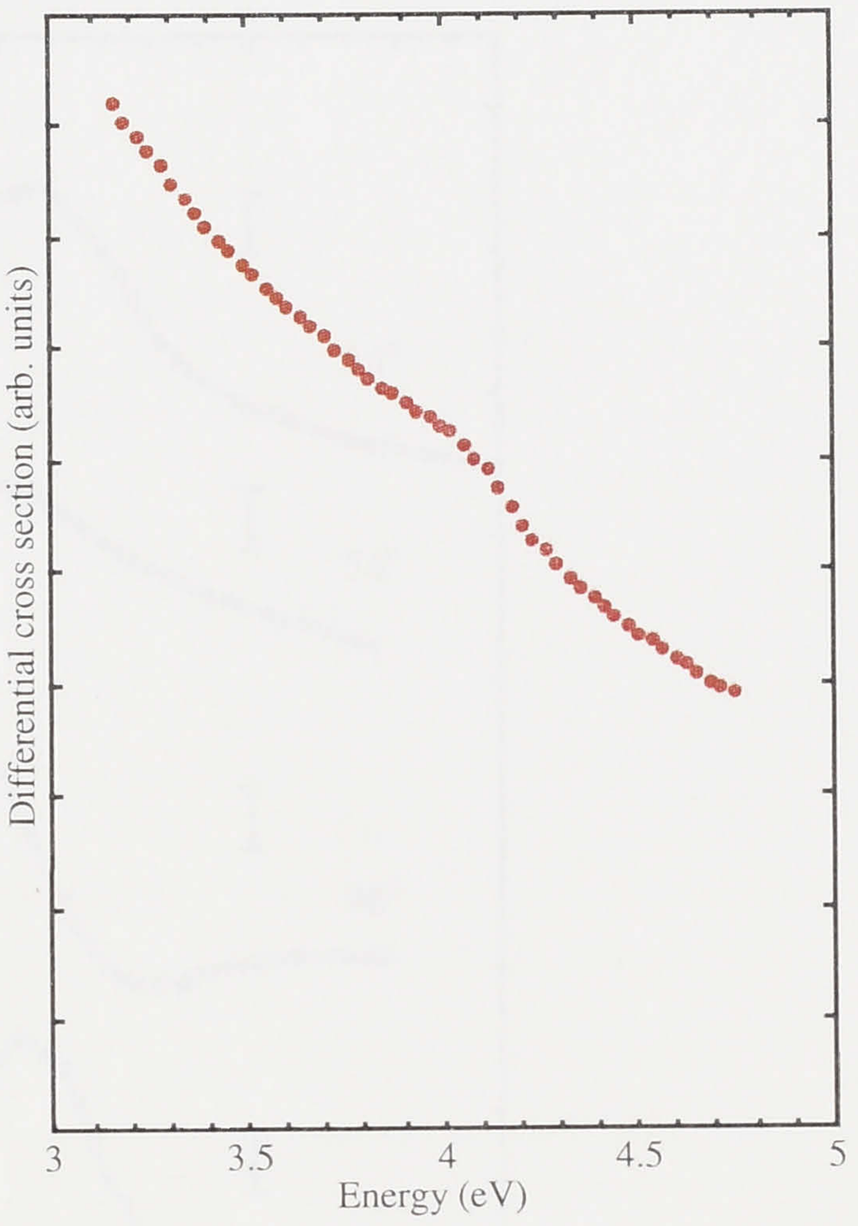

Figure 5.13: Elastic electron scattering from cadmium at 54 degrees

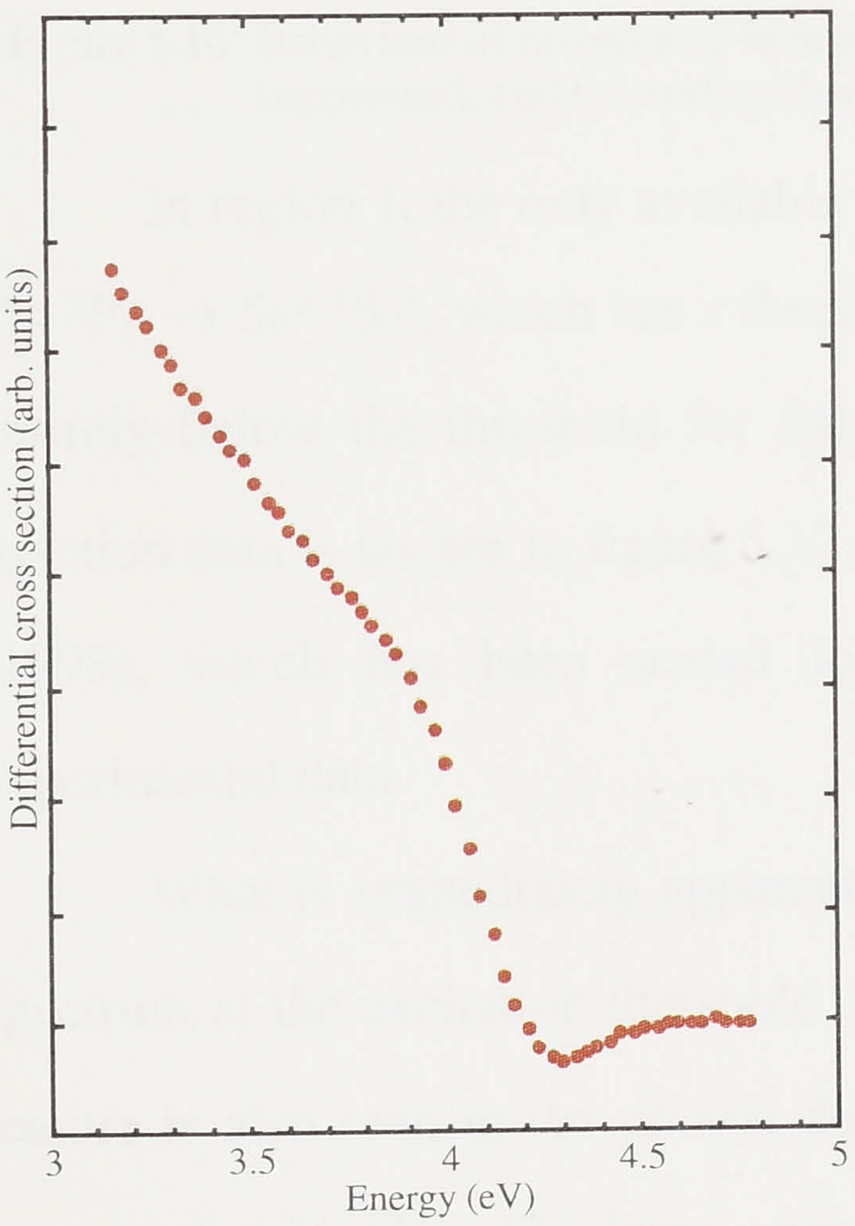

Figure 5.14: Elastic electron scattering from cadmium at 90 degrees

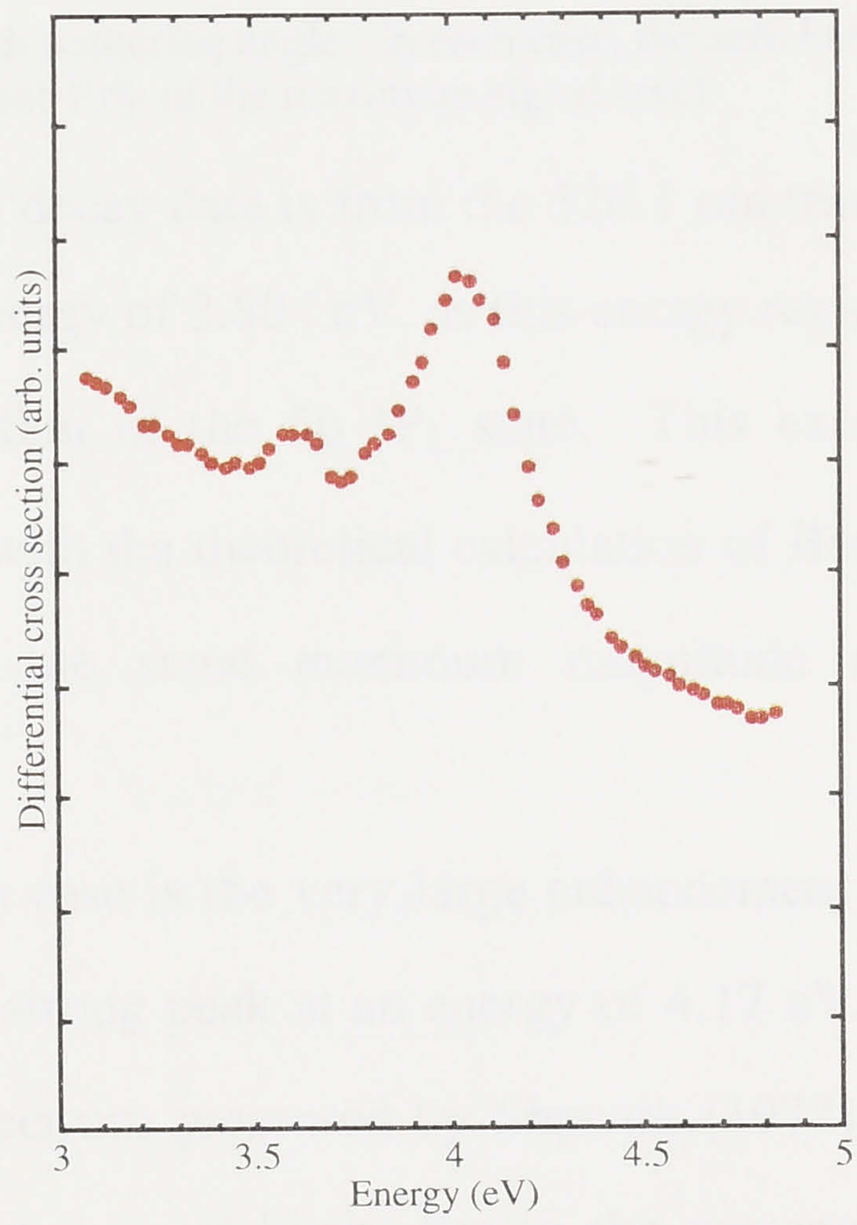

Figure 5.15: Elastic electron scattering from cadmium at 120 degrees

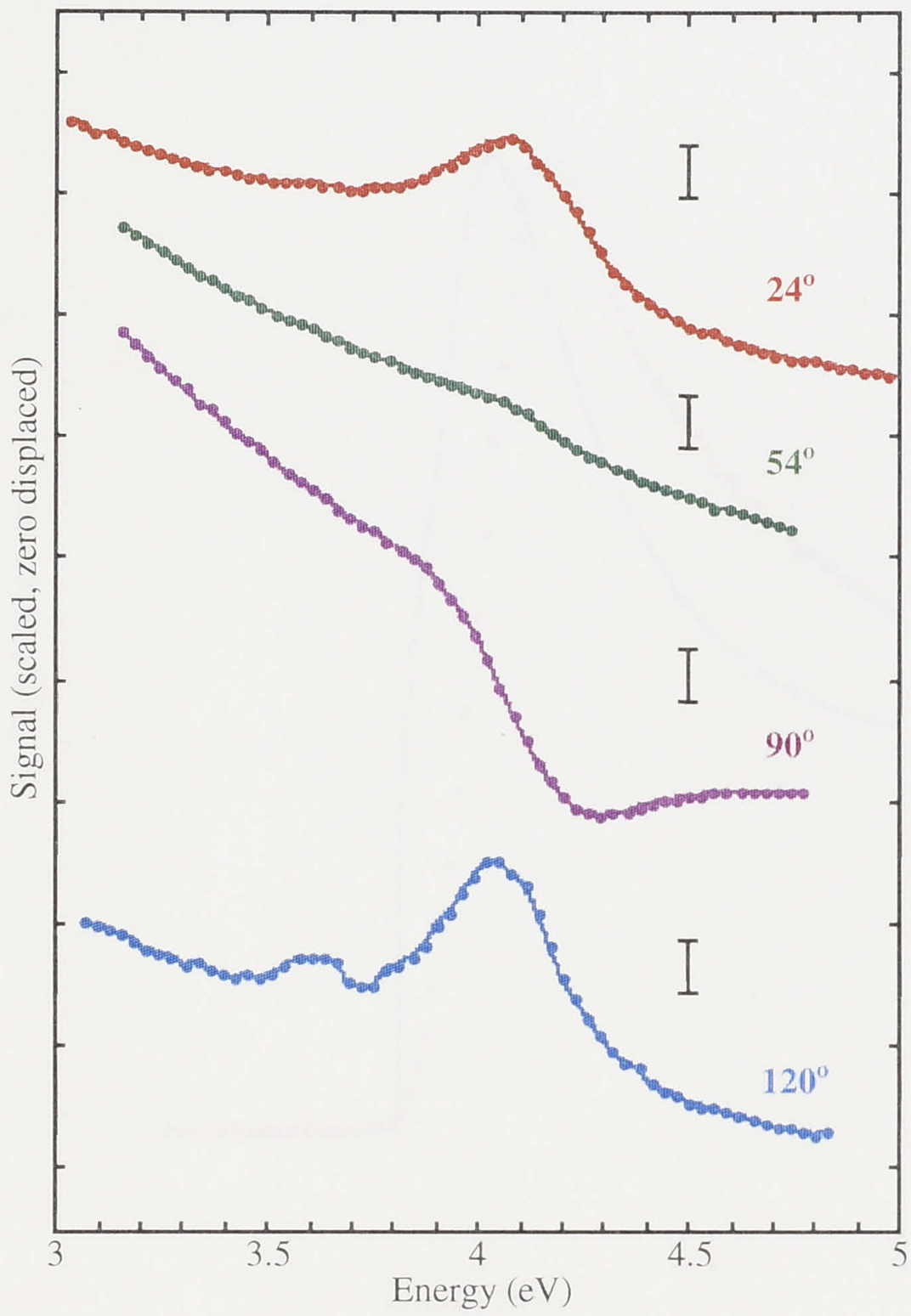

Figure 5.16: Behaviour of resonances in region 1 with scattering angle. In each case, the zero has been suppressed, and the vertical bars represent 10% of the maximum signal level.

In region 1, the only available photon decay data is from the 326.1 nm transition ($5p\ ^3P_1 \rightarrow 5s^2\ ^1S_0$), which has a threshold energy of 3.804 eV, as this energy region lies entirely below the threshold for the excitation of the $5p\ ^1P_1$ state. This excitation function data is shown in figure 5.17 along with the theoretical calculation of Bartschat (1998), which has been scaled to have the same maximum magnitude as the experimental data.

What is immediately apparent in this case is the very large enhancement of the spectrum at the excitation threshold, with a strong peak at an energy of 4.17 eV. This feature is also seen in the photon decay spectrum presented by Shpenik (1973), at an energy of 4.16 eV. The large enhancement is most likely due to the presence of a resonance, and it can be seen in figure 5.17 that this large peak at the $5s5p\ ^3P_1$ photon decay onset is also present in the calculations of Bartschat (1998), although slightly shifted in energy relative to the experimental data, appearing at an energy of 4.02eV, rather than 4.17 eV.

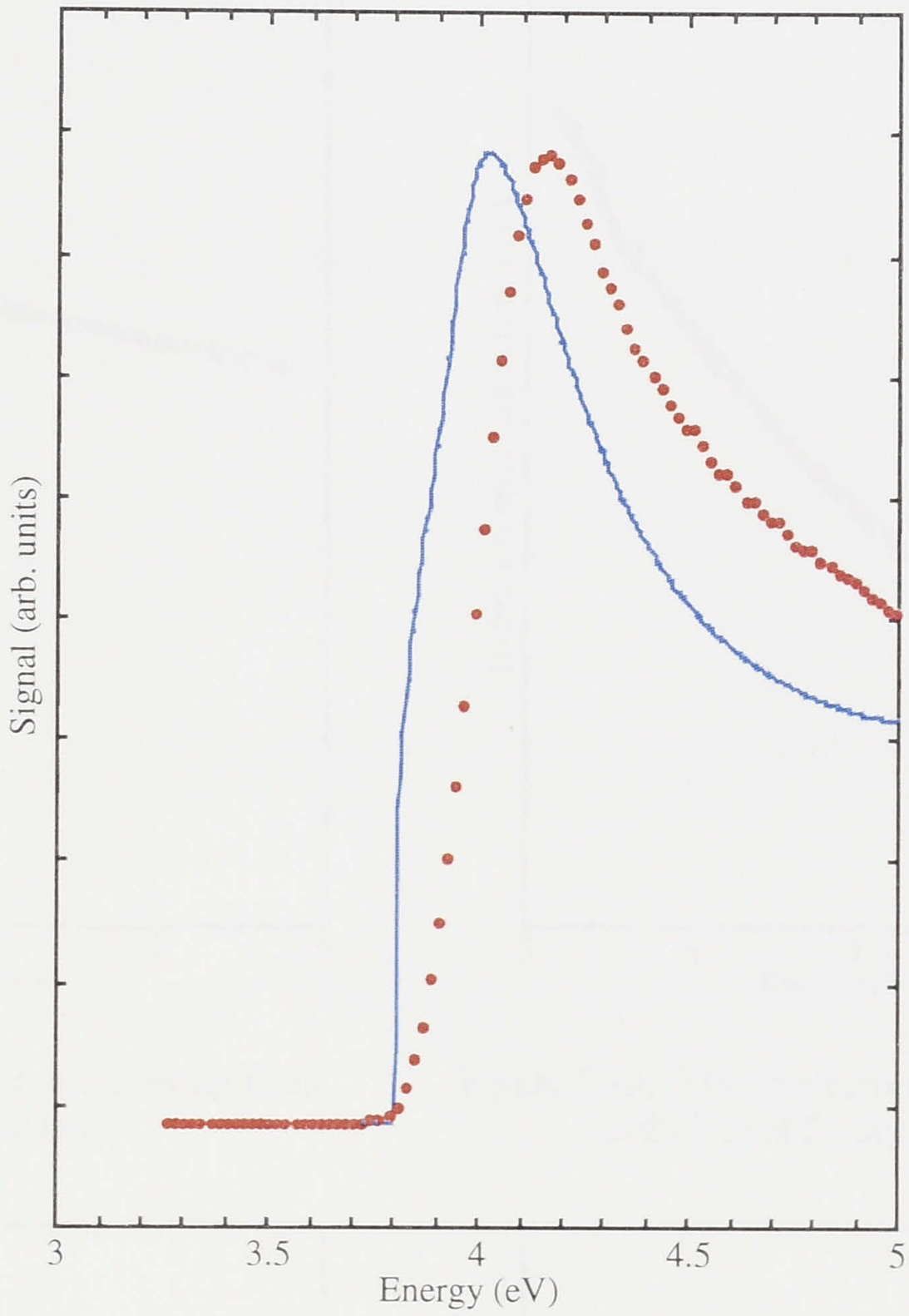

Figure 5.17: Photon decay spectrum for the 5s5p $^3P_1 \rightarrow 5s^2\ ^1S_0$ transition at 326.1 nm in region 1. Red points are the experimental data, blue curve is the calculation of Bartschat (1998).

5.2.3 Region 2 - 5.0 eV to 8.99 eV

The data from the elastic electron scattering experiments presented in this section encompasses the energy region from just below the 5p $^1P_1$ state of neutral cadmium (5.417 eV) to the ionisation potential. They are shown in figures 5.18, 5.19, 5.20 and 5.21, which are for scattering angles of 24°, 54°, 90° and 120° respectively. The resonance features in these figures are substantially weaker than those in the previous section, and are most clearly visible in the background subtracted data. Figure 5.22 displays this background subtracted data, and clearly shows three resonance features, the first at 5.42 eV with a width of approximately 215 meV (FWHM), the next at 6.60 eV with a width of 195 meV and the third at 7.24 eV with a width of 170 meV. Burrow et al. (1976) and Burrow (1998) also see a feature in their electron transmission data at the onset of the 5p $^1P_1$ state of neutral cadmium, at an energy of 5.417 eV, which

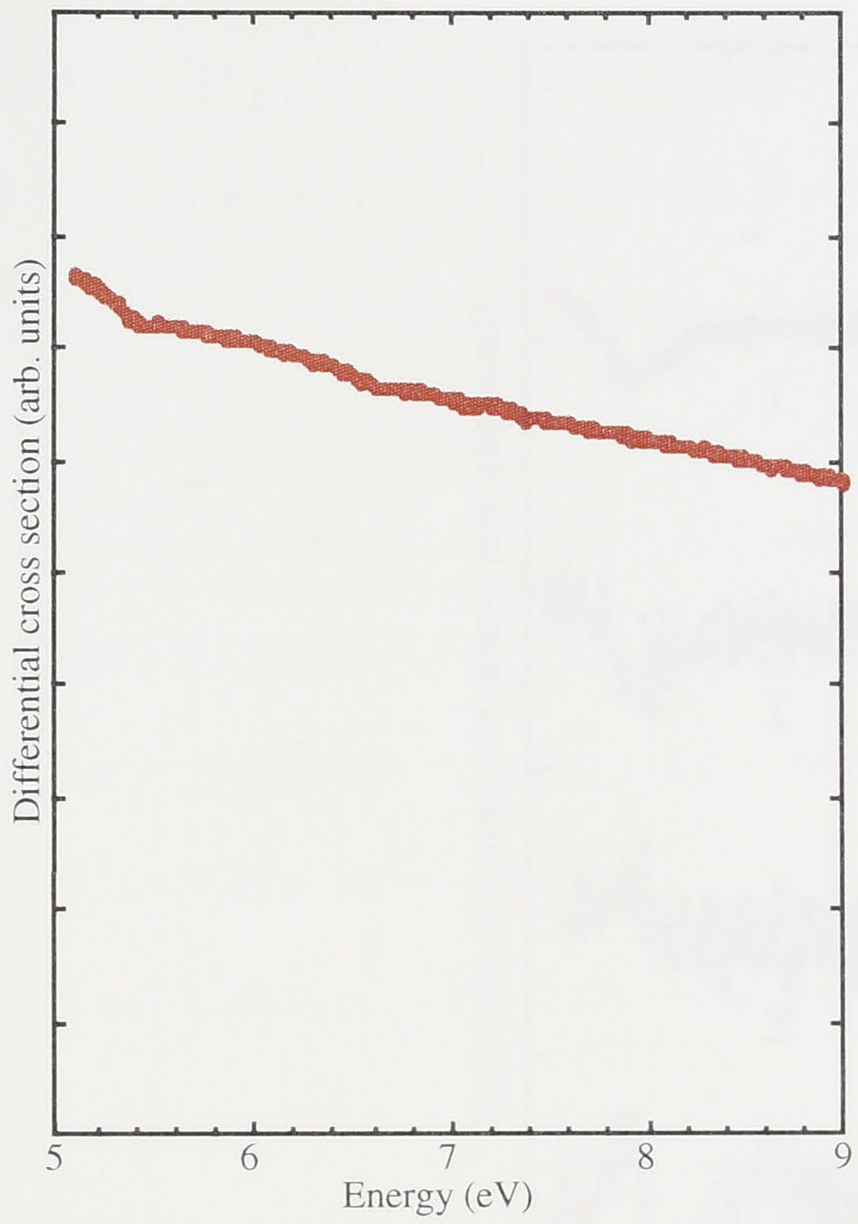

Figure 5.18: Elastic electron scattering from cadmium at 24 degrees

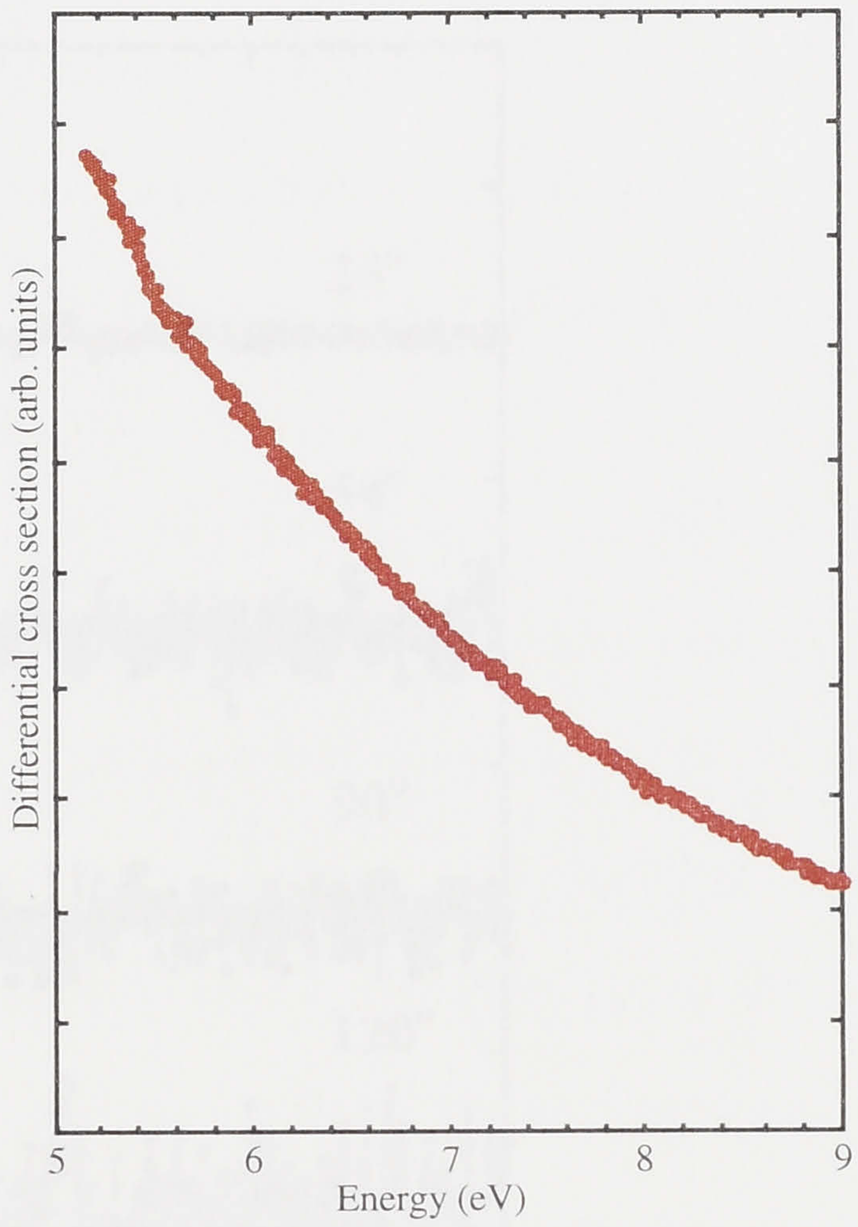

Figure 5.19: Elastic electron scattering from cadmium at 54 degrees

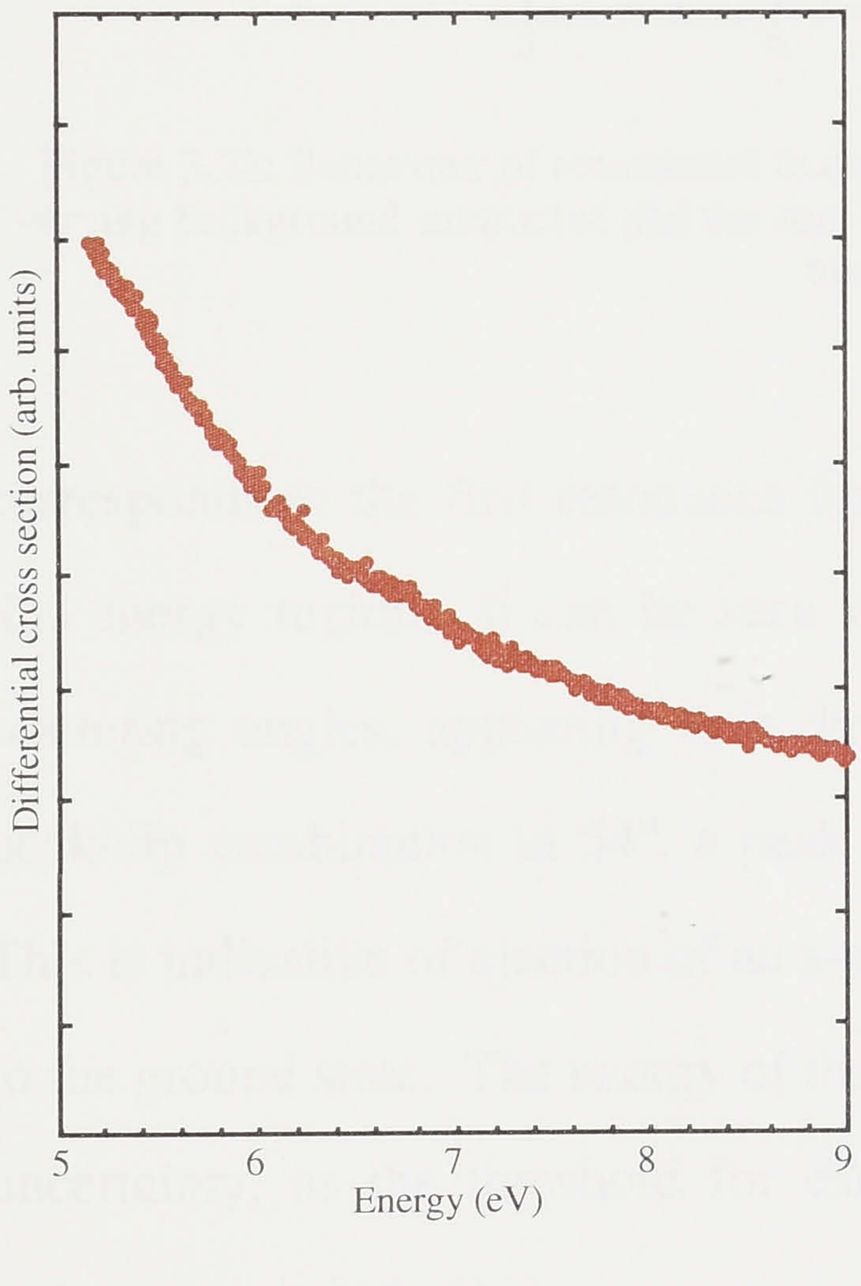

Figure 5.20: Elastic electron scattering from cadmium at 90 degrees

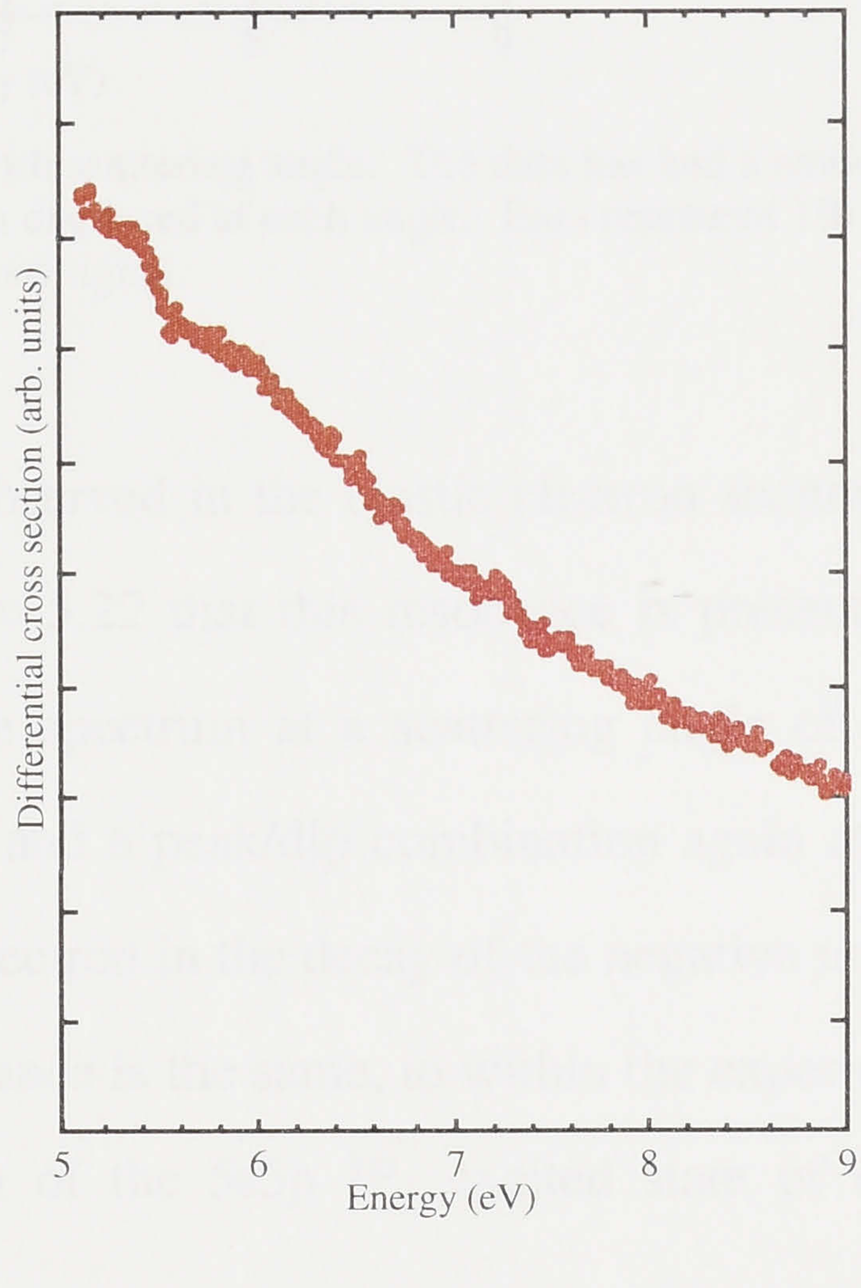

Figure 5.21: Elastic electron scattering from cadmium at 120 degrees

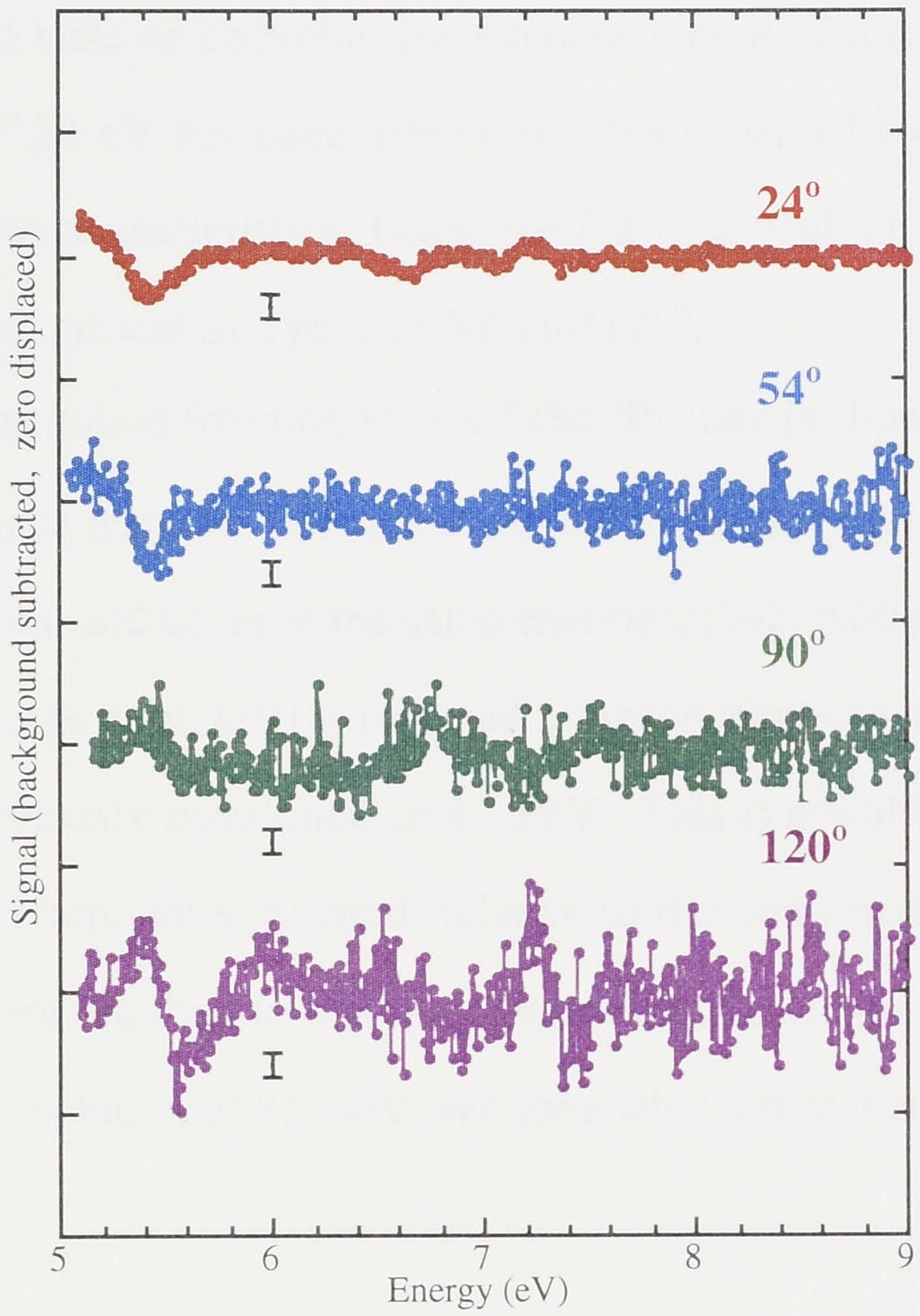

Figure 5.22: Behaviour of resonances in region 2 with scattering angle. The data has had a smoothly varying background subtracted and the zero has been displaced at each angle. Bars represent 1% of the total scattered signal.

corresponds to the first resonance feature observed in the elastic electron scattering in this energy region. It can be seen in figure 5.22 that this resonance is present at all scattering angles, appearing as a dip in the spectrum at a scattering angle of 24°, a peak/dip combination at 54°, a peak at 90° and a peak/dip combination again at 120°. This is indicative of ejection of an s-wave electron in the decay of the negative ion state to the ground state. The energy of the resonance is the same, to within the experimental uncertainty, as the threshold for excitation of the 5s5p $^1P_1$ excited state of neutral cadmium at 5.417 eV.

The resonance at 6.60 eV has also been observed in the experiment of Burrow (1998). In the present experiment it appears as a dip at a scattering angle of 24°, it is not present in the cross section at 54°, appears as a peak at 90°, and it is weakly present as a dip in the cross section at 120°. However, its presence at this largest angle is difficult to definitively ascertain, due to the small scattering cross section. Nevertheless, the

behaviour of this resonance feature as a function of scattering angle indicates that it decays to the ground state of cadmium by autodetachment of a d-wave electron. The feature observed at 7.24 eV has once more also been observed by Burrow (1998) and again displays d-wave characteristics, being present as a peak at a scattering angle of 24°, absent at 54°, and present as a peak at 90° and 120°.

The optical excitation function for the 5s5p $^3P_1$ state is shown in figure 5.23, and exhibits three resonance features. These correspond to the three features observed in the electron scattering data, and occur at the same energies, 5.42, 6.60 and 7.25 eV. For the same transition, Shpenik et al. (1973) reported no resonances other than the large near-threshold feature previously mentioned, at 4.16 eV. This is possibly due to the fact that the features observed here are very small relative to the non-resonant background, and long counting times are required to obtain sufficient data to see the features. In addition to this, their energy resolution of 80 meV was somewhat larger than that of the present

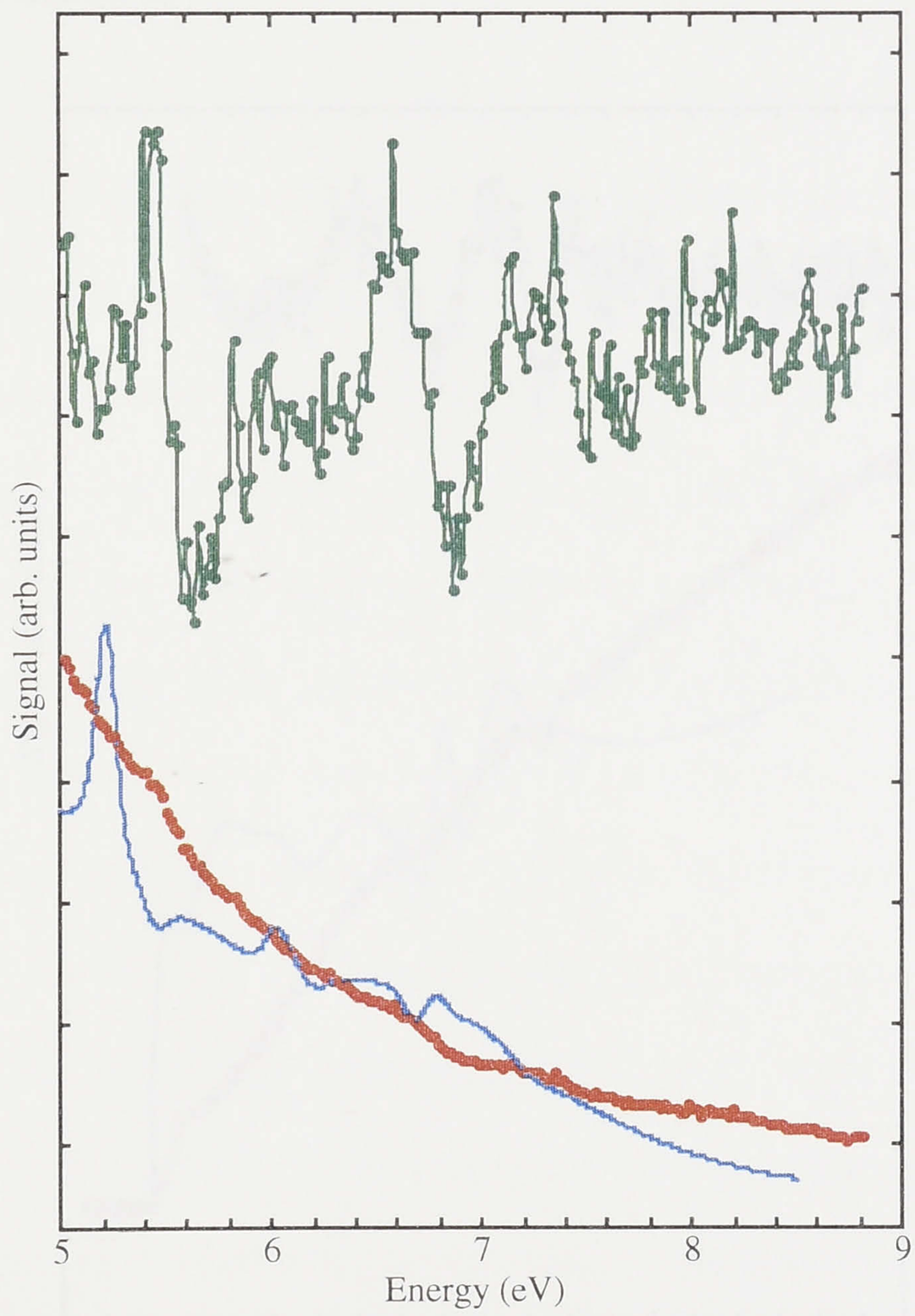

Figure 5.23: Photon decay spectrum for the 5s5p $^3P_1 \rightarrow 5s^2\ ^1S_0$ transition at 326.1 nm in region 2. The red points are the experimental data, the blue curve is the calculation of Bartschat (1998) and the green points are the scaled, background subtracted experimental data.

experiments and may also have contributed to lack of observation of the smaller resonances presented here. The resonance at 5.42 eV appears as a peak-dip in the spectrum, and can be seen to be straddling the 5s5p $^1P_1$ excitation threshold, as is the case in the elastic scattering spectrum. The resonance at 6.60 eV also appears as a peak in the photon decay spectrum, as does the resonance at 7.24 eV. It is possible to compare this spectrum with the photon decay calculations of Bartschat (1998), also shown in figure 5.23 and normalised as previously. Qualitatively there is reasonable agreement between theory and experiment, although there are some differences in the positions and magnitude of the resonances. A peak corresponding to the resonance observed at 5.42 eV is seen at an energy of 5.22 eV in the theoretical calculation. Several other features can be seen in the theoretical curve which may correspond to the other two features observed in the experiment, although they are again shifted in energy with respect to the experimental observations, and it is difficult to make a meaningful comparison between the two.

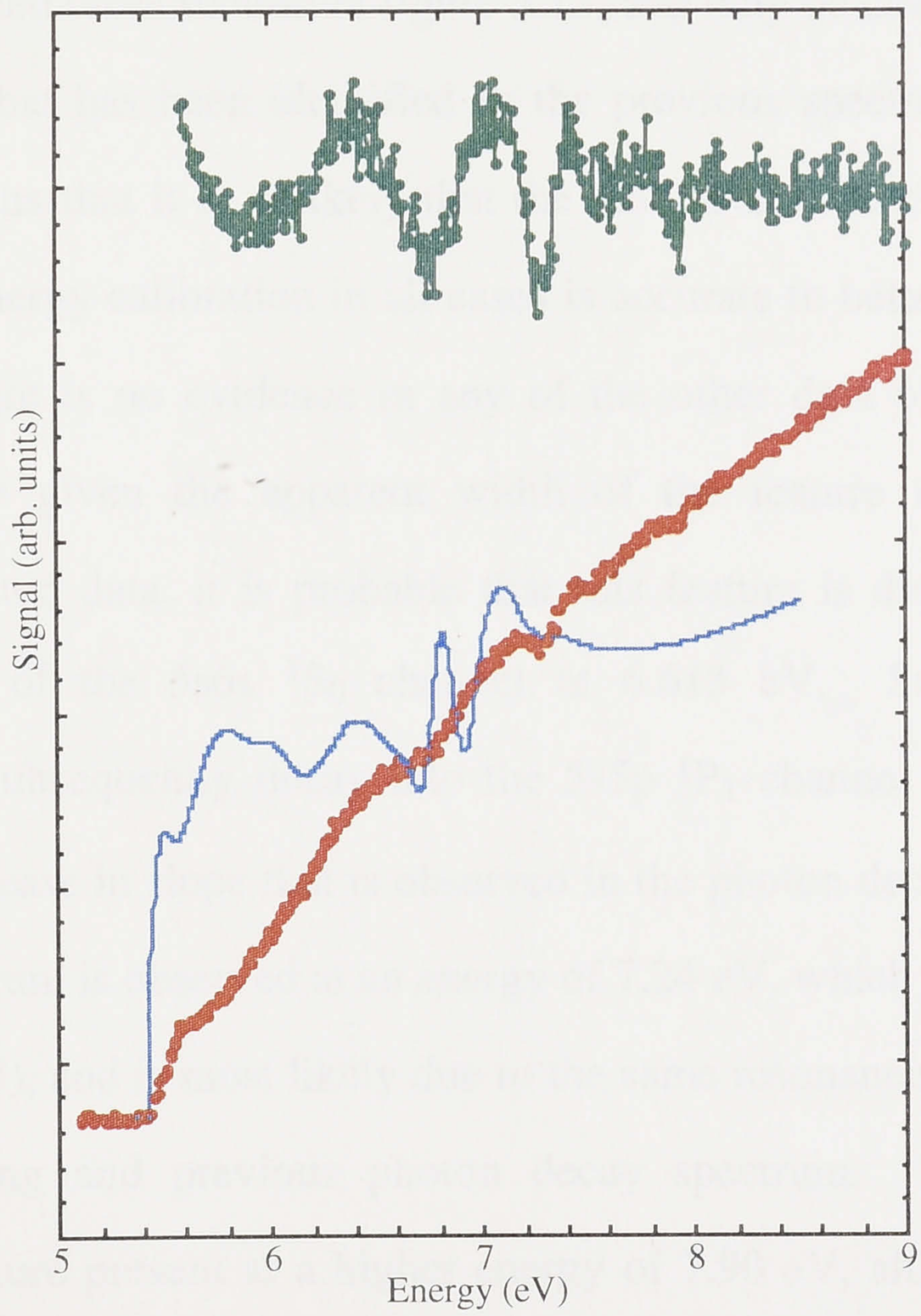

Figure 5.24: Photon decay spectrum for the 5s5p $^1P_1 \rightarrow 5s^2\ ^1S_0$ transition at 228.8 nm in region 2. The red points are the experimental data, the blue curve is the calculation of Bartschat (1998) and the green points are the scaled, background subtracted experimental data.

Data is also available in this energy region from the second photon decay channel, the 5s5p $^1P_1 \rightarrow 5s^2\ ^1S_0$ transition at 228.8 nm, and this is displayed in figure 5.24. It is qualitatively very similar to the analagous transition in magnesium, the 3s3p $^3P_1 \rightarrow 3s^2\ ^1S_0$ transition. In this data a sharp, step-like rise is also seen at the onset of the photon decay channel. Although much smaller in magnitude than the similar effect observed in the excitation function of the $^3P_1$ state, this effect is also due to the presence of a resonance near the threshold of the excited state. This effect can also be clearly seen in the excitation function for this state measured by Shpenik et al. (1973), but is not attributed by them to a resonance. At 6.41 eV, there is a change in slope in the excitation function, and this is probably due to the opening of a new excitation channel, possibly the 5s6s $^3S_1$ state which has a threshold energy of 6.388 eV. It is possible that as this threshold is passed, there is a loss of flux to the 5s5p $^1P_1$ state, resulting in the reduction in slope occuring around this energy. Another possible change in slope occurs at approximately 6.70 eV, although it appears as a dip in the background subtracted cross section in figure 5.13, and may be due to a resonance. The nearest resonance that has been identified in the previous spectra is the resonance at 6.60 eV. This means that it is unlikely that the feature at 6.70 eV is due to the same resonance, as the energy calibration in all cases is accurate to better than 100 meV (see chapter 3). As there is no evidence in any of the other data of a resonance at this energy, particularly given the apparent width of the feature as it appears in the background subtracted data, it is probable that this feature is due to a cascade effect from the opening of the 5s6s $^1S_0$ channel at 6.615 eV. States excited to this configuration can subsequently decay into the 5s5p $^1P_1$ channel by photon emission, resulting in the increase in slope that is observed in the photon decay data. A dip in the photon decay spectrum is observed at an energy of 7.24 eV, which was also observed by Shpenik et al. (1973), and is most likely due to the same resonance that was observed in the elastic scattering and previous photon decay spectrum. There is the further possibility of a feature present at a higher energy of 7.90 eV, although it is only very weakly apparent, even in the background subtracted data of figure 5.24. Interestingly, a similar feature is observed at 7.95 eV in the data of Shpenik et al.

5.2.4 Region 3: 10.5 eV to 13.5 eV

This energy region lies above the ionisation potential for cadmium, and ecompasses the thresholds for 3 autoionising states of neutral cadmium, the $4d^9 5s^2 (^2D_{5/2}) 5p\ ^1P_1$, $4d^9 5s^2 (^2D_{3/2}) 5p\ ^3P_1$ and $4d^9 5s^2\ (^2D_{3/2}) 5p\ ^3D_1$ states at energies of 12.122 eV, 12.819 eV and 12.934 eV respectively (Moore, 1971). These doubly excited states of neutral cadmium have been the subject of extensive experimental investigation in electron scattering experiments (see Martin and Thompson 1991, Martin et al. 1994 and references therein, for example) and the resonances in this region will be associated with them. The data from the elastic electron scattering experiments in this region show the presence of several resonances, with four prominent peaks in evidence. The data at individual angles is shown in figures 5.25 (24^o), 5.26 (54^o), 5.27 (90^o) and 5.28 (120^o), with the background subtracted data summarised in figure 5.29. The four features are centred at energies of 11.43, 11.64, 11.88 and 12.20 eV with widths of approximately 160 meV, 110 meV, 120 meV and 270 meV respectively. At a scattering angle of 54^o, there is no evidence of any of the resonance structures, and they are present again at 90 and 120^o. This is indicative of the ejection of a d-wave electron in the decay of these states to the ground state.

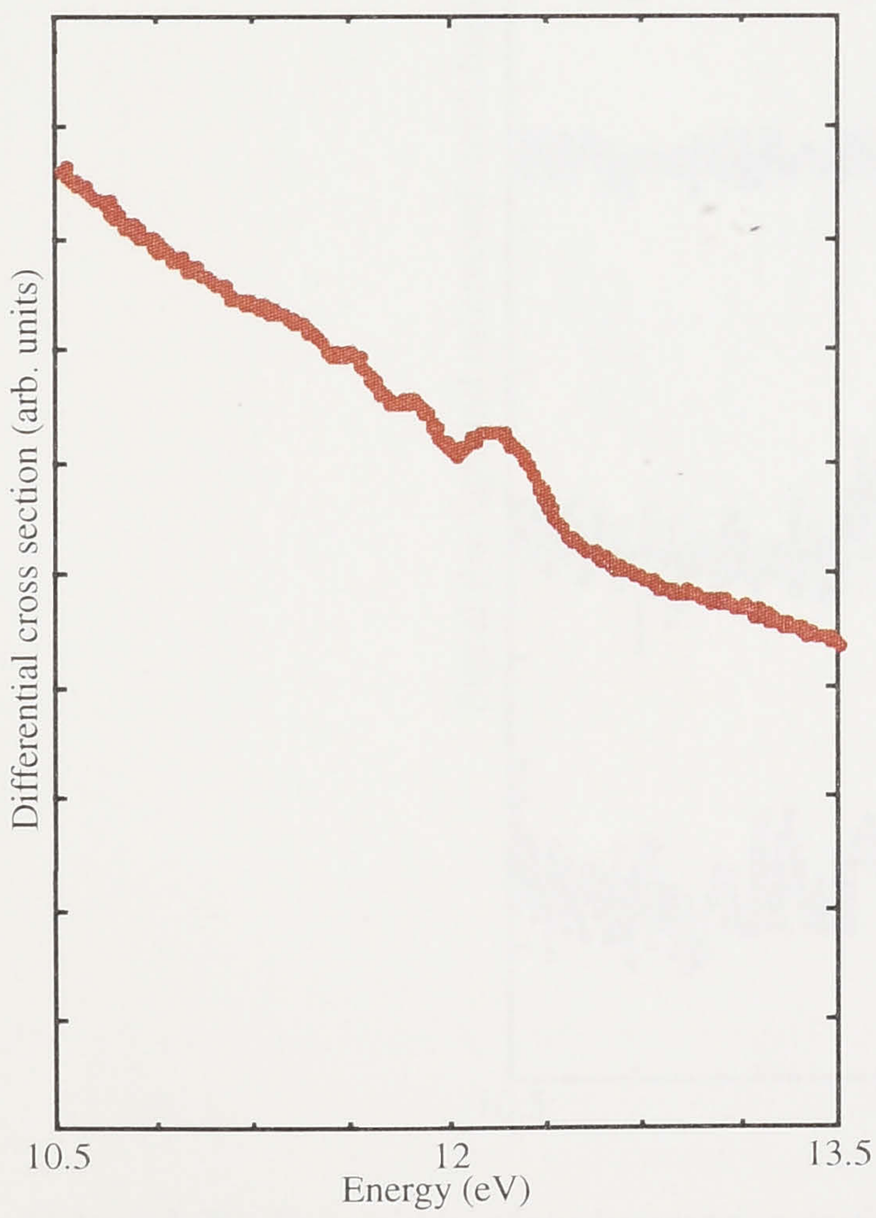

Figure 5.25: Elastic electron scattering from cadmium at 24 degrees

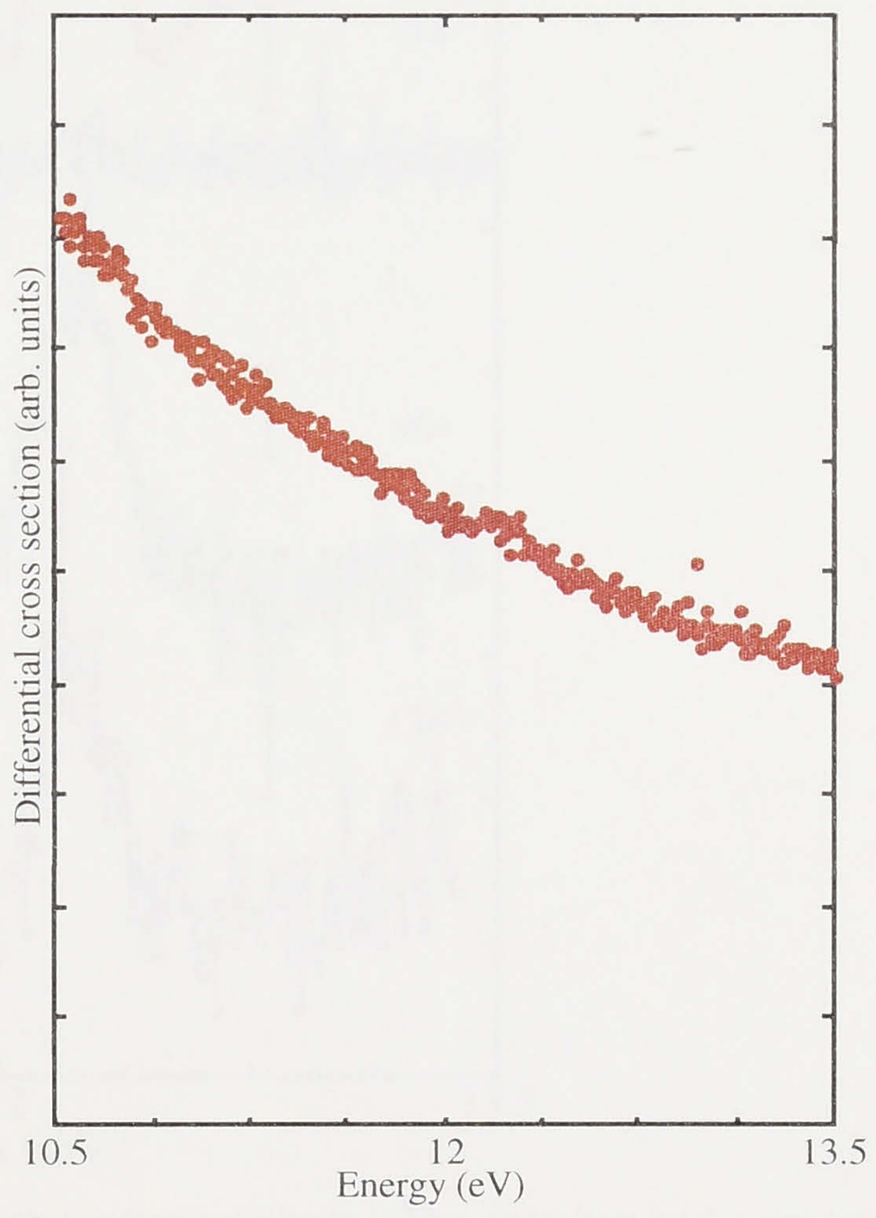

Figure 5.26: Elastic electron scattering from cadmium at 54 degrees

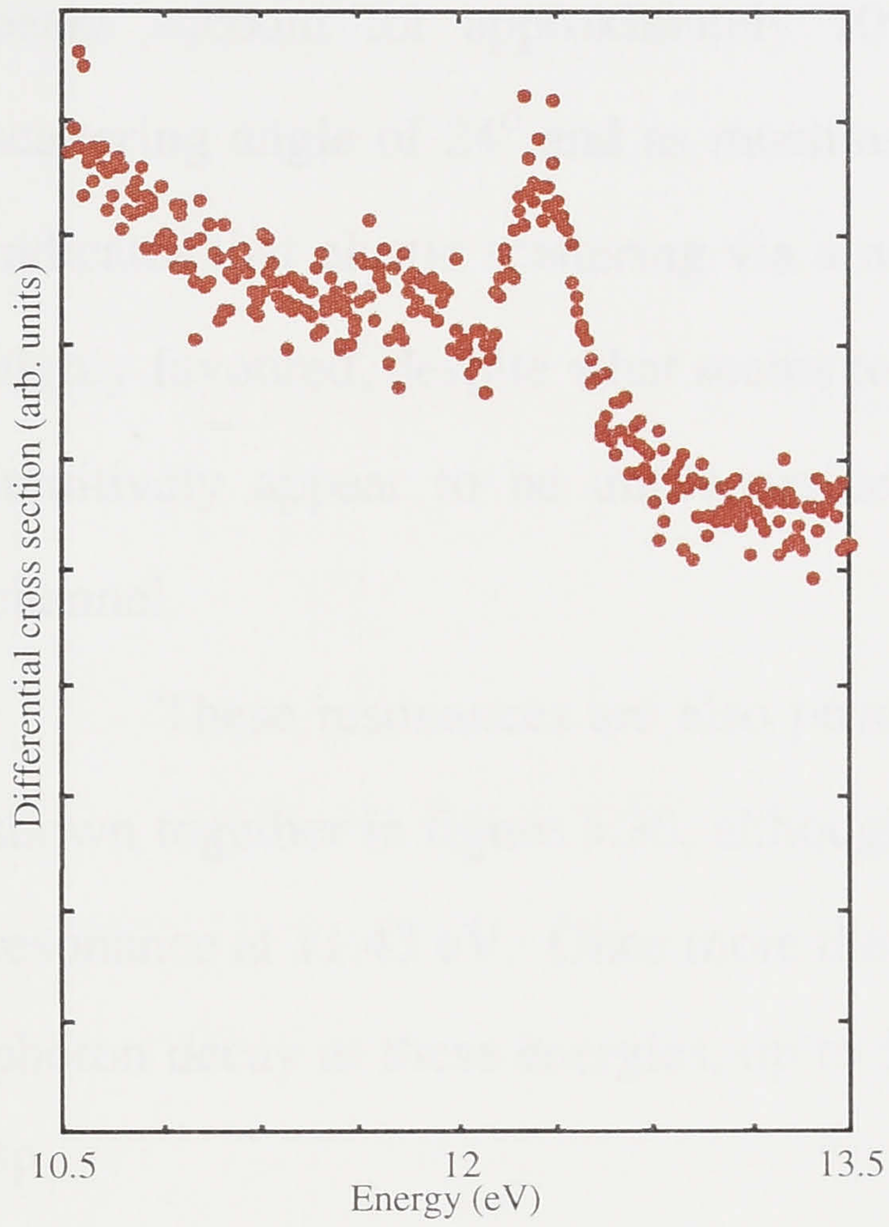

Figure 5.27: Elastic electron scattering from cadmium at 90 degrees

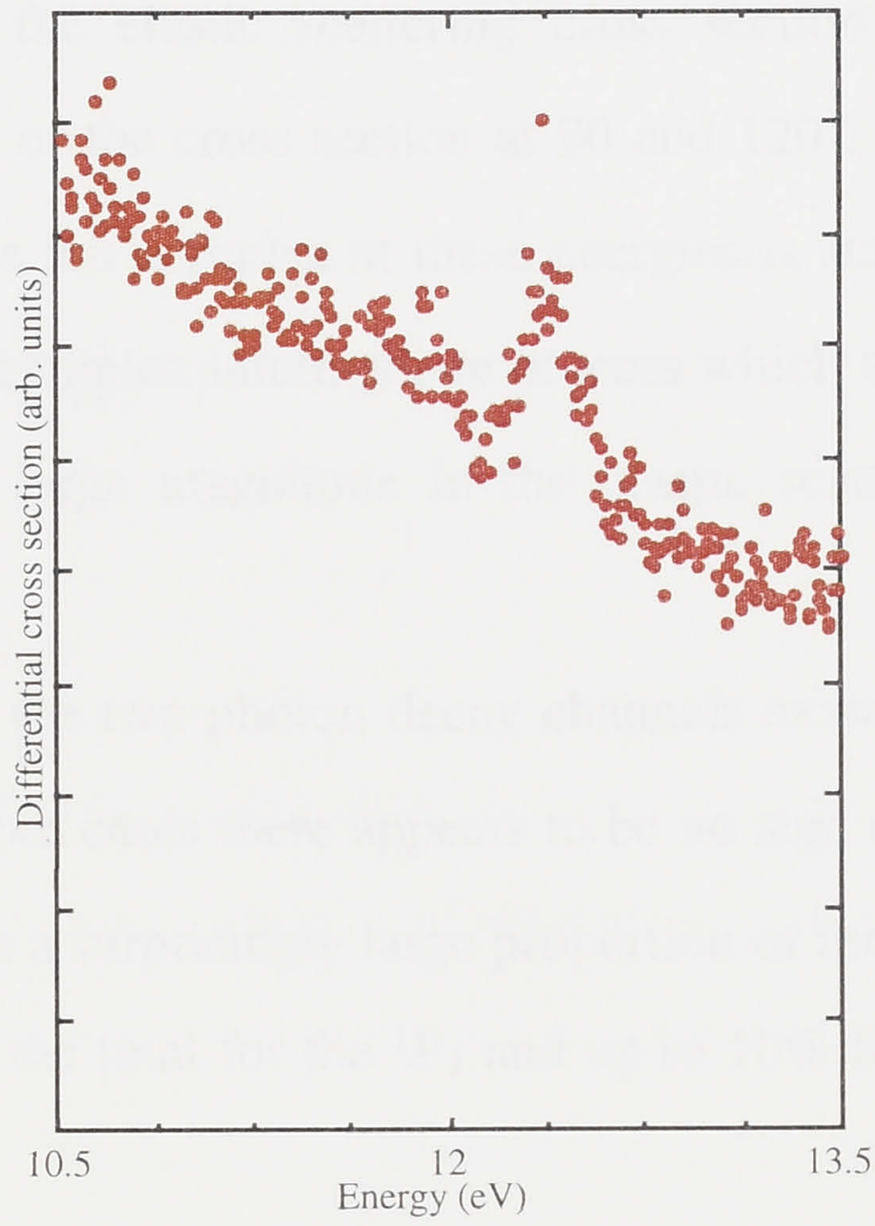

Figure 5.28: Elastic electron scattering from cadmium at 120 degrees

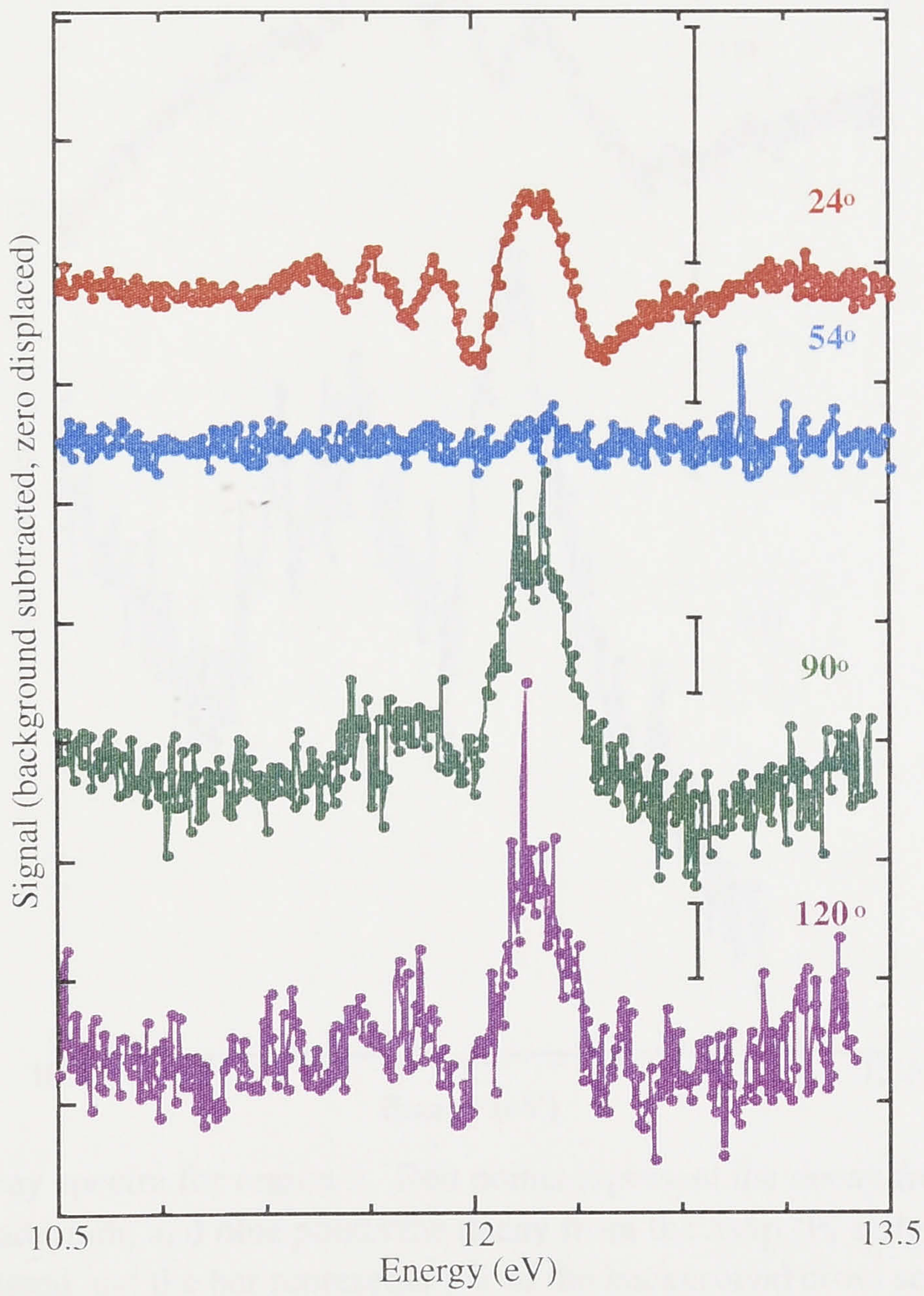

Figure 5.29: Behaviour of resonances in region 3 with scattering angle. The data has had a smoothly varying background subtracted and the zero has been suppressed at each angle. Bars represent 10% of the total scattered signal.

One feature worth noting in the elastic scattering spectra is that the resonance peaks account for approximately 10% of the elastic scattering cross section at a scattering angle of 24° and as much as 30% of the cross section at 90 and 120°. This indicates that elastic scattering via a negative ion complex at these energies is actually highly favoured, despite what seems to be a complex intermediate process which would intuitively appear to be unfavourable to a large magnitude in the elastic scattering channel.

These resonances are also present in the two photon decay channels examined, shown together in figure 5.30, although in both cases there appears to be no sign of the resonance at 11.43 eV. Once more they form a surprisingly large proportion of the total photon decay at these energies, up to 5% of the total for the $^1P_1$ and up to 10% for the $^3P_1$.

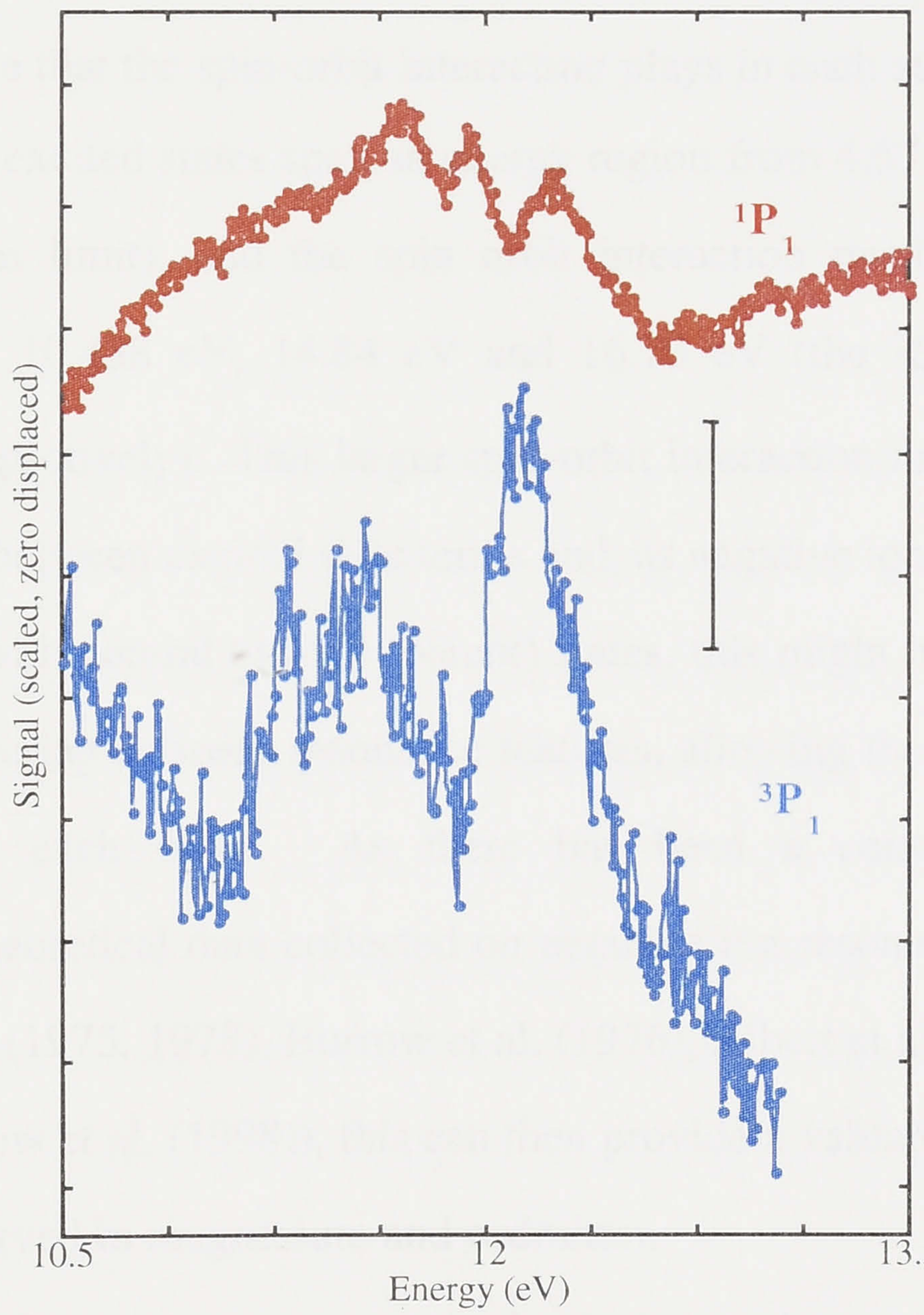

Figure 5.30: Photon decay spectra for region 3. Red points represent the decay from the 5s5p $^1P_1$ state to the ground state of cadmium, and blue points the decay from the 5s5p $^3P_1$ state. The zero has been suppressed and the bar represents 5% of the background cross section.

Chapter 6

Discussion

In considering the classifications of the resonances observed in the present study of magnesium and cadmium, a comparison to mercury can be of assistance, as there is a large body of experimental data for this atom and its negative ion spectrum should be similar to both magnesium and cadmium. Despite this, differences may be expected due, for example, to the differences in the energy spacing of their neutral excited states and the differing role that the spin-orbit interaction plays in each atom. For example, in mercury the neutral excited states span an energy region from 4.67 eV ($6p\ ^3P_0$) to 16.70 eV ($^2D_{3/2}$ ionisation limit), and the spin orbit interaction results in three different ionisation limits at 10.438 eV, 14.84 eV and 16.70 eV (the $^2S_{1/2}$, $^2D_{5/2}$ and $^2D_{3/2}$ ionisation limits respectively). This larger spin-orbit interaction in mercury also results in a larger splitting between excited state terms and, as negative ion resonances are often closely associated with neutral excited (parent) states, this might be expected to reduce the possibility of overlap between resonance features, allowing them to be more readily distinguished from each other. As there has been a considerable amount of experimental and theoretical data collected on negative ion resonances in mercury (see for instance Heddle (1975, 1978), Burrow et al. (1976), Albert et al. (1977), Newman et al. (1983) and Burrow et al. (1998)), this can then provide a valuable guide to analysing the resonances observed in magnesium and cadmium.

In analysing the resonance structure of cadmium and magnesium, the first group of resonances to be examined will be those with a $nsnp^2$ configuration, with n=3 for magnesium and n=5 for cadmium. It is constructive to compare these resonances with the corresponding resonances in mercury, with n=6 in this case. The reason for this is that the outer electron configuration of the neutral atom is ns^2 in all three elements, with

n=3,5 and 6. The major difference is that magnesium, as a Group IIA element, has no d-shell electrons within the outer ns^2 shell, unlike the situation for cadmium and mercury. Nonetheless, constructive comparisons can be made between the negative ion resonance spectra of all three elements.

Resonances that fall outside the $nsnp^2$ classification, as defined above, will be dealt with separately for each element.

6.1 The $nsnp^2$ resonances

Resonances belonging to the $6s6p^2$ configuration in mercury first appear around the threshold for the excitation of the 6s6p ^3P states of the neutral atom which occur at 4.67, 4.89 and 5.46 eV for the $^3P_0$, $^3P_1$ and $^3P_2$ .states respectively It is then to be expected that the resonances of the $3s3p^2$ and $5s5p^2$ configurations, in magnesium and cadmium respectively, will also occur near the corresponding thresholds in these atoms. Indeed resonances occuring at the np ^3P threshold have been observed in both these atoms, as the results presented in chapter 5 show. For the $nsnp^2$ configuration, a large number of terms are possible - $^4P_{1/2,3/2,5/2}$, $^2D_{3/2,5/2}$, $^2P_{1/2,3/2}$ and $^2S_{1/2}$. In the region around the 6s6p ^3P states in mercury 5 negative ion states in the $6s6p^2$ configuration have been unambiguously identified, the $^4P_{1/2}$ at 4.55 eV, $^4P_{3/2}$ at 4.67 eV, $^4P_{5/2}$ at 4.91 eV, $^2D_{3/2}$ at 5.2 eV and the $^2D_{5/2}$ at 5.55 eV (see Burrow et al. 1998 and references therein). In cadmium and magnesium we can reasonably expect these states to be present in the corresponding regions, and to have the same ordering in energy. Of the 5 states mentioned above, all are even parity. Decay to the ground state, which is also even parity, must then occur via emission of s-, d-, g-wave electrons and so on. The $^2P_{1/2}$ state must then decay to the ground state of cadmium by emission of an s-wave electron to conserve angular momentum, and the remaining states must all decay by emission of a d-wave electron.

In the electron scattering spectra for magnesium in this energy region, only one feature is observed. This feature, which is centred at 2.80 eV and near the threshold of the ^3P states in magnesium, displays a strong d-wave behaviour with scattering angle, all but disappearing at 54^o with a very strong presence at the other scattering angles

investigated. In magnesium, spin-orbit interaction is very weak and similar terms with differing angular momentum will be virtually degenerate, as witnessed by the 3s3p ^3P neutral excited states being very close together in energy, spread over only 7 meV. The location of this resonance feature and the close spacing of the ^3P states in neutral magnesium, suggests that this feature most likely comprises all 5 resonance terms that are mentioned above ($^4P_{1/2,3/2,5/2}$, $^2D_{3/2,5/2}$). If the negative ion states are shortlived and in close proximity to each other, the natural widths of the features in the spectrum will cause them to overlap, and they will be indistinguishable fom each other. As a result, it is unlikely that even with a greatly improved energy resolution, the individual resonance states would be able to be distinguished. The small presence of the feature at a scattering angle of 54° is probably due to the one resonance state ($3s3p^2\ ^2P_{1/2}$) that can decay to the ground state by emission of an s-wave electron. Thus the feature at 2.80 eV corresponds to a conglomeration of the $3s3p^2\ ^4P_{1/2}$, $^4P_{3/2}$, $^4P_{5/2}$, $^2D_{3/2}$ and $^2D_{5/2}$ states.

Two features are seen in cadmium in the region of the 5p $^3P_{0,1,2}$ excited states, at energies of 3.60 eV and 4.08 eV (see figure 5.16). The feature at 3.60 eV in cadmium is not present at a scattering angle of 54°, indicating autodetachment by emission of a d-wave electron. From the energy ordering in mercury, it would be expected that the first resonance would be due to the $5s5p^2\ ^4P_{1/2}$ state, which can only decay to the ground state by emission of an s-wave electron. This resonance feature is clearly not due to an s-wave electron, so it cannot be due to the $^4P_{1/2}$ state. The first of the resonances that can be expected to decay to the ground state by d-wave electron emission is the $^4P_{3/2}$ state. As a result, it is possible to identify this feature in cadmium as being due to the $5s5p^2\ ^4P_{3/2}$ negative ion state. On close examination, the electron transmission data of Burrow (1998) reveals a very small feature at an energy of 3.52 eV, which may be due to the $5s5p^2\ ^4P_{1/2}$ state. It also shows a larger feature at 3.59 eV, perhaps corresponding to the feature at 3.60 eV in the present data, which is believed to be the $Cd^-\ 5s5p^2\ ^4P_{3/2}$ state. The resonance at 3.52 eV in Burrow's data is very weak and, as the sensitivity of Burrow's experiment to resonance features is much higher than can be achieved with the present apparatus, it is not unreasonable to speculate that the smaller $^4P_{1/2}$ resonance is

not able to be observed in the present experiments. The larger feature in this energy region of cadmium, at 4.08 eV, is then likely to be a combination of the remaining three negative ion states, namely the $5s5p^2\ ^4P_{5/2}$, $^2D_{3/2}$ and $^2D_{5/2}$ states. These states all decay to the ground state of cadmium by emission of a d-wave electron, meaning that we can expect the feature to have a minimum at a scattering angle of 54°. Figure 5.5 shows the behaviour of this feature as a function of scattering angle, and it can be seen that it does indeed display a minimum at an angle of 54°, although there is some small presence of a peak at 4.08 eV. The small presence at 54° may possibly be due to the angular resolution of the electron detectors of ±2°. Another possible reason for the small presence of the resonance could be due to the breakdown of the assumption that there are no relativistic effects in this atom (see section 2.1.3). Relativistic effects will lead to the d-wave in the partial wave expansion to break into $d_{3/2}$ and $d_{5/2}$ partial waves, which do not necessarily have a minimum at 54°. This could then lead to a small feature due to the resonance at this scattering angle.

In the case of cadmium, there is also data in this energy region from the $5p\ ^3P_1$ photon excitation function. This spectrum displays a large peak with a maximum at an energy 4.17 eV. The most likely states to contribute to this peak are, once again, the $^4P_{5/2}$, $^2D_{3/2}$ and $^2D_{5/2}$ states, given their appearance at around this energy in the elastic electron scattering spectrum. Analysis of the eigenphase sums of the calculation of Bartschat (1998) bears out the assumption that a combination of the above three states gives rise to the onset feature in this case.

The cadmium metastable excitation spectrum shown in figure 3.29 also shows a sharp feature that occurs at approximately 4.0 eV, which is similar to the peak observed at 4.702 eV in the mercury metastable excitation experiments performed by Newman et al. (1985) that was classified as the $6p^2\ ^4P_{3/2}$ state. However, the $5p^2\ ^4P_{3/2}$ state in Cd^- has already been accounted for, at an energy of 3.60 eV. It may be that the peak observed in the metastable spectrum lies somewhat lower than the estimated 4.0 eV, accounting for the discrepancy. This could be due to the difficulties in determining the precise peak position from the data, and also the energy calibration for this spectrum,

which is only accurate to within 100 meV rather than the 25 meV which applied to the other spectra.

In both magnesium and cadmium, a resonance has been observed that straddles the np $^1P_1$ threshold at an energy of 4.30 eV and 5.42 eV respectively (see figures 5.10 and 5.22). These resonances are both present at all angles in the elastic scattering data, although the intensity at an angle of 90° appears to be somewhat reduced in both cases. The classifications offered above leave several terms of the $nsnp^2$ configuration unaccounted for in each atom (the $^2P_{1/2}$, $^2P_{3/2}$ and $^2S_{1/2}$ terms). In mercury, Newman et al. (1985) found one resonance state that occurred at the threshold of the 6s6p $^1P_1$ excited state and one that occured approximately 150 meV below the threshold. This neutral state corresponds, by analogy, to the 3s3p $^1P_1$ state in magnesium and the 5s5p $^1P_1$ state in cadmium. From arguments based on the isoelectronic series, Newman et al. classified these resonances as the $^2P_{1/2}$ and $^2S_{1/2}$ resonance configurations, with the $^2S_{1/2}$ feature the stronger and higher lying of the two (at the 6s6p $^1P_1$ threshold).

Once again, it might be reasonably expected that the same terms are responsible for the features observed near the np $^1P_1$ thresholds in magnesium and cadmium at energies of 4.30 eV and 5.42 eV respectively, with the $^2S_{1/2}$ state making the dominant contribution. Both of these configurations will decay to the ground state of the atom by autodetachment of an s-wave electron, which is the observed behaviour in both cases. Also in both cases, there is evidence of this resonance feature in the excitation function for the $^1P_1$ state (figures 5.11 and 5.24). The resonance is also present in the $^3P_1$ excitation function taken for cadmium (figure 5.23). In both $^1P_1$ excitation functions there is a sharp onset due to the overlap of the resonance with the $^1P_1$ threshold, whilst in the $^3P_1$ spectrum for cadmium, the resonance appears as a peak. The calculations of Bartschat (1998) suggest that the corresponding feature in the $^3P_1$ spectrum for cadmium is due to a negative ion configuration of 5s5p5d, as opposed to the $5s5p^2$ configuration. A resonance with this former configuration would have odd parity and would decay to the ground state in elastic electron scattering by emission of a p- or f-wave electron. This proposal is not well supported by the electron scattering data presented in figure 5.22. However, the reduced magnitude of the feature at 90° could

possibly be due to the presence of another resonance, overlapping the two $5s5p^2$ states, which decays to the ground state by emission of a p-wave electron. It may be then, that there is also a resonance present at this energy in cadmium with the 5s5p5d configuration proposed by Bartschat. As the resonance at 4.30 eV in magnesium is similarly positioned to the cadmium resonance with respect to the $^1P_1$ threshold and displays the same behaviour as a function of scattering angle, it may be that a similar 3s3p3d resonance is present in magnesium as well.

One discrepancy between the $6p^2\ ^2S_{1/2}$ resonance in mercury and the features observed at the corresponding thresholds in magnesium and cadmium is the large difference in the natural widths of the features. The $^2S_{1/2}$ resonance in mercury has a width of approximately 20 meV based on the measurements of Newman et al. (1985), and the threshold features in magnesium and cadmium have widths of 100 meV and 215 meV respectively. In mercury, the $^2S_{1/2}$ and $^2P_{1/2}$ are separated by approximately 150 meV (Newman et al., 1985), meaning that the overlap between the two is minimal. For magnesium and cadmium, where the spin-orbit interaction is smaller, the separation between these two states can be expected to be reduced, so that they will likely overlap. This may then also account for the greater widths observed. If there is indeed another resonance present in both cases with a nsnpnd (n=3 for magnesium and n=5 for cadmium) configuration, this will also contribute to a larger energy width than the $^2S_{1/2}$ resonance in mercury.

There is one other possible alternative for this near-threshold feature. The appearance of the feature in the electron transmission data of Burrow (1998) for both magnesium and cadmium is similar to that which is observed for a cusp at the opening of a new channel. If this were the case, the corresponding feature in the elastic scattering spectra would be expected to be a downward step, rather than the clearly defined dip which is observed in elastic scattering and in the $5p\ ^3P_1$ excitation function for cadmium. As a result, this possibility has been ruled out.

As the $3s3p^2\ ^2P_{3/2}$ state will be degenerate with the $^2P_{1/2}$ state in magnesium, and thus occur at the same energy (4.30 eV), this then leaves only the $^2P_{3/2}$ state to be accounted for in the $5s5p^2$ configuration for cadmium. The next two higher energy

resonances which are observed in mercury have been classified as the $7s^2\ ^2S_{1/2}$ and $6p^2\ ^2P_{3/2}$ terms by Newman et al. (1985). These correspond to the $6s^2\ ^2S_{1/2}$ and $5p^2\ ^2P_{3/2}$ states for the cadmium negative ion, presuming that the energy ordering remains the same between the two elements. The next resonance structure that has been identified in cadmium is the feature at 6.60 eV which displays a d-wave behaviour with scattering angle, as shown in figure 5.22. Of the two possible resonance states, only the $^2P_{3/2}$ state can decay to the ground state via ejection of a d-wave electron, so a classification for this resonance of $5p^2\ ^2P_{3/2}$ seems reasonable in this case. The position and classifications of the $nsnp^2$ resonances for magnesium, cadmium and mercury are summarised in table 6.1.

Resonance state	Mercury	Cadmium	Magnesium
$nsnp^2\ ^4P_{1/2}$	4.55	3.52*	2.80
$nsnp^2\ ^4P_{3/2}$	4.67	3.60	2.80
$nsnp^2\ ^4P_{5/2}$	4.91	4.08	2.80
$nsnp^2\ ^2D_{3/2}$	5.2	4.08	2.80
$nsnp^2\ ^2D_{5/2}$	5.55	4.08	2.80
$nsnp^2\ ^2P_{1/2}$	6.6	5.42	4.30
$nsnp^2\ ^2S_{1/2}$	6.702	5.42	4.30
$nsnp^2\ ^2P_{3/2}$	7.8	6.60	4.30

Table 6.1: Summary of the $nsnp^2$ resonance energies for mercury, cadmium and magnesium. Energies are in electron volts. Values for mercury are from Newman et al. (1985) and Burrow et al. (1998). Values for cadmium and magnesium are from the present work, except for the value marked (*), which is from Burrow (1998).

Shpenik et al. (1979) assigned the $3p^2\ ^2S$ and ^2P states to two separate features in magnesium occurring at 4.7 eV and 5.2 eV respectively. This does not agree with the classification proposed above for these two resonances. The analysis in their case was based on the series of doubly excited states in aluminium, which is isoelectronic to the magnesium negative ion, and did not have any electron scattering data with which to compare. It may be that the features observed by Shpenik et al. are from other

resonance states with a different electronic configuration to the $3s3p^2$ configuration they propose.

6.2 Higher-lying resonances in magnesium

There are several resonances observed in the current experiments on magnesium that are unaccounted for by the $3s3p^2$ electronic configuration. The first of these is observed in the elastic electron scattering data at 4.85 eV, and is consistent with decay into the ground state by autodetachment of a p-wave electron (see figure 5.10). This means that the resonance state has to have odd parity, indicating that the electron configuration would possibly be 3s3p4s or 3s3p3d. The possible states in the 3s3p4s configuration are ^2P or ^4P (remembering that the different angular momentum components are degenerate in this case), and the possible states in the 3s3p3d configuration are ^2P, ^2D, ^2F, ^4P, ^4D and ^2F. Many of these states will decay to the ground state by autodetachment of a p-wave electron, and without further information, there is no way to assign one of these states to the feature observed. Given the proximity to the 3s4s ^3S threshold (5.11 eV) it is possible that the resonance has the 3s3p4s configuration. None of the states in the corresponding electron configurations in Hg^- (i.e. 6s6p7s and 6s6p6d) have been identified, so this classification remains tentative. The three remaining resonances observed in the electron scattering experiments were at energies of 5.30 eV (autodetachment by p- or d-wave electron), 5.71 eV (autodetachment by p-wave electron) and 6.39 eV (autodetachment by s-wave electron). The first two of these may be due to either of the two electron configurations above but, as before, it is not possible to definitively classify these resonances. Shpenik et al. (1979) observed a resonance at 5.7 eV and classified it as 3s3p4s ^4P, which would be consistent with the observations in this case. The resonance at 6.39 eV lies just below (~50 meV) the 3s5s ^3S state, and may be a Feshbach resonance with that state as its parent, giving a configuration of $3s5s^2$, although this remain highly speculative.

Three features were noted in the $^1P_1$ excitation spectrum for magnesium, at energies of 5.2 eV, 5.5 eV and 6.28 eV. The first two of these appear as changes in the

slope of the spectrum (see figure 5.11). It is probable that the first two features are due to new excitation channels opening, in the first case the 3s4s $^3S_1$ state threshold is passed, resulting in a loss of flux to the 3p $^1P_1$ state, and in the second case the 3s4s $^1S_0$ threshold is passed, increasing the flux into the $^1P_1$ state, which is similar to the situation for cadmium outlined in section 5.2.3. Shpenik et al. (1979) classified a feature at 5.2 eV in their 3p $^1P_1$ excitation function as the $3s3p^2$ ^2P resonance, but that state has already been accounted for in this analysis. The remaining feature at 6.28 eV is a resonance feature, and has also been observed by Shpenik et al. (1979), although in the 4s $^3S_1$ excitation function rather than the 3p $^1P_1$ excitation function. In their analysis this resonance has been classified as the 3s3p3d ^2P state. Another possible option is that it is also a Feshbach resonance with the 3s5s $^3S_1$ state as its parent, as it lies just beneath the threshold of this state (6.44 eV). It is unlikely that this is the same resonance as that observed at 6.39 eV in the elastic scattering spectrum as, in both cases, the energy calibration is to within 25 meV (see section 4.1.4). Table 6.2 summarises the classifications of the higher-lying resonances observed in magnesium.

Energy (eV)	Configuration
4.85	3s3p4s
5.30	3s3p4s/3s3p3d
5.71	3s3p4s/3s3p3d
6.28	3s3p3d (^4P)
6.39	$3s5s^2$

Table 6.2: Tentative assignments for remaining resonances observed in magnesium. The state assignment in parentheses is from Shpenik et al. (1979).

6.3 Higher-lying resonances in cadmium

6.3.1 Below the ionisation potential

The next two resonances unaccounted for in cadmium in the current experiments lie below the ionisation potential. The first is at an energy of 7.24 eV, where several other configurations of the negative ion are possible giving rise to many different possible negative ion states, the $5s6s^2$ ($^2S_{1/2}$ state), $5s6p^2$ ($^2S_{1/2}$, $^2P_{1/2,3/2}$, $^4P_{1/2,3/2,5/2}$ and

$^2D_{3/2,5/2}$ states) and $5s5d^2$ ($^2S_{1/2}$, $^2P_{1/2,3/2}$, $^4P_{1/2,3/2,5/2}$, $^2D_{3/2,5/2}$, $^4D_{3/2,5/2,7/2}$, $^2F_{5/2,7/2}$, $^4F_{5/2,7/2,9/2}$ and $^2G_{7/2,9/2}$ states) configurations. The resonance displays behaviour consistent with ejection of a d-wave electron, as there is no evidence of the resonance at a scattering angle of 54°. One clue to the identity of the negative ion state that gives rise to this feature may be that it is located at the threshold of the 5s6p ^3P states at 7.245 eV. This is similar to the position of the $5s5p^2$ states which occur around the 5s5p ^3P threshold at 3.737 eV, which could indicate that this feature has the configuration of $5s6p^2$, and is made up of the $^4P_{1/2,3/2,5/2}$, $^2D_{3/2}$ and $^2D_{5/2}$ states. This would also lead predominantly to decay by autodetachment of a d-wave electron, which is observed in this case.

The final resonance observed in cadmium below the ionisation threshold is the resonance in the $^1P_1$ decay spectrum at an energy of 7.90 eV. This lies just above the 5s7s $^1S_0$ state of neutral cadmium which occurs at 7.828 eV, and by analogy to the previous analysis could be due to the $5s6p^2$ $^2P_{3/2}$ state of the negative ion, given that the $5s5p^2$ $^2P_{3/2}$ negative ion state lies close to the 5s6s $^1S_0$ threshold of neutral cadmium.

Three other possible resonance features are observed in the metastable excitation spectrum presented in figure 3.29, occuring at 5.9 eV, 6.9 eV and 7.9 eV. It is not possible to definitely assign energies to these features, due to the quality of the data in this case, but certainly indications are that a metastable excitation measurement could provide valuable further information about the negative ion resonance spectrum in cadmium.

6.3.2 Above the ionisation potential

Several resonances have been observed in cadmium above the first ionisation potential, in the autoionising region of neutral cadmium, both in photon excitation functions and elastic electron scattering experiments. These features occur at energies of 11.43 eV, 11.64 eV, 11.88 eV and 12.20 eV, and all indicate decay to the ground state by autodetachment of a d-wave electron, as demonstrated in figure 5.29. There are three core-excited states of neutral cadmium in this energy region, the $4d^95s^2(^2D_{5/2})5p$ $^1P_1$ at 12.122 eV, $4d^95s^2(^2D_{3/2})5p$ $^3P_1$ at 12.819 eV and the $4d^95s^2(^2D_{3/2})5p$ $^3D_1$ at

12.934 eV (Moore, 1971). It would be expected that resonances in this region would be associated with these states of the neutral atom, and have the electronic configuration $4d^9 5s^2(^2D_{5/2}$ or $^2D_{3/2})5p^2$. Resonances with the configuration $5d^9 6s^2(^2D_{3/2})6p^2$ and $5d^9 6s^2(^2D_{5/2})6p^2$, have been observed in mercury (Newman et al. 1985), and are grouped around the first ionisation potential (10.438 eV). The parent states of these resonances are core excited states in neutral mercury ($5d^9 6s^2(^2D_{3/2})6p$), which commence only 0.57 eV above this first ionisation threshold. Feschbach resonances (which typically lie energetically below the parent state, see chapter 2) associated with the $5d^9 6s^2(^2D_{3/2,5/2})6p$ parent states in mercury are then located around the first ionisation threshold in energy. In the case of cadmium, the core-excited parent states ($4d^9 5s^2(^2D_{5/2})5p\ ^1P_1$, $4d^9 5s^2(^2D_{3/2})5p\ ^3P_1$ and the $4d^9 5s^2(^2D_{3/2})5p\ ^3D_1$ states) occur well above the ionisation threshold (~3.13 eV), so that any Feschbach resonance with this parent state will still lie well above the ionisation threshold in energy. Resonances with this electronic configuration must, from considerations of angular momentum and parity, decay to the ground state of neutral cadmium by autodetachment of a d-wave electron, which is consistent with the observations in the elastic electron scattering experiments. It is not possible in this case to predict precisely which terms give rise to these resonances in cadmium, as once more there is no good way of separating the many options available on the basis of the current data. Table 6.3 summarises the proposed classifications for the higher-lying resonances observed in cadmium.

Energy (eV)	Configuration
7.24	$5s6p^2\ (^4P_{1/2,3/2,5/2},\ ^2D_{3/2,5/2})$
7.90	$5s6p^2\ (^2P_{3/2})$
11.43	$4d^9 5s^2(^2D_{5/2},\ ^2D_{3/2})5p^2$
11.64	$4d^9 5s^2(^2D_{5/2},\ ^2D_{3/2})5p^2$
11.88	$4d^9 5s^2(^2D_{5/2},\ ^2D_{3/2})5p^2$
12.20	$4d^9 5s^2(^2D_{5/2},\ ^2D_{3/2})5p^2$

Table 6.3: Tentative assignments for remaining resonances observed in cadmium. Some speculative state assignments are in parentheses.

Chapter 7

Conclusion

7.1 Summary of results

In this thesis, a systematic study of negative ion resonances in heavy metals has been commenced. A new oven was designed for the crossed beam apparatus using resistive heating wires instead of the previous design which was based on electron bombardment. This was used to study the negative ion resonance structure of magnesium and cadmium. A metal vapour beam trap was also designed using an automated liquid nitrogen cooling system, and these two additions to the apparatus greatly increased the length of time the apparatus could be operated without major intervention. A photon detection system incorporating a photomultiplier tube was also designed and incorporated into the system, allowing the measurement of optical excitation functions, in addition to the previously available elastic electron scattering system. This also provided a reliable means of calibrating the energy of the electron beam during the experiments on metal vapours.

After analysing the results from elastic electron scattering and excitation function experiments, all the resonance terms from the $3s3p^2$ configuration in magnesium and the $5s5p^2$ configuration in cadmium have been identified. This was done by considering the energy of each resonance, its behaviour with scattering angle, and previous work on negative ion resonances in mercury. The analysis has been compared, where possible, with previous experimental and theoretical work on these systems.

Several other resonances have been identified in each of these systems, and tentative classifications for those have been proposed, again based on the energy, behaviour with scattering angle and previous work on mercury.

An attempt was made to design and build a detector to measure the metastable excitation function for the 5s5p $^3P_{0,2}$, but despite very promising initial results the detector proved unsuccessful.

7.2 Future directions

There is a lot of work that remains to be done in investigating the negative ion resonance structure of heavy metallic atoms. An investigation of the elastic differential cross section for mercury in the region of the $6s6p^2\ ^2S_{1/2}$ resonance feature seen in metastable excitation by Newman et al. (1985), at an energy of 6.702 eV, would allow the confirmation of the classification proposed by them and complete the examination of the $nsnp^2$ resonances in magnesium, cadmium and mercury. There is also scope for a series of differential elastic electron scattering measurements in the higher reaches of the mercury spectrum, in order to provide some confirmation of the classifications proposed by Newman et al. (1985) which were based on total metastable production measurements.

The series of elements increasing in atomic number from mercury to thallium, lead and bismuth, provides an attractive prospective area for study as the variation in resonance structure could be examined as successive electrons are added to the outer electron shell (Hg $6s^2$, Tl $6s^26p$, Pb $6s^26p^2$, Bi $6s^26p^3$). This is in contrast to the present study where the outer electron configuration is similar, with only the principle quantum number changing from magnesium through to mercury. Experiments on these metals should be possible with minimal modifications to the current oven design, and quite low vapour pressures are needed when the exit aperture of the oven lies so close (2 mm) to the electron beam.

Whilst problems were encountered with the inconsistent operation of the metastable cadmium atom detector, this is the first attempt to measure such a spectrum, and the results are extremely encouraging for future investigation. It is possible that design modifications to the metastable detector would enable it to be used for heavy metal systems other than cadmium, perhaps if a system can be found where the

energetics of electron emission from the impact of metastable excited atoms on the samarium surface are more favourable.

Another possible future project would be to install new electron detectors to enable the detection of inelastically scattered electrons in addition to the elastic scattering channel - the only channel that is possible at the moment. This would increase the versatility of the apparatus by allowing investigation of resonances in the various inelastic differential cross sections that may be only weakly apparent in the elastic differential cross section. Investigating these resonances as a function of scattering angle in different differential cross sections (i.e. both elastic and inelastic) would allow a more confident classification of the observed resonances.

Provision for a larger number of electron detectors has also been included in the original design for the apparatus, and if more detectors were built, the time required for a complete investigation of the resonance structure of an element could be halved, resulting in a much greater efficiency in the experimental investigations.

References

K. Albert, C. Christian, T. Heindorff, E. Reichert and S. Schön, J. Phys. B, 10, 3733 (1977)

I. S. Aleksakhin, I. P. Zapesochnyi, I. I. Garga and V. P. Starodub, Opt. Spectrosc., 34, 611 (1973)

J. N. Bardsley and B. R. Junker, J. Phys. B, 5, L178 (1972)

M. Bartsch, H. Geesmann, G. F. Hanne and J. Kessler, J. Phys. B, 25, 1511 (1992)

K. Bartschat 1998, private communication

R. P. Bauman and N. L. S. Martin, Rev. Sci. Instrum., 66, 4900 (1995)

M. Bentley, Phys. Rev. A, 44, 5414 (1991)

K. A. Berrington, P. G. Burke and A. L. Sinfailam, J. Phys. B, 8, 1459 (1975)

K. Bethge, E. Heinicke and H. Baumann, Phys. Lett., 23, 542 (1966)

A. K. Bhatia and A. Temkin, Phys. Rev. A, 23, 3361 (1981)

W. L. Borst, Phys. Rev., 181, 257 (1969)

W. L. Borst, J. Chem. Phys, 67, 2920 (1977)

B. H. Bransden and C. J. Joachain 1983 "Physics of Atoms and Molecules" Longman Group Ltd, Hong Kong

W. H. Brattain, Phys. Rev., 34, 474 (1929)

J. N. H. Brunt, G. C. King and F. H. Read, J. Phys. B, 9, 2195 (1976)

S. J. Buckman and C. W. Clark, Rev. Mod. Phys., 66, 539 (1994)

S. J. Buckman, P. Hammond, F. H. Read and G. C. King, J. Phys. B, 16, 4039 (1983a)

S. J. Buckman, P. Hammond, G. C. King and F. H. Read, J. Phys. B, 16, 4219 (1983b)

S. J. Buckman and D. S. Newman, J. Phys. B, 20, L711 (1987)

P. G. Burke, J. W. Cooper and S. Ormonde, Phys. Rev., 183, 245 (1969)

P. D. Burrow 1998, private communication

P. D. Burrow, J. A. Michejda and J. Comer, J. Phys. B, 9, 3225 (1976)

P. D. Burrow, J. A. Michejda, D. R. Lun, J. P. Sullivan, R. P. McEachran, D. S. Newman and S. J. Buckman, J. Phys. B, 31, L1009 (1998)

B. L. Christiensen-Dalsgaard, J. Phys. B, 21, 2539 (1988)

J. Comer and F. H. Read, J. Phys. B, 4, 1055 (1971)

G. D. Doolan, J. Nuttall and R. W. Stagart, Phys. Rev. A, 10, 1612 (1974)

J. L. Erskine 1995 "Electron Energy Analysers" (Ch. 6) in "Atomic, Molecular, and Optical Physics: Charged Particles", F. B. Dunning and R. G. Hulet (editors), in "Experimental Methods in the Physical Sciences" R. Celotta and T. Lucartorto (editors in chief) Academic Press, San Diego

I. I. Fabrikant, J. Phys. B, 7, 91 (1974)

U. Fano, J. Phys. B, 13, 603 (1980)

J. M. Feagin and J. S. Briggs, Phys. Rev. Lett., 57, 984 (1986)

J. M. Feagin and J. S. Briggs, Phys. Rev. A, 37, 4599 (1988)

A. H. Firester, Rev. Sci. Inst., 37, 1264 (1966)

R. J. Fleming and G. S. Higginson, Proc. Phys. Soc. Lond., 81, 974 (1963)

V. A. Fock, K. Nor. Vidensk. Selsk. Forh., 31, 138 (1958)

W. C. Fon, K. A. Berrington, P. G. Burke and A. E. Kingston, J. Phys. B, 11, 325 (1978)

W. C. Fon, K. A. Berrington, P. G. Burke and A. E. Kingston, J. Phys. B, 22, 3939 (1989)

H. Fukuda, N. Koyama and M. Matsuzawa, J. Phys. B, 20, 2959 (1987)

V. Gedeon, V. Lengyel, O. Zatsarinny and C. A. Kocher, Phys. Rev. A, 59, 2016 (1999)

D. E. Golden and H. W. Bandel, Phys. Rev., 138, A14 (1965)

R. J. Gulley 1994 "Low Energy Electron Scattering from Polar Polyatomic Molecules" PhD thesis, Australian National University, unpublished

E. Harting and F. H. Read 1976 "Electrostatic Lenses" Elsevier Scientific Publishing Co., Amsterdam

A. U. Hazi, J. Phys. B, 11, L259 (1978)

A. U. Hazi, Phys. Rev. A, 19, 920 (1979)

D. W. O. Heddle, J. Phys. B, 8, L33 (1975)

D. W. O. Heddle, Proc. R. Soc. London Ser. A, 352, 441 (1977)

D. W. O. Heddle, J. Phys. B, 11, L711 (1978)

D. W. O. Heddle 1991, "Electrostatic Lens Systems" Adam Hilger - IOP Publishing, Bristol

Y. K. Ho, Phys. Rev. A, 45, 4402 (1992)

J. Hunt and B. L. Moiseiwitsch, J. Phys. B, 3, 892 (1970)

C. J. Joachain 1975 "Quantum Collision Theory" Elsevier Scientific Publishing Co., Amsterdam

B. R. Junker, Adv. At. Mol. Phys., 18, 207 (1982a)

B. R. Junker, J. Phys. B, 15, 4495 (1982b)

F. Karstensen and H. Köster, Astron. Astrophys., 13, 116 (1971)

L. Kim and C. H. Green, J. Phys. B, 22, L175 (1989)

H. Klar, Phys. Rev. Lett., 57, 66 (1986)

O. Klemperer and M. E. Barnett 1971 "Electron Optics" Cambridge University Press, Cambridge

L. Koch, T. Heindorff and E. Reichert, Z. Phys. A, 316, 127 (1984)

N. Koyama, A. Takafuji and M. Matsuzawa, J. Phys. B, 22, 553 (1989)

P. Krylstedt, N. Elander and E. Brändas, J. Phys. B, 21, 3969 (1988)

P. Krylstedt, M. Rittby, N. Elander and E. Brändas, J. Phys. B, 20, 1295 (1987)

H. A. Kurtz and K. D. Jordan, J. Phys. B, 14, 4361 (1981)

R. W. LeBahn and J. Callaway, Phys. Rev., 135, 1539 (1964)

M. Le Dourneuf and S. Watanabe, J. Phys. B, 23, 3205 (1990)

D. Leep and A. Gallagher, Phys. Rev. A, 13, 148 (1976)

L. Lichten, Phys. Rev., 109, 1191 (1958)

C. D. Lin, Phys. Rev. A, 10, 1986 (1974)

C. D. Lin, J. Phys. B, 16, 723 (1983)

C. D. Lin and S. Watanabe, Phys. Rev. A, 35, 4499 (1987)

L. Lipsky, R. Anania and M. J. Connelly, At. Data Nucl. Data Tables, 20, 127 (1977)

J. Macek, J. Phys. B, 1, 831 (1968)

J. Macek and J. M. Feagin, J. Phys. B, 18, 2161 (1985)

B. Marinkovic, V. Pejcev, D. Filipovic and L. Vuskovic, J. Phys. B, 24, 1817 (1991)

N. L. S. Martin and D. B. Thompson, Phys. Rev. A, 43, 2281 (1991)

N. L. S. Martin, D. B. Thompson, R. P. Bauman, M. Wilson, J. Jimenez-Mier, C. D. Caldwell and M. O. Krause, J. Phys. B, 27, 3945 (1994)

C. W. McCurdy, J. G. Lauderdale and R. C. Mowrey, J. Chem. Phys., 75, 1835 (1981)

E. W. McDaniel 1989 "Atomic Collisions - Electron and Photon Projectiles" John Wiley and Sons, New York

R. P. McEachran 1997, private communication

R. P. McEachran and A. D. Stauffer, J. Phys. B, 25, 1527 (1992)

C. E. Moore 1971 "Atomic Energy Levels" National Standards Reference Data System, U. S. Government Printing Office, Washington D. C.

J. H. Moore, C. C. Davis and M. A. Coplan 1989 "Building Scientific Apparatus" Addison-Wesley Publishing Co. Inc., Massachusetts

D. L. Moores and D. W. Norcross, J. Phys. B, 5, 1482 (1972)

D. L. Moores and D. W. Norcross, Phys. Rev. A, 10, 1646 (1974)

N. F. Mott and H. S. W. Massey 1965 "The Theory of Atomic Collisions" 3rd edition, volume 2, Oxford University Press, Oxford

D. S. Newman, M. Zubek and G. C. King, J. Phys. B, 18, 985 (1985)

D. S. Newman, M. Zubek and G. C. King, J. Phys. B, 16, 2247 (1983a)

D. S. Newman, G. C. King and M. Zubek 1983b, Proc. 13th ICPEAC (ed. J. Eichler), Amsterdam, North Holland, p 104

J. Nuttall 1972, as cited in Bardsley and Junker (1972)

R. Panajotovic, M. Minic, B. Marinkovic, V. Pejcev and D. Filipovic, 17th Summer School and International Symposium on the Physics of Ionised Gases (1994)

A. Pathak, A. E. Kingston and K. A. Berrington, J. Phys. B, 21, 2939 (1988)

J. R. Pierce 1949 "Theory and Design of Electron Beams" Van Nostrand, Princedon and London

A. R. P. Rau, J. Phys. B, 16, L699 (1983)

F. H. Read, J. Phys. B, 10, 449 (1977)

F. H. Read, J. Phys. E, 16, 636 (1983)

T. N. Rescigno, C. W. McCurdy and A. E. Orel, Phys. Rev. A, 17, 1931 (1978)

K. Richter and D. Wintgen, J. Phys. B, 23, L197 (1990)

J. M. Rost and J. S. Briggs, J. Phys. B, 21, L233 (1988)

J. M. Rost, R. Gersbacher, K. Richter, J. S. Briggs and D. Wintgen, J. Phys. B, 24, 2455 (1991)

H. R. Sadeghpour, Phys. Rev. A, 43, 5821 (1991)

G. J. Schulz, Phys. Rev. Lett., 10, 104 (1963)

G. J. Schulz, Rev. Mod. Phys, 45, 378 (1973)

N. S. Scott, K. Bartschat, P. G. Burke, O. Nagy and W. B. Eissner, J. Phys. B, 17, 3775 (1984)

O. B. Shpenik, I. P. Zapesochnyi, V. V. Sovter, E. E. Kontrosh and A. N. Zavilopulo, Zh. Eksp. Teor. Fiz., 65, 1797 (1973)

O. B. Shpenik, I. P. Zapesochnyi, E. E. Kontrosh, E. I. Nepiipov, N. I. Romanyuk and V. V. Sovter, Sov. Phys. JETP 49, 426 (1979)

I. I. Shafran'osh, T. A. Snegurskaya and I. S. Aleksakhin, Opt. Spectrosc., 76, 20, 1994

A. J. F. Siegert, Phys. Rev., 56, 750 (1939)

L. T. Sin Fai Lam, J. Phys. B, 14, L437 (1981)

J. A. Simpson and U. Fano, Phys. Rev. Lett., 11, 158 (1963)

Sultana N. Nahar, Phys. Rev. A, 43, 2223 (1991)

R. Szmytkowski and J. E. Sienkiewicz, J. Phys. B, 27, 555 (1994)

K. T. Taylor and D. W. Norcross, Phys. Rev. A, 34, 3878 (1986)

J. K. Van Blerkom, J. Phys. B, 3, 932 (1970)

G. J. Wannier, Phys. Rev., 90, 817 (1953)

A. W. Weiss, Phys. Rev., 166, 166, (1968)

A. W. Weiss and M. Krauss, J. Chem. Phys., 52, 4363 (1970)

J. Yuan and Z. Zhang, J. Phys. B, 22, 2751 (1989)

I. P. Zapesochnyi, V. V. Sovter, O. B. Shpenik and A. N. Zavilopulo, Dokl. Akad. Nauk SSR, 214, 1288 (1974)

R. J. Zollweg, J. Chem. Phys., 50, 4251 (1969)